
SPECTROSCOPIC PROBES OF CHARGE SEPARATION,
ENERGY TRANSFER, AND THEIR DEPENDENCIES ON
LOCAL STRUCTURE IN ASSEMBLED ORGANIC
MATERIALS

by
Timothy J. Magnanelli

A dissertation submitted to Johns Hopkins University in conformity with the
requirements for the degree of Doctor of Philosophy

Baltimore, Maryland
10/2017

Abstract

Ultrafast, spectroscopic techniques were utilized to interrogate the properties and dynamics of excitonic and charge-separated states in aggregates and assemblies of conjugated polymeric and oligomeric materials relevant to organic electronics. Dependencies between photophysical dynamics and local morphology, intermolecular interactions, and chemical composition were explored. Novel, advanced experimental set-ups were developed and optimized for transient absorption (TA), femtosecond stimulated Raman (FSRS), and broadband transient polarization (BPA) spectroscopies. FSRS measurements yielded direct structural evidence that coupled charge transfer transients localize on morphologically well-ordered sites and clarified photophysical dynamics in poly-thiophene nanoaggregates. Transient absorption and broadband polarization measurements were used to characterize exciton dynamics in nonplanar thiophene-methanoannulene polymers and indicate limited intermolecular interaction with polymer aggregation. Evidence of prolonged charge separation and long-range energy transfer was identified in assemblies of peptidic charge transfer dyads and conjugated polyelectrolyte complexes, respectively. A unique experimental set-up for conducting ultrafast measurements of broadband electronic polarization

anisotropy (BPA) was developed and used to characterize the directionality and relaxation dynamics between excited states of 9,10-bis(phenylethynyl)anthracene and applied as a spectroscopic tool for examining other conjugated materials.

Acknowledgements

Firstly, I'd like to acknowledge the efforts of my research advisor, Art Bragg, for leading me throughout my graduate academic journey. His wisdom was invaluable in determining how to approach various challenges and answer difficult questions about these projects. He aided me in staying on track and applying my skills to the best of my abilities. His humility, not to be understated, made him an excellent leader and one that I'm glad to have been able to research under.

My labmates deserve a share of the credit as well. The original group included Jiawang, Wenjian, Molly, and Josh. The former two were ones I worked with on various polymer/conjugated material projects. We developed varying techniques for handling FSRS and other data and were able to collaborate on a few projects. Molly constantly provided optimism, unique perspective, helpful comments in response to findings and presentations, and a pension for grammar and proofreading that were invaluable in the first couple years.

Josh and I were probably opposite sides of the same coin. We looked at situations and problems a bit differently: he was the eager and efficient accomplisher, and I was the giddy and optimized perfectionist. Together we were able to tackle challenges including complex equipment set-up, machine shop fabrications, schematic and programmatic approaches to new and difficult experiments, and development of methods for interpreting data. I feel he probably contributed the most to a variety of results within the group, but I'd put myself at a close second.

Paul, Ken, Jamie, Chana, Brandon, and others came later, and they're all to be thanked for their contributions as well. Ken was a segue between us and future students: he began the exploration of new projects, always offered to help, and filled in a lot of the cracks where the group needed it. Jamie brought expertise with him that enabled our research to continue going strong and made an immediate impact within the group. He assumed unfinished projects with difficult questions left to answer and tackled them with enthusiasm. The others are the group's future, and will hopefully see some of my projects to the end beyond what's written herein.

I wouldn't be here without the funding provided to our group and me specifically! Start-up funds from Hopkins, DoE funding related to the OFET project, and other NSF and E₂SHI funding that Art received enabled us to obtain the materials and equipment to conduct our experiments. The Marks Award, Langmuir-Cresap Fellowship, and JHU teaching assistant stipends helped to support me over various semesters as well. Additionally, the NIH donations program proved invaluable in providing recycled equipment, including my desktop at work.

Several collaborators and staff members helped me to obtain complementary results presented herein. Various members of Professor Tovar's research group, namely Allix Sanders and Herdoline Ardon (Digs) prepared peptide charge/energy transfer systems that served as the basis for an interesting collaboration. Olivia Alley and others from Professor Katz's group prepared OFET devices for that project. Professor Alex Ayzner worked collaboratively on the CPEC project, while Professor Jim West made corona charging and other aspects of the OFET project possible. Julie Bitter ran DLS measurements with me to initially characterize my nanoaggregates. Later on Dr. Michael McCaffery and the JHU IIC staff instructed me on and helped me to run TEM scans (regular and cryogenic) in order to more accurately depict their sizes, shapes, and structural features. Countless other professors and staff members helped with everything from instruction in classes, strategies on handling spectroscopic challenges, NMR/FTIR spectra collection, and general advice/assistance with computer or mechanical projects.

On a more personal level, a number of people at Hopkins helped out in other aspects of my life. Josh, Ken, and Jamie were good friends outside of work, regularly playing games or sharing in good times and memories with me. Our Buckyballs soccer and other intramural teams won a few championships, and we gave it our all every season! Friends including but not limited to Ryan, Rob, Dan, Abhinav, Joe, Jason, Joel, Kyle, and countless other friends were also there in my personal life to share fun times and dilute troublesome ones with, which I could probably never thank them properly for. My faith also deserves credit for providing me the fortitude and a compass needed to guide me to this point in my life. My parents were my heroes growing up and raised me well! My siblings provided me with the strength and resolve to make it here and "graditate", brothers (and girl bros) in arms. I lived at home until I was 29 and harbor no regret in that regard because the right place for me was always just a drive away (UMBC to JHU) with home always right there where my heart was. My wife and her family graciously accepted me as one of their own over the past several years and have always been incredibly supportive of me as well.

Speaking of which, and saving the best for last, I want to acknowledge the love and support of my amazing wife Amanda. With our new home, our family we'll start together someday, and having each other at our sides, I know that we can take on anything and look forward to accomplishing so much in life. In closing, I once said in true cheesy fashion to her one Valentine's Day, "Nanoparticles are the smallest part of my life, your love is the biggest.", and I don't think I could phrase how I feel more efficiently than that.

To all of you: *Thanks and Godspeed!*

Contents

Abstract	ii
Acknowledgements	iv
List of Figures	ix
List of Tables	xi
List of Abbreviations	xii
1 Introduction	1
1.1 Applications and Relevant Photophysics	1
1.1.1 Light-Induced Charge and Energy Transfer in Condensed Organic Materials	3
1.1.2 Morphology and Aggregation	8
1.2 Principles of Ultrafast Spectroscopic Techniques	12
1.2.1 Electronic Excitation, Transient Absorption	13
1.2.2 Vibrational Characterization: Raman Spectroscopy and Femtosecond Stimulated Raman Spectroscopy (FSRS)	16
1.2.3 Electronic Polarization Anisotropy	22
1.3 Topical Overview	26
1.4 References	29
2 Experimental Methods	32
2.1 Nanoaggregate Synthesis	33
2.1.1 Nanoparticles Formed through Injection Reprecipitation	33
2.1.2 pH-Mediated Peptide Assembly	36
2.1.3 Nanoparticle Size Characterization: DLS and TEM	38
2.1.4 Sample Steady State Characterizations	40
2.2 Ultrafast Spectroscopic Techniques	41
2.3 Laser System Overview	42
2.4 Advanced Spectral Collection through Four and Eight Phase Data Acquisition	46
2.4.1 Fluorescence-Corrected TA (FCTA) and FSRS by Four-Phase Acquisition	47
2.4.2 Eight Phase Measurements: FSRS, PRP, and BPA	51

2.5	Data Processing and Analysis Techniques	54
2.5.1	Spectral Processing and Fitting Algorithms	56
2.5.2	Error Propagation and Uncertainty Predictions	60
2.6	Acknowledgments	61
2.8	References	61
3	Time-Resolved Raman Spectroscopy of Polaron Pair Formation in Poly(3-hexylthiophene) Aggregates	62
3.1	Abstract	62
3.2	Introduction	63
3.3	Experimental Methods	68
3.4	Results and Discussion	69
3.4.1	Steady State, GSR, and TA Considerations	69
3.4.2	Time Dependent FSRS and Kinetic Markers	73
3.4.3	Extraction of PTR Raman Spectra of RR-P3HT PP and Related Transients	77
3.5	Conclusions	84
3.6	Acknowledgments	84
3.7	References	85
4	Exciton Dynamics in Thiophene-Methanoannulene Polymers and their Aggregates	89
4.1	Abstract	89
4.2	Introduction	90
4.3	Experimental Methods	94
4.4	Results and Discussion	95
4.4.1	UV-Vis and Characterization	95
4.4.2	Transient Absorption: Impacts of Substituents and Comparisons to Oligomer and PTMTT	96
4.4.3	Photodynamic Effects of Increasing Pump Frequency	100
4.4.4	Photophysical Response to Aggregation	104
4.4.5	Polarization Anisotropy: Substituent Effects and Insights from Aggregation and the Oligomer	107
4.5	Conclusions	112
4.6	Acknowledgments	113
4.7	References	113
5	Photoinduced Electron Transfer within Supramolecular Donor–Acceptor Peptide Nanoassemblies under Aqueous Conditions	114
5.1	Abstract	114
5.2	Introduction	115
5.3	Experimental Methods	120
5.4	Results and Discussion	122
5.4.1	Transient Absorption of Dyads and Spectral Component Isolation and Characterization	122

5.4.2	Comparisons to Other Dyads and Dyad/Control Mixtures to Identify Energy Transfer	127
5.4.3	BPA and Comments on Prevalence of Charge Migration	129
5.5	Conclusions	132
5.6	Acknowledgments	133
5.7	References	133
6	Photoinduced Energy Transfer within Aqueous Co-assemblies of Conjugated Poly-Electrolytes	135
6.1	Abstract	135
6.2	Introduction	136
6.3	Experimental	138
6.4	Results and Discussion	140
6.5	Conclusions	150
6.6	Acknowledgments	151
6.7	References	151
7	Electronic Relaxation Dynamics of 9,10-bis(phenylethynyl)anthracene Studied with Ultrafast Broadband Polarization Anisotropy	153
7.1	Abstract	153
7.2	Introduction	154
7.3	Experimental Methods	158
7.4	Results and Discussion	159
7.4.1	BPA on Solution Phase BPEA	160
7.4.2	BPEA Nanoaggregates and Evidence of Intermolecular Energy Migration	166
7.5	Conclusions	167
7.6	References	168
8	Appendices	169
8.1	Appendix II: Experimental	169
8.1.1	Alternative Aggregate Preparation Techniques	169
8.1.2	Pump Re-pump Probe Spectroscopy	172
8.2	Appendix IV: PTMT	174
8.3	Appendix V: Dyad	177
8.4	Appendix VI: CPEC	179
8.5	Curriculum Vitae	179

List of Figures

1.1	Examples of Condensed Organic Materials	4
1.2	Energy Transfer Mechanisms	6
1.3	Visualizations of Charge Transfer	7
1.4	H- and J-Aggregate Comparisons (Energy Levels and Spectra)	11
1.5	Jablonski Diagram Illustrated Processes Relevant to TA	14
1.6	RR-P3HT TA Spectrum with Overlapping TA and GSB Absorptions	16
1.7	Classification of Vibrational Measurements	18
1.8	Illustrations and QM Representation of FSRs	21
1.9	Incident Anisotropy and Resulting Relaxation	24
2.1	Visualization of Reprecipitation	34
2.2	Example TEM Images	40
2.3	Fluorescence Corrected Transient Absorption Experimental Set-up . .	49
2.4	Femtosecond Stimulated Raman Experimental Set-up	50
2.5	Broadband Polarization Anisotropy Experimental Set-up	53
3.1	Steady State RR-P3HT NP Characterizations	71
3.2	RR-P3HT NP Transient Absorption Spectra	72
3.3	RR-P3HT NP PIR Contour Plot	74
3.4	RR-P3HT NP PIR Kinetic Markers vs. TA Comparison	76
3.5	RR-P3HT NP Intensity Dependent PIR Spectra	78
3.6	C=C and C-C Shifts and SVD Component Plots of RR-P3HT NP PIR	79
3.7	Extracted PTR Spectra of RR-P3HT Polaron and RRa-P3HT PP NPs	82
4.1	Thiophene-Methanoannulene Polymer and Oligomer Structures . . .	92
4.2	DFT Oligomer Estimate 3D Structures	93
4.3	Steady State Absorption Spectra of PTMTs	96
4.4	480 nm Excitation Transient Absorption of PTMTs	98
4.5	400 nm Excitation Transient Absorption of PTMTs	101
4.6	PTMT Stimulated Emission Peak λ Traces	103
4.7	480 nm and 400 nm Transient Absorption of PTMT NPs	106
4.8	Polarization Anisotropy Spectra of TTMTT	109
4.9	S ₁ Polarization Anisotropy Decay Traces	110
5.1	DA- <i>n</i> /C- <i>n</i> Synthesis, Structures, and Energy Levels	117
5.2	Dyad Stacking, Aggregates, and Photoluminescence	119

5.3	Transient absorption spectra of DA-2 dyads.	123
5.4	Isolated Components from SVD analysis of DA-2 TA Spectra	124
5.5	Fluence Dependence of DA-2 and C-2 Excited at 400 nm	128
5.6	DA-2, C-2, and 10:90 Mixture Decay Trace Comparison	130
5.7	Polarization Anisotropy of DA-2	131
6.1	PFPI and PTAK Steady State Properties	138
6.2	600 nm Transient Absorption of CPECs and Integrated Traces	142
6.3	360 nm Transient Absorption of PTAK and PTAK-dominant CPECs	144
6.4	360 nm Transient Absorption of PFPI and CPEC 80:20 and Integrated Traces	145
6.5	PFPI Subtraction and Energy Transfer Isolation from TA	148
7.1	BPEA Molecule, Transition Dipoles and UV-Vis Spectra	157
7.2	Molecular Orbitals for Electronic Excitations of BPEA Ground State	158
7.3	Molecular Orbitals for Electronic Excitations of BPEA Ground State	160
7.4	BPEA Parallel and Perpendicular TA and BPA Spectra	162
7.5	Kinetic Traces of BPA Measurements on BPEA	164
7.6	BPEA NC Transient Absorption and BPA Spectra	167
8.1	Wavelength/Frequency Shifts of PTMT Absorbances	174
8.2	Regression Model Parameters for PTMT GSB and S_1 Decays	175
8.3	BPA Contour Plots for PTMT Samples	176
8.4	480 nm Excitation and Control, Mixture, and Dyad TA Spectra	177
8.5	DA-6 and DA-3 TA Spectra	178
8.6	DA-2, 3, and 6 Integrated Decay Traces	178
8.7	PTAK Fluence Dependence NIR Decay Traces	179

List of Tables

2.1	Chopper Phase Assignment Table	54
4.1	PTMT Stimulated Emission Peak Initial λ and Shift	104
5.1	DA-2 Component Kinetic Fit Parameters	126
5.2	DA-2 Anisotropy Decay Parameters	131
6.1	CPEC Subtraction Decay Trace Fitting Parameters	149
7.1	BPEA Anisotropy Range Fit Parameters	164

List of Abbreviations

ArCl	Chlorobenzene
ATR	Average then ratio
BBO	Barium borate
BPA	Broadband polarization anisotropy
BPEA	9,10-bis-phenylethylnyl-anthracene
C-n	Control of dyad w/ separation length 'n'
CaF ₂	Calcium fluoride
CHCl ₃	Chloroform
CPEC	Conjugated poly-electrolyte complexes
DA-n	Donor-acceptor dyad w/ separation length 'n'
DCM	Dichloromethane
DF	Difference function (component of SVD)
DFT	Density functional theory (calculations)
DMSO	Dimethyl sulfoxide
EtOH	Ethanol
FSRS	Femtosecond stimulated Raman spectroscopy
GSR	Ground state Raman
HOMO	Highest occupied molecular orbital
IIC	Integrated imaging center
I/O	Digital input/output
ISC	Inter-system crossing
JHU	Johns Hopkins University
LUMO	Lowest unoccupied molecular orbital
MA	Magic angle
MeOH	Methanol
ND	Neutral density (filter)
NC, NP	Nanocrystal, nanoparticle
NIR	Near infrared
OD	Optical density i.e. absorbance
OPA	Optical parametric amplifier
OPV	Organic photovoltaic
P3HT	Poly-3-hexylthiophene
PCBM	Phenyl C ₆₀ butyric acid methyl ester
PFPI	Poly([fluorene]-alt-co-[phenylene]) iodide
PGS	Pseudo ground state (component of SVD)

PIR	Pump induced Raman
PRP	Pump re-pump probe
PTAK	Potassium poly-(alkylcarboxythiophene) derivative
PTR	Pure transient Raman
PTMT	Poly-thiophene-1,6-methano(10)annulene-thiophene
PTMTT	Poly-thiophene-methanoannulene-thiophene-thiophene
RRS	Resonant Raman scattering
RTA	Ratio then average
SC	Synchronous chop
SFG	Sum frequency generation
SHG	Second harmonic generation
SRS	Stimulated Raman scattering
SVD	Singular value decomposition
TA	Transient absorption
THF	Tetrahydrofuran
TI, TO	Tail-in, Tail-out (PTMT)
TTMTT	Bithiophene-methanoannulene-bithiophene
TPA	Transient polarization anisotropy
VI	Visual interface (LabVIEW program)
Vis	Visible
UV-Vis	Electronic absorption spectrum
UV	Ultraviolet
WG	Wire grid polarizer

Chapter 1

Introduction

1.1 Applications and Relevant Photophysics

Condensed phase organic materials incorporate a diverse array of hydrocarbon-based molecules in which delocalized π -bonding networks lead to unique and tunable photophysical properties and behavior. Conjugated oligomers and corresponding polymers have been utilized for more applications than can be fully described here and are prevalent in a host of applications relevant to the materials studied herein; they often serve as a semiconducting component of organic electronic devices, including photovoltaics (OPV)s, light emitting diodes (OLED)s, field-effect transistors (OFET)s, optical sensors, and other semiconductor devices. These materials offer advantages in processing and device fabrication, flexibility in material design, and scalability not always offered by similar inorganic counterparts. Unfortunately, these systems often struggle to compete in terms of cost effectiveness because of inefficiencies brought about by sample and molecular heterogeneity and labile structures which affect the nature of their photo-induced responses. The same degree of flexibility that holds so much promise also hinders our ability to understand how they

function and how to optimize their performance. By placing these materials into an aggregated environment (e.g. films), local structure and morphology critically determine the nature of electronic and charge-separated transients and the resulting heterogeneous dynamics of their physical and chemical actions. An important challenge that must be addressed is how the measurable properties of transient states can be directly related to local structure, namely its molecular conformations and morphology (microstructure of the material).

The focus of this work is to develop and apply spectroscopic techniques to study the photodynamics of specialized polymeric/oligomeric materials and how they are affected by intermolecular interactions and material morphology. Measurements specifically probed electronic and vibrational transitions of photoexcited materials on ultrafast (i.e. femto- to nanosecond) timescales, utilizing techniques including electronic transient absorption (TA), femtosecond stimulated Raman (FSRS), and broadband transient measurements electronic polarization anisotropy (BPA). These experiments facilitate the spectroscopic assignment of transient states, interrogate their charge and energy transfer mechanisms, and evaluate how these processes depend on the molecular morphologies of the systems described herein. Specialized polymeric and oligomeric materials, particularly nanoscopic aggregates or assemblies, were prepared and interrogated to determine how effectively they function for their designed photophysical task and to characterize their interactions to glean insights as to how the desired response, more so than applied devices made with the material, may be improved upon or made more efficient.

1.1.1 Light-Induced Charge and Energy Transfer in Condensed Organic Materials

Condensed organic materials used as semiconductors fall into several classes depending on what molecular units they are comprised of: namely molecular crystals, amorphous molecular films, and polymer films.¹ Example structures of each are included in Figure 1.1, with those of the latter two chosen from oligomeric/polymeric materials often incorporated in OPV devices. Molecular crystals consist of organic units, e.g. planar polyacenes, arranged about an ordered point lattice to form a repeatable lattice structure held together by van der Waal’s forces rather than electrostatic dipole interactions of their inorganic counterparts.¹ While these materials find applicability in certain fields, primarily OFETs, their weaker intermolecular interactions often limit their thickness and ability to maintain a fixed lattice structure when external current, photo-excitation, or other stimulus is applied, and thus our discussion focuses on the latter two classes.¹ Amorphous molecular and polymer films share many commonalities, in which conjugated structures have often been tailored to adjust energy levels, improve their solubility, or enhance particular aspects of the applicable chromophore, e.g. higher fluorescence quantum yield and charge separation yield for OLEDs and OPVs respectively. Naturally, the properties of these materials are also impacted by their environment and the microstructures they adopt because of their structural lability; oligomers are free to migrate within a layer of material, while polymers often form different types of packing phases (or order) to accommodate forces applied by surrounding condensed phase materials.

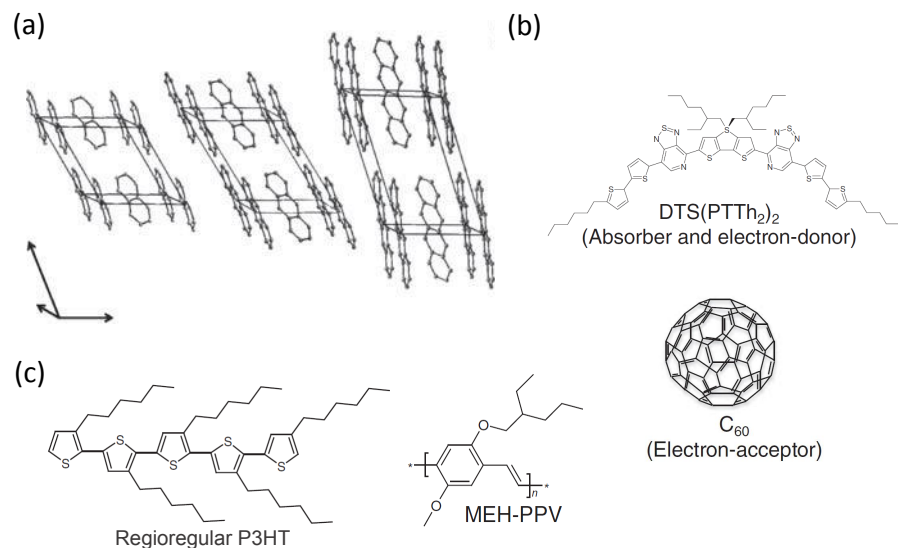


Figure 1.1: Examples of Condensed Organic Materials: prototypical (a) organic molecular crystals and components of (b) amorphous molecular films and (c) polymer films (c) used in OPVs¹

These oligomeric and polymeric materials are incorporated into systems to be inert with respect to their surroundings in the absence of a particular stimulus to promote their stability; these can include electrical, magnetic, or thermal stimuli but we will restrict our consideration to photoactive materials. Initial photoexcitation involves interaction of one of the material components with ultraviolet (UV), visible (Vis), or near-infrared (NIR) photons in order to excite an electron from the highest occupied molecular orbital (HOMO) to the lowest unoccupied molecular orbital (LUMO) or higher lying orbital in order to deposit energy. This process is akin to excitation about the bandgap of an inorganic semiconductor except that the organic excitation occurs as a promotion of an electron between localized molecular orbitals whereas excitation of the inorganic equivalent is a delocalized event from the conduction to valence bands of the inorganic equivalent. Of these, the latter excitation

occurs along a much more continuous electronic surface, and so the photoresponse, while still intrinsically complex, predominantly varies in the presence of defects and behaves uniformly elsewhere. Thus, inorganic semiconductors tend to exhibit very little charge carrier scattering, and hence significantly higher mobility than organic semiconductors.² As organic semiconductors rely upon discrete molecular interactions, which can lead to reactivity and degradation, the nature of such interactions becomes increasingly dependent on the local structure and molecular units surrounding the excitation site.

Part of the versatility in these materials lies in their ability to shuttle energy stored as an electronic excitation or isolated charges from photoactivated sites to regions where the energy can be utilized for useful work. This can occur through either energy or charge transfer depending on the materials used and presence of applicable interfaces. Following photo-excitation, energy transfer can occur radiatively through emission and re-absorption of a photon of light by a nearby chromophore whose absorption spectrum overlaps the emission spectrum of the initially excited material (e.g. an inner filter effect). However, it is often the case that the energy transfer occurs non-radiatively through the quantum-mechanical coupling between a donor and acceptor molecule and can occur by one of two prominent mechanisms shown in Figure 1.2, namely Förster (a) or Dexter (b) energy transfer.¹ Förster energy transfer involves an interaction between resonant energy donor and acceptor states that couple through dipole-dipole interactions and transfer energy spatially. Dexter energy transfer is more sensitive to the distance separating the donor and acceptor as it occurs through exchange coupling, a direct swapping of electrons through related

bonds rather than a transfer of energy through space.¹ Thus the former is most often the case in intermolecular energy transfer, while both play roles in intramolecular energy transfer along a polymeric backbone. Multiple precisely, but flexibly coupled processes occur among photosynthetic³ and biological light absorption systems (e.g. purple bacteria)⁴ in nature, and are critical for transporting energy to an interface to separate charge in an OPV device.^{5,6}

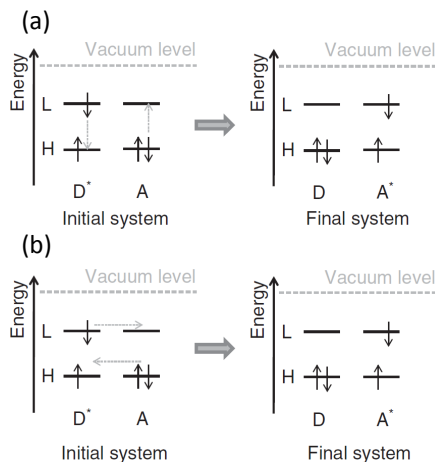


Figure 1.2: Energy Transfer Mechanisms: Depiction of Förster (a) and Dexter (b) energy transfer mechanisms¹

Charges can also be donated from one organic material to another depending on their relative electronegativities and the ability for the photoexcitation to reach sites at which interactions between electron-donating and electron-accepting moieties can occur. Photoinduced charge transfer occurs when an electron excited to the LUMO (or higher lying) energy state of an electron donor is transferred to a lower energy unoccupied orbital on an acceptor molecule without forming a new chemical bond ((a) of Figure 1.3).^{5,6} Through electrostatic interactions, the donor and acceptor

can form a complex or remain in close proximity to one another after electron donation has produced a hole-electron pair (h^+e^-), as shown in (b, 1) of Figure 1.3. While these charges will often recombine (3), they can persist and eventually separate from one another (2) by migrating through electron poor and rich layers of material to reach electrodes and be stored (e.g. OPV devices) or used for useful work (e.g. photocatalysis). The positions of the HOMO and LUMO are also critical for either energy or charge transfer to be energetically favorable and occur: specifically, energy transfer requires that the HOMO-LUMO energy gap of the donor be greater than that of the acceptor, while charge transfer requires that the LUMO of the acceptor be lower in energy than the LUMO of the donor.

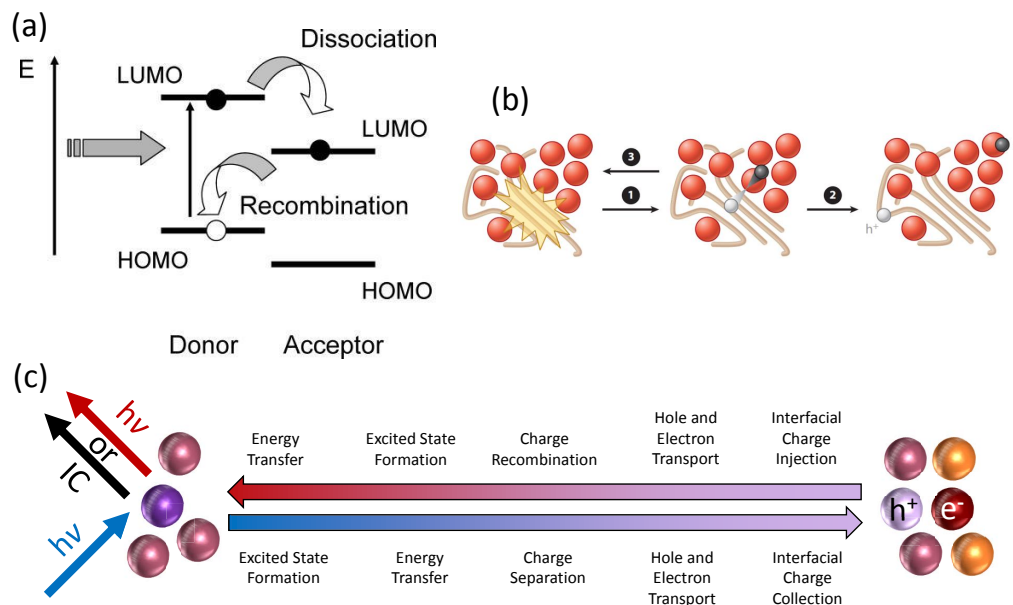


Figure 1.3: Visualizations of Charge Transfer: Depictions of (a) HOMO-LUMO interactions of donor and acceptor⁵, (b) depiction of charge (1) pair formation, (2) separation, and (3) recombination⁶, and (c) processes that occur between photoexcitation, hole pair formation, and emission/internal conversion⁵

This disparity between the energetic requirements of these processes allows

for materials to be chosen with the intent of being selective for one process over the other. This can be advantageous in discouraging charge separation within a given domain after excitation but prior to migration to the necessary interface, or critical in allowing local electric fields to be generated without localizing electronic transients on the charge accepting moiety (or unit) as considered in Chapter 5.⁷ Finally, part (c) of Figure 1.3 lists, in order, a number of processes that excited transient and charge separated states often undergo prior to separation (bottom left to right) or recombination and eventual emission/internal conversion (top right to left). As mentioned previously, these processes depend not only on the nature of the organic materials involved, but also on their morphology and the intermolecular interactions that occur in a condensed phase environment.

1.1.2 Morphology and Aggregation

Local molecular ordering is instrumental in determining how readily a material system will undergo a desired photophysical or photochemical process. More ordered morphologies are characterized by improved molecular packing and often serve as more planar sites for excitations to lower lying regions of excited state potential energy surfaces.⁸ Ordered regions within poly-3-hexylthiophene (P3HT) and fullerene (PCBM) heterojunction cells have been shown using microscopy and photocurrent imaging to be more electrically conductive than adjacent disordered regions⁹. However, the double-edged sword of ordering is that energy or charge transfer can be hindered by stabilizing the transients locally, preventing them from migrating beyond

the ordered domains that now behave as trap sites. This raises important questions about how we can impact local ordering and determine under which conditions we can selectively excite and devise overall strategies to improve yields or mobilities of electronic and charge separated excited states of interest.

Condensed organic materials are often very heterogeneously ordered, and a rather simple way to influence morphology is to anneal or thermally relax a sample. Annealing serves as an excellent means to homogenize local microstructures into more ordered configurations, which often shifts resulting spectroscopic signatures¹⁰ and can improve charge transfer yields¹¹. Selection of solvent in processing films is also critical, as precipitation from different solvents affects surface roughnesses and deposition morphologies.¹² Even mixtures of regio-random (RRa-) and regioregular (RR-) P3HT, which tend towards more ordered and disordered microstructures, respectively, can be mixed with PCBM in a ternary system to improve charge transfer yields over the use of more ordered RR-P3HT alone with PCBM.¹³

Different types of intermolecular interactions can occur upon aggregation of conjugated oligomeric (if long enough) and polymeric materials, with the two most important for consideration in this work being the formation of H- and J- type aggregates. H-aggregates are characterized by conjugated units stacked with their dipoles offset from one another in a direction orthogonal to that of the π -conjugated backbone, leading to hypsochromic shifts in absorptions and a decrease in the 0-0 vibrational mode. Counter to this, J-aggregates are formed by stacking conjugated units that have been offset in the direction of backbone propagation, leading to a direct alignment of dipoles, and resulting in bathochromic peak shifts and significantly higher

population of lower lying vibrational modes.^{14,15} Figure 1.4a shows H- and J-aggregate types of stacking as indicated by the energy level diagrams, slip stacking structures, and steady state absorbances/photoluminescence spectra of P3HT in (1)-(3), respectively.¹ The energy level diagrams indicate how dipole alignment leads to shifting of the absorbance bands, while the absorption and photoluminescence examples illustrate how different the distribution of Franck-Condon overlaps are shifted towards higher and lower vibrational levels for H- and J-aggregates, respectively. Figure 1.4b shows the temperature dependence of the self-stacking seen in RR-P3HT dissolved in methylated tetrahydrofuran and how the nature of ordering can be impacted by external factors¹.

Aggregating conjugated materials can lead to very different spectral features and photophysical responses.^{14,16,17} The morphologies of these condensed phase systems depends in large part on how the samples are prepared, whether or not they are annealed, and what specific materials are added to achieve the desired functionality.¹⁸ Excitations are also not constrained to one domain, as migration from one region to another, often towards those that are more ordered and lower in energy, can stabilize a given transient while serving as a trap or localization to engage in a photophysical process of interest.^{17,19,20} One focus of my research is to interrogate nanoaggregates fabricated from conjugated organic materials that emulate different levels of ordering within films. In the case of thiophene based oligomers and polymers, several different techniques exist for manufacturing nanoscopic aggregates: H-type reprecipitated nanoparticles formed via kinetic suspensions²¹ and mixed-solvent stabilized aggregates²², as well as J-type nanofibers²³ can all be synthesized for these purposes as

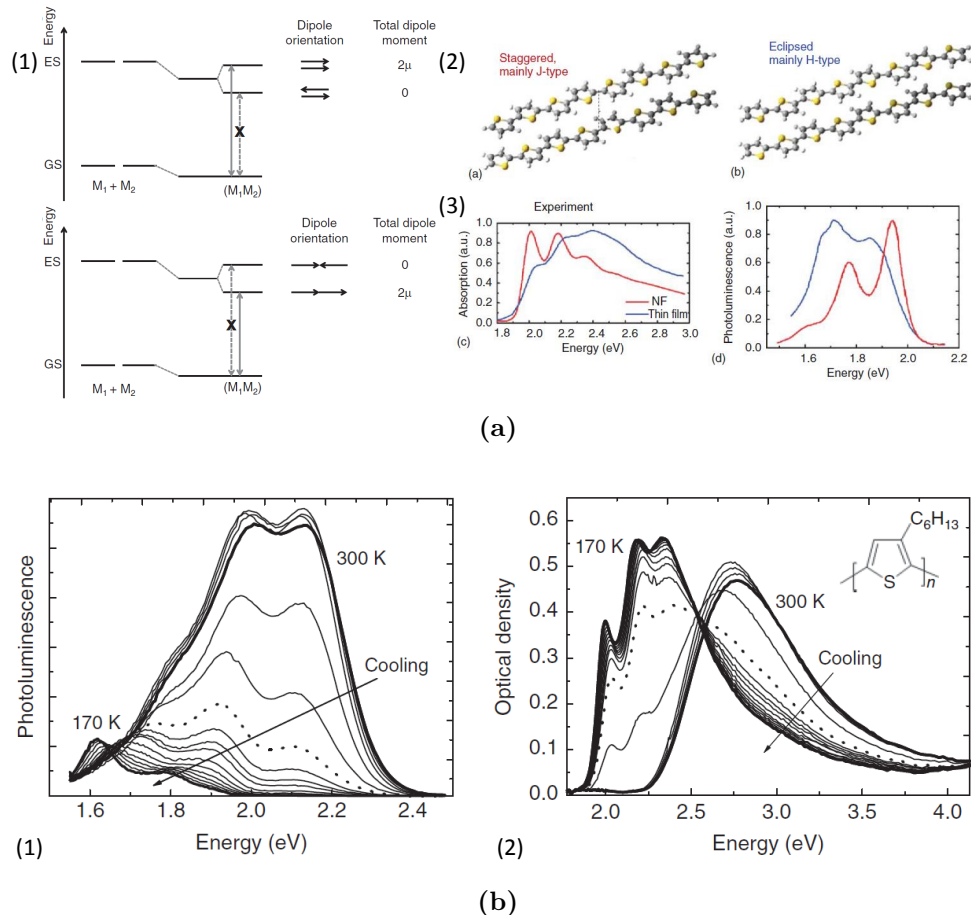


Figure 1.4: H- and J-Aggregate Comparisons (Energy Levels and Spectra): (a) energy level diagrams (1), molecular structures of stacking (2), and absorption and photoluminescence (3) of J- (red) vs. H-aggregates (blue)¹, and (b) temperature dependent photoluminescence (1) and absorption (2) of RR-P3HT in solution¹ (b)

described in Section 2.1. The primary intent is to characterize processes that occur within condensed phase organic materials and connect their dynamics with intra- and intermolecular order. In order to accomplish this several spectroscopic techniques are utilized as the primary tools for examining how these systems behave in response to changes in material composition, excitation conditions, and differences in morphology and external environmental factors.

1.2 Principles of Ultrafast Spectroscopic Techniques

The interaction of light with materials depends on their electronic characteristics, such that spectroscopy can serve as a valuable and informative probe of material properties. Combining this with the ability of light to induce a photophysical or photochemical response upon exposure permits the use of time-resolved spectroscopic measurements to characterize material photoresponses. Using light as both a driving force of photoresponses in these molecular systems and a probe for how those responses manifest as spectroscopic signatures of electronic and vibrational excitation along the molecule’s potential energy landscape, transfer of energy/charge, or bonding to another molecule. These provide meaningful insights into how the properties of the system can be altered to achieve a particular photoresponse.

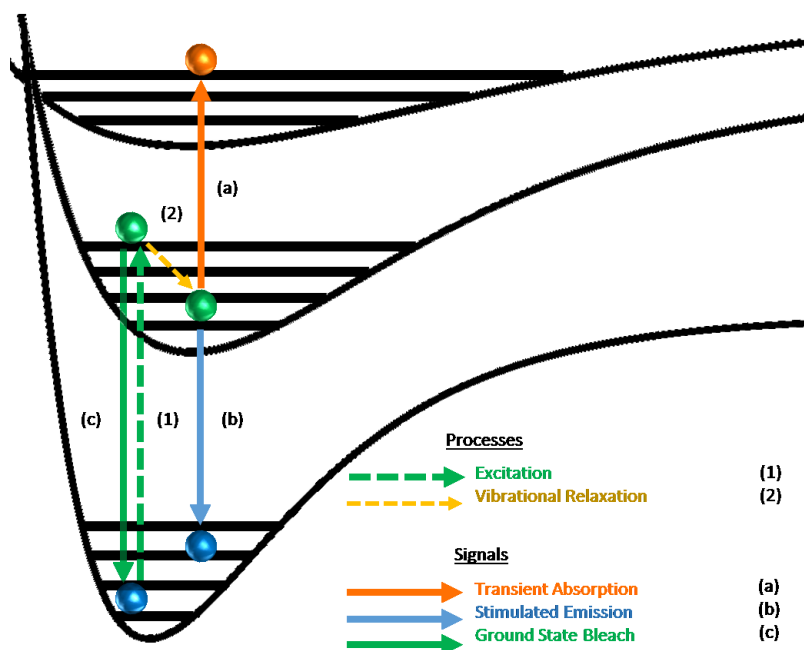
The photoinduced interactions considered by this work can be broken into three primary categories. Absorption of photons yields temporally dependent alterations to a molecule’s electronic absorption spectrum, and these induced differences are known as transient absorption (TA). This technique can be combined with an additional laser pulse to inelastically scatter light off the sample to probe vibrational modes of transients using femtosecond stimulated Raman spectroscopy (FSRS). Lastly, the alignment of electronic dipoles associated with transitions between electronic states relative to the polarization used for photoexcitation monitor the orientation of a molecule, localization of a transient state, or extent of energy/charge transfer using transient electronic polarization anisotropy (TPA); in the novel application of

this technique considered in subsequent chapters (e.g. Chapter 7), it is labeled as broadband polarization anisotropy (BPA). Each of these techniques assists in clarifying the photoresponses of the materials presented herein. Conceptual aspects of these methods are described below, with technical details reserved for Chapter 2.

1.2.1 Electronic Excitation, Transient Absorption

Transient absorption (TA) has long been utilized as a tool for interrogating organic condensed material systems useful for OPVs^{24,25}, biological systems²⁶, photochemical dynamics^{27,28}, and photoswitch applications²⁹. TA is a technique in which the evolution of electronic absorption of a material is monitored as a function of time after photoexcitation. The technique provides critical information about the electronic absorption profiles of populated transient states as well as signatures that result from the perturbation of the steady state absorption. Steady state absorption corresponds to comparison of a broadband white light continuum with and without the sample present to determine the absolute electronic absorption profile of that sample. TA, on the other hand, involves comparing the broadband probe with and without an electronic excitation pulse present to drive photophysical process that modify light transmission through the sample. Figure 1.5 shows a Jablonski diagram used to depict the signatures associated with the electronic excitation of a molecule. The primary spectral modifications analyzed as part of these measurements are transient absorption signals (a) which involve excitations to higher-lying electronic states (also labeled TA). A second signature (b), is derived from the loss of part of the steady

state absorption spectrum due to the *dep*opulation of molecular ground states following excitation, known as a bleaching of the ground state (GSB). Finally, signatures due to stimulated emission (SE) from the a singlet excited state back to the ground state are also apparent (c), with TA spectra reflecting some combination of these three types of signals. Additional features can occur due to higher order processes or at higher excitation fluences but are omitted from consideration here.



Jablonski diagram depicting processes occurring to make up a transient absorption signal namely (a) TA, (b) GSB, and (c) SE

Figure 1.5: Jablonski Diagram Illustrated Processes Relevant to TA: Depicts processes occurring that comprise a prototypical transient absorption signal, namely TA (a), GSB (b), and SE (c)

An important aspect of the evolution of a TA spectrum with time is how the central frequency and spectral width of these various transient features can change with time. These spectral alterations can reflect vibrational relaxation of a particular transient,³⁰ exciton migration/hopping¹⁹, or the transfer of population from one

state to another⁷. The measured photodynamics and spectral progressions can be monitored quantitatively to better understand how they rely on aspects of their excitation and surroundings including fluence^{25,31} or frequency³² of the excitation pulse and solvent environment²⁷. Additionally, the kinetics with which various electronic excited state features decay provide insight into molecular reaction mechanisms and relaxation pathways. In particular, the features present at a given time following excitation can be used to determine the identity of a particular species and clarify over what timescales it will form, decay, or transition to another state.

Often the simplest approach to quantitatively analyze TA spectra is to examine isolated spectral regions, where an integrated cut of the TA spectrum only samples the population of a single (or directly coupled) state(s). This permits accurate and straightforward estimation of system kinetics where feasible. Complications arise, however, when multiple bands overlap one another spectrally and temporally. An example of this is shown in Figure 1.6, which illustrates how multiple features, namely a TA and GSB band for a transient absorption spectrum of RR-P3HT nanoparticles³³ can coincide in the same spectral region, leading to difficulties in discerning the spectral and kinetic characteristics associated with each feature independently. While plotting these spectra as a function of frequency and modeling with Gaussian functions can be valuable, the spectral complexity and vibrational structures of these features often necessitate using a more intricate modeling method. Mathematical algorithms related to singular value decomposition (SVD) can be used to decouple spectra from one another.^{7,27,28} Examples include principal component analysis (PCA), a common method used to extract spectral components, and global analysis (GA),

which constrains SVD relative to a particular kinetic model. Unique SVD algorithms for parsing the species found within TA spectral progressions are incorporated into several analyses presented in this dissertation (Chapters 3 and 5). Other experimental, rather than technical, challenges arise in analyzing TA results obtained from an ultrafast set-up (e.g. multi-photon excitation and temporal chirp) but consideration of these is reserved for Chapter 2.

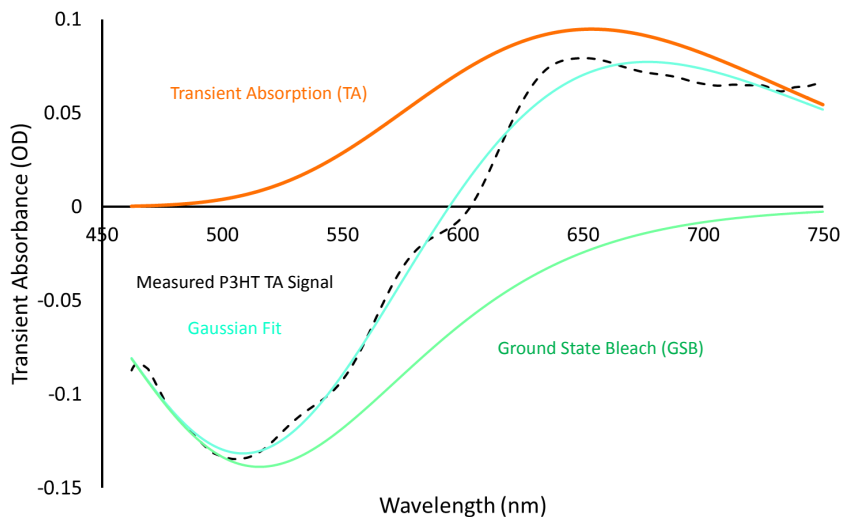


Figure 1.6: RR-P3HT TA Spectrum with Overlapping TA and GSB Absorptions: visible spectrum decoupled into a TA signature from a charge-pair transient state and a GSB signal due to depopulation of the ground state and overlaid with a Gaussian fit function

1.2.2 Vibrational Characterization: Raman Spectroscopy and Femtosecond Stimulated Raman Spectroscopy (FSRS)

Ultrafast vibrational spectroscopies provide excellent complementary results to electronic excitation spectra derived from TA measurements. Vibrational techniques can be broken down into two types, infrared (IR) and Raman scattering as

shown in Figure 1.7a. While these two techniques explore similar regimes of energy separation (vibrational energy gaps), they do so with sensitivity to different modes and through different experimental methodology. The primary difference between the two modes lies in the characteristic of each vibration that determines its susceptibility to inelastically scatter: vibrational modes are sensitive to IR if the corresponding molecular motion causes a net change in electrostatic dipole as a result, while modes are Raman active if the motion yields a net change in polarizability, loosely interpreted as the volume containing electron density. Examples of exclusively IR and Raman active modes of CO₂ are included as Figure 1.7b, but for larger molecules that are not centrosymmetric (lack an inversion center), the modes are not mutually exclusive.

The most important aspect of what makes Raman spectroscopy so useful for conjugated oligomers and polymers is that their Raman cross sections are greatly amplified by the large changes in polarizability associated with the electron delocalization seen for their electronic excited states.³⁴ Ultrafast Raman is also more useful as it uses visible excitation (and probe, FSRS) wavelengths compared to the mid- to near-infrared pulses for which IR transitions are named, making ultrafast IR experimental set-ups less compatible with TA measurements than comparable Raman set-ups. As indicated in Figure 1.7a, Raman scattering occurs when an incident photon of light inelastically scatters off of a molecule by depositing or absorbing a quantum or quanta of energy into or from a particular vibrational mode in what are known as Stokes and Anti-Stokes scattering, respectively. Thus, Raman scattering features are emitted at much narrower output wavelengths than TA features, due to the energetic specificity

of a particular vibrational transition, and occur at wavelengths relative to the incident wavelength of the Raman excitation source with added or reduced energy of a particular frequency (~ 100 's to 1000 's of cm^{-1}) unique to each vibrational mode.

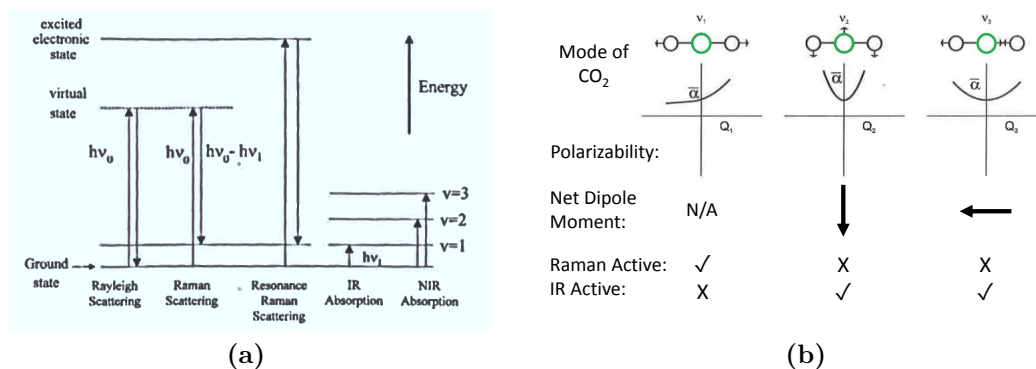


Figure 1.7: Classification of Vibrational Measurements: (a) energy level diagrams of IR and Raman transitions,³⁵ and (b) CO₂ vibrational modes illustrating IR and Raman susceptibilities³⁶

Raman scattering itself can be either stimulated or spontaneous. Spontaneous Raman consists of scattering upon exposure to a light source without any additional enhancement, resulting in weak, non-directional signals. While multiple methods are available for improving the sensitivity, FSRS incorporates a second pulse, a broadband probe, to complete a correlation interaction at the scattered wavelength and generate Raman gain (or depletion) to the wavelengths that correspond to Raman scattering. In fact, many related quantum mechanical signals are allowed within a FSRS measurement as displayed in part (1) of Figure 1.8a. The most important of these is the resonant Raman scattering RRS(I) subset of stimulated Raman scattering (SRS), in which simultaneous interaction of the Raman excitation and broadband probe in this order, establishes a coherence to produce gain at the vibrational frequencies of interest after a second interaction with the pump pulse. The other signals contribute to low

resolution background signatures which are removed from resulting Raman spectra or other isolatable features which are not considered here for brevity.³⁷ Part (2) of Figure 1.8a displays the temporal dependence of these pulse and how they impact propagation of the resulting excited state wavepacket.³⁷

In either spontaneous Raman or FSRS, the application of an initial actinic excitation pulse analogous to a TA measurement can be used to create an excited state wavepacket that allows for the vibrational modes of transient states to be explored as well. This becomes possible by selecting a Raman excitation wavelength that overlaps with the absorbance of a particular transient state. This specification of the technique dramatically amplifies Raman features associated with geometric changes adopted by the molecule were further excitation of that transient state to occur, taking advantage of what is known as resonance enhancement. Resonance Raman can be several orders of magnitude more intense than non-resonant Raman signatures, which is taken advantage of to extract structural information about specific transients as will be seen in Chapter 3.

In addition to using the Raman probe as a heterodyne gain medium for improving signal intensities, FSRS is also superior to spontaneous Raman for its ability to decouple spectral from temporal resolution that a spontaneous measurement would ordinarily be limited by. Similar to a minimum uncertainty between the position and velocity of a particle, the uncertainty principle also states that the maximum simultaneous precision of the spectral and temporal resolution of a transform limited Gaussian pulse is given by Equation 1.2.2. However in FSRS, the spectral and temporal resolution of the resulting SRS data are decoupled as shown by part (2)

of Figure 1.8a.³⁷ Initially, an excited state wavepacket is populated by an actinic pump pulse as would be done in a transient absorption measurement. Then, a coherence is formed between the Raman pump and broadband probe after a fixed delay relative to original excitation with the time resolution of the result only being limited by the temporal bandwidth of the probe (~ 100 fs). Since the coherence began at an indeterminate time (black dashed arrows) prior to completion (green wave), the temporal uncertainty is maintained without sacrificing spectral resolution which is determined by the linewidth of the Raman excitation pulse involved in this final step. Thus, this FSRS process permits accurate spectral and temporal interrogation of transient state vibrational modes.

$$\Delta t * \Delta \omega \geq \sqrt{2}h \quad (1.1)$$

Experimental set-ups have been well characterized elsewhere^{38,39} and details about the equipment used are reserved for Section 2.2. However, Figure 1.8b highlights a few other aspects of FSRS measurements that are worth noting. Part (1) shows the temporal arrangement of pulses used to conduct a FSRS measurement, colored to correspond to the more straightforward Jablonski diagram shown by part (2). These spectra highlight how delays between the actinic and probe pulse can be used to control the prevalence of particular transients while the Raman pump delay can be adjusted about the probe to establish an optimal coherence, both in terms of spectral shape and signal intensity. Finally, part (3) of Figure 1.8b shows example

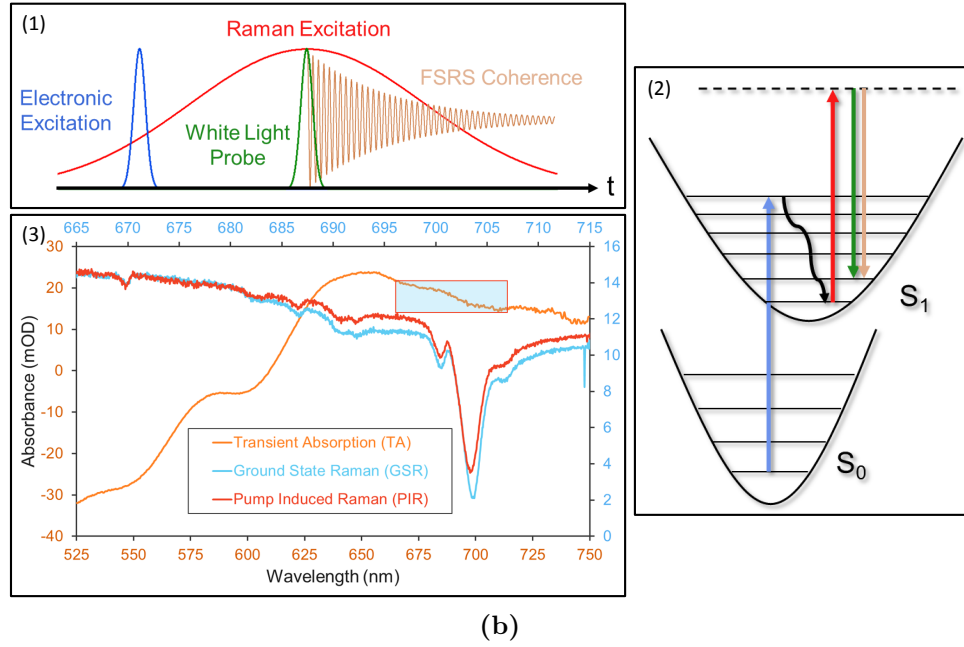
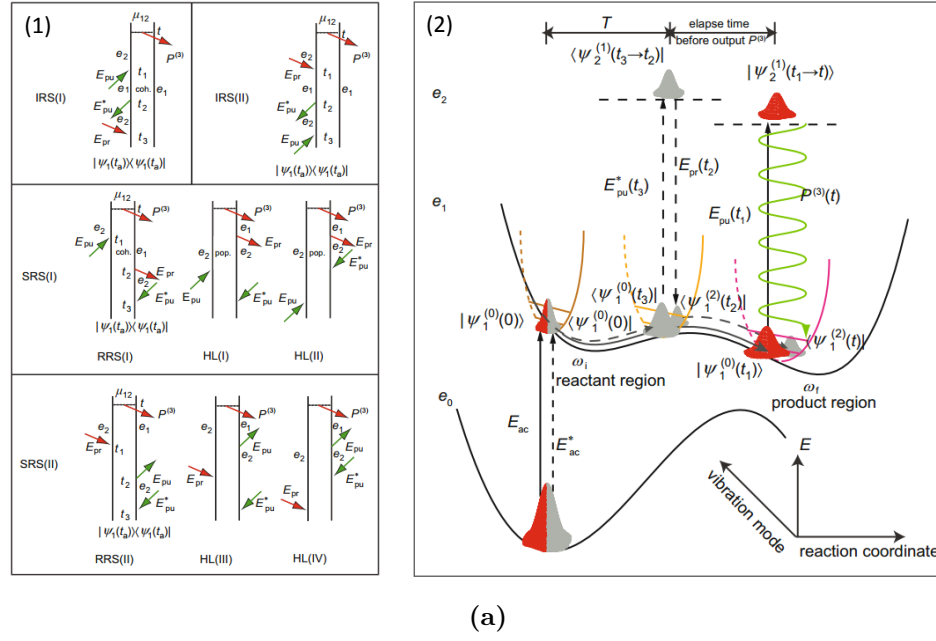


Figure 1.8: Illustrations and QM Representation of FSRS: (a) quantum mechanical descriptions of FSRS including its associated Feynman diagrams (1) and the wavepacket propagation of stimulated Raman scattering that illustrates the decoupling of temporal and spectral resolution (2),³⁷ and (b) representations of the temporal progression of FSRS pulses (1), Jablonski diagram that coincides with this temporal progression (2), and an example of analogous RR-P3HT TA and FSRS spectra (3)³⁷

measurements of P3HT NPs further detailed in Chapter 3, to exemplify the differences between transient absorption and Raman features. While pure ground state, and transient state Raman measurements often produce remarkably different progressions, rigorous comparison can quantify these discrepancies to gain insight into how the structure of the resonant transient differs from that of the original ground state molecule.

1.2.3 Electronic Polarization Anisotropy

In order for a particular conjugated material to absorb a photon of light and access a higher lying electronic state, the transition must be allowed by symmetry and amenable overlap between the orbitals and structural configuration of both states of the molecule. The likelihood for a transition to occur is determined by the combination of these factors and is often reflected quantitatively as a Franck-Condon factor or overlap between the two states. The Franck-Condon overlap represents how strongly coupled two states are to one another and how prominent the asymmetric inversion of the poles is within overlapping regions of electron density between the molecular orbitals of interest, most often occurring in ordinary excitations as a transition dipole. Relative to the geometric framework of the molecule, these transition dipoles are inherently directional and correlate to specific orientations of molecular orbitals of the chromophore or moiety involved in the absorption, emission, or transient feature. Thus, in order to excite the transition, it is necessary for the incident light to not only be of the correct wavelength to correspond with the bandgap of the electronic

excitation, but for the polarization of the incoming excitation pulse to be parallel to that of the transition dipole within the absorbing molecule as well. While this does not pose an issue in exciting randomly oriented molecules, it necessitates that inorganic and organic crystal structures be oriented correctly (rotationally) in order to maximize the possibility for excitation.

For randomly oriented samples, as is the case with conjugated polymeric and oligomeric materials, polarization anisotropy arises when molecules whose dipoles are aligned with the excitation source are predominantly excited relative to those that are not. Upon creating this directional transient polarization, the response that the transient population exhibits when probed along orthogonal cardinal polarization axes relative to the directional, polarized light source will not be equivalent (hence the term anisotropy). The distribution of excitations immediately following excitation reflects a \cos^2 dependence along the axis of the polarization as defined in Equation 1.2a and Figure 1.9a. This signal anisotropy may disappear by one of several mechanisms. Specifically, the entire molecule may rotate within a vapor or liquid medium prior to transient relaxation (e.g. gas phase or isolated molecules dissolved in solution) or via migration of the excitation through a condensed phase aggregate material on to dipoles offset by a fixed (aggregated stacks/assemblies) or random amount (amorphous aggregates) . This results in a directional memory of the original excitation that diminishes or is forgotten altogether in time, typically over the span of pico-microseconds depending on the molecule and relaxation process. Importantly, excited state relaxation or energy transfer can also occur, yielding diminished or well defined anisotropic distributions that do not align with the original excitation

source or initially prepared distribution. After one or more of these mechanisms have transpired, the polarizations of excited state transients will either relax or revert to an isotropic distribution as shown in Figure 1.9b.

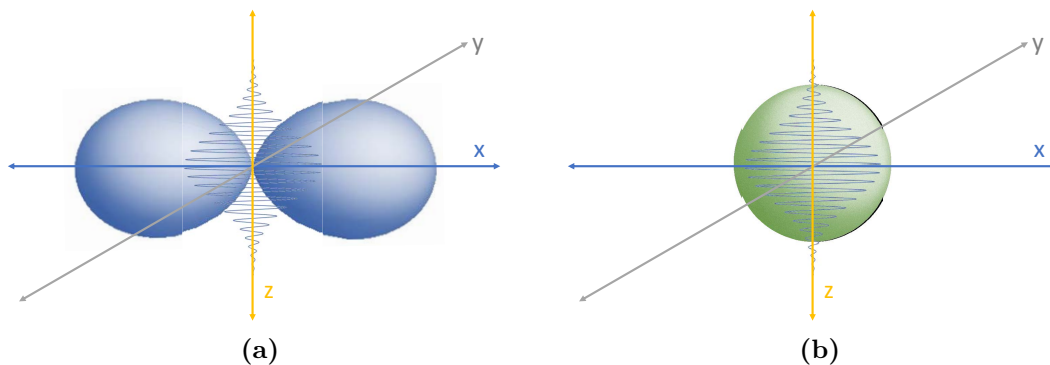


Figure 1.9: Incident Anisotropy and Resulting Relaxation: (a) imposed dipole by polarized excitation by a light source traveling along the z-axis, with the polarization of its electric field oriented along the x-axis, and (b) resulting isotropic dipole distribution of an ensemble of molecules after complete homogeneous rearrangement/randomization

Ordinarily, TA measurements are corrected for anisotropy to extract information due solely to population dynamics rather than directional heterogeneity of the sample. This occurs at the polarization angle (between polarizations of the pump and probe) where the probe can more preferentially sample under-represented perpendicular polarizations relative to parallel ones. For a three dimensional, randomly oriented sample, this occurs when the signal in orthogonal (perpendicular) directions to the incident excitation polarization is reflected twice as much as signal from the parallel polarization to account for there being two orthogonal dimensions in which polarization can occur. Namely, if a pulse is propagating along the z-axis with polarization aligned along the x-axis (Figure 1.9), measurements can be conducted by a (nearly) parallel incident probe pulse with polarization elements along the x- and y-axis, but the y-axis component must be doubled to represent both the y- and z-axis

signals. Additionally, the signals cannot be simply doubled as a result of the \cos^2 dependence of excitation and thus the polarization of the probe is set to an angle with proportional intensities such that $\cos^2(x) = 2\cos^2(y)$, which occurs at what's known as magic angle (MA), 54.7° . Setting the probe polarization to this orientation relative to the pump polarization ensures that modifications to signal due to anisotropy are canceled out, resulting in only the system's population dynamics being present in the resultant spectra.

$$r_0(\lambda) = \frac{3\cos^2\theta - 1}{5}, -0.2 < r_0(\lambda) < 0.4 \quad (1.2a)$$

$$I_{MA} = \frac{I_{\parallel} + 2I_{\perp}}{3} \quad (1.2b)$$

$$r(t, \lambda) = \frac{I_{\parallel} - I_{\perp}}{I_{\parallel} + 2I_{\perp}} \quad (1.2c)$$

$$r_{Total}(t, \lambda) = \frac{\sum_i^n (r_i * I_{MA,i})}{\sum_i^n (I_{MA,i})} \quad (1.2d)$$

However, given the information available in anisotropies for determining the kinetics, trajectory, or extent of molecular motion and excited state energy transfer, one simply needs to obtain multiple probe polarization signals from the same measurement to calculate quantities reflective of the transient state dipoles as a function of time. Equation 1.2c shows how a polarization anisotropy is calculated, namely by comparing the difference between parallel and perpendicular responses normalized for signal intensity (with the magic angle intensity in the denominator).⁴⁰ If a sample exhibits a completely isotropic transient signature ($I_{\parallel} = I_{\perp}$), this quantity will be zero, but any preference towards parallel or perpendicular alignment of the dipole of

a signature relative to the incident pump polarization will be reflected as a positive or negative value, respectively. Again, Equation 1.2a describes the initial polarization anisotropy imposed by an excitation pulse on a sample, depending on the angle of the resulting dipole and can vary strictly between -0.2 and 0.4 for a three-dimensionally isotropic ensemble of sample molecules.

Overlapping spectral features can also constructive or destructive contribute to this time dependent quantity which is why isolating these signatures as a function of wavelength as well can allow for the anisotropy associated with each feature to be modeled and decoupled using Equation 1.2d⁴⁰. With overlapping features, it is possible for anisotropy values to approach $\pm\infty$ if the signals are opposite in sign (i.e. TA and GSB).⁴⁰ Given this dependence, great care must be taken to ensure that the broadband probe is not passed through or off of optics that would rotate or alter the polarization prior to its selection to ensure that the polarization is not arbitrarily and erroneously shifted, a concern handled by the experimental set-up described in Section 2.4.2.⁴¹ Additionally, more complicated dependencies on polarization can occur for higher order processes, such as FSRS, but are omitted here for brevity.⁴²

1.3 Topical Overview

The six chapters that follow consider, first, the experimental methodologies associated with the materials and ultrafast spectroscopic measurements are presented in Chapter 2. Important facets of sample preparation, the specific spectroscopic equipment utilized, and the analysis of the resulting spectra are all considered here.

Chapter 3 considers the extraction of structural information for transient states of RR-P3HT nanoparticles, particularly coupled polaron pairs. FSRS is demonstrated to be a powerful and morphologically selective probe of the structures adopted by these charge transfer transients. An SVD based algorithm was developed for the extraction of a pure Raman spectrum representative of individual transients from a series of power-dependent measurements, and time-dependent markers (both shifting and intensity depletion) provide kinetic information directly comparable to that seen by accompanying TA studies. While this is the only explicit FSRS based content presented as part of this thesis, the technique is nevertheless shown to hold potential applicability to future research endeavors on related materials.

Chapter 4 considers a second system of conjugated polymers comprised of alternating bithiophene and methanoannulene groups (PTMTs), designed to disrupt the intermolecular π -orbital overlap between adjacent polymer strands without strongly diminishing overall intramolecular conjugation. The impact of hexyl substituents placed in differing positions along the backbone, modifying excitation frequency and aggregating the materials are analyzed to clarify the nature of discrepancies in their photophysics and dynamics. Transients seen within polymeric aggregates are shown to relax much more rapidly than their solution phase counterparts. However, the lack of other substantial changes to the ultrafast spectra indicates that unique electronic or charge separated excited states are not formed as a result of intermolecular interactions amongst aggregates. Broadband polarization data is also presented to compare the mobility and delocalization of these states within different types of polymer environment and as a function of excitation frequency.

Chapters 5 and 6 are similarly themed research topics that center around the interrogation of charge and energy transfer within peptide-based dyad and polyelectrolyte complex supramolecular assemblies, respectively. Chapter 5 illustrates evidence of immediate and induced charge separation between a quaterthiophene (4T) electron donor and naphthalene diimide (NDI) electron acceptor positioned a fixed distance away along a peptidic backbone. SVD decouples the spectral and kinetic profiles of the 4T singlet, which decays on a sub-picosecond timescale, from the charge transfer state ($4T^+-NDI^-$) which shows a much more prolonged lifetime when the dyads are assembled. Measurements conducted with mixtures of dyad and NDI-less control molecules highlight the ability for energy transfer between 4T units along aggregated stacks prior to charge separation. Polarization anisotropy on the assembled system indicates that charges are likely relatively immobile once separated. Polyelectrolyte co-assemblies of poly([fluorene]-alt-co-[phenylene]) iodide (PFPI) energy donor and potassium poly-(alkylcarboxythiophene) (PTAK) energy acceptor are the focus of Chapter 6 in which coordinated excited state energy transfer (EET) is proven by a similar means to occur from PFPI to PTAK. Modifications to aggregation patterns within the acceptor aggregates are also analyzed as well as what effects changing the relative loading of donor and acceptor within the assemblies has on their overall photophysics.

Finally, the technique of BPA is demonstrated through the characterization of the polarization dynamics of a test molecule, 9,10-bis-phenyl-ethynylanthracene (BPEA) in Chapter 7. The relative dipole vectors, relaxation kinetics, and photodynamics of excitations to the molecule's lowest lying and a higher lying excitation

are compared and illustrate how the technique can be effective at characterizing the orientation of and transfer between different electronic excited states. Comparisons are made between free rotation of isolated molecules in solution and polarization decay brought about by energy transfer in aggregated nanocrystals, establishing the technique as a viable descriptor of both processes.

References

1. Köhler, A. *Electronic Processes in Organic Semiconductors: An Introduction*. Wiley-VCH, first edition, (2015).
2. Coropceanu, V., Cornil, J., da Silva Filho, D. A., Olivier, Y., Silbey, R., and Brédas, J.-L. *Chem. Rev.* **107**(4), 926–952 (2007).
3. Berardi, S., Drouet, S., Francàs, L., Gimbert-Suriñach, C., Guttentag, M., Richmond, C., Stoll, T., and Llobet, A. *Chem. Soc. Rev.* **43**(22), 7501–7519 (2014).
4. Aratani, N., Kim, D., and Osuka, A. *Acc. Chem. Res.* **42**(12), 1922–1934 (2009).
5. Brédas, J.-L., Beljonne, D., Coropceanu, V., and Cornil, J. *Chem. Rev.* **104**(11), 4971–5004 (2004).
6. Vandewal, K. *Annu. Rev. Phys. Chem.* **67**(1), 113–133 (2016).
7. Sanders, A. M., Magnanelli, T. J., Bragg, A. E., and Tovar, J. D. *J. Am. Chem. Soc.* **138**(10), 3362–3370 (2016).
8. Noriega, R., Rivnay, J., Vandewal, K., Koch, F. P. V., Stingelin, N., Smith, P., Toney, M. F., and Salleo, A. *Nat Mater* **12**(11), 1038–1044 (2013).
9. Gao, Y., Martin, T. P., Thomas, A. K., and Grey, J. K. *J. Phys. Chem. Lett.* **1**(1), 178–182 (2010).
10. Tsoi, W. C., James, D. T., Kim, J. S., Nicholson, P. G., Murphy, C. E., Bradley, D. D. C., Nelson, J., and Kim, J.-S. *J. Am. Chem. Soc.* **133**(25), 9834–9843 (2011).
11. Ayzner, A. L., Wanger, D. D., Tassone, C. J., Tolbert, S. H., and Schwartz, B. J. *J. Phys. Chem. C* **112**(48), 18711–18716 (2008).
12. Huang, Y., Kramer, E. J., Heeger, A. J., and Bazan, G. C. *Chem. Rev.* **114**(14), 7006–7043 (2014).

13. Campoy-Quiles, M., Kanai, Y., El-Basaty, A., Sakai, H., and Murata, H. *Organic Electronics* **10**(6), 1120–1132 (2009).
14. Spano, F. C. *Acc. Chem. Res.* **43**(3), 429–439 (2010).
15. Spano, F. C. and Silva, C. *Annu. Rev. Phys. Chem.* **65**(1), 477–500 (2014).
16. Martin, T. P., Wise, A. J., Busby, E., Gao, J., Roehling, J. D., Ford, M. J., Larsen, D. S., Moulé, A. J., and Grey, J. K. *J. Phys. Chem. B* **117**(16), 4478–4487 (2013).
17. Tapping, P. C., Clifton, S. N., Schwarz, K. N., Kee, T. W., and Huang, D. M. *J. Phys. Chem. C* (2015).
18. Hu, Z., Tenery, D., Bonner, M. S., and Gesquiere, A. J. *Journal of Luminescence* **130**(5), 771–780 (2010).
19. Wells, N. P., Boudouris, B. W., Hillmyer, M. A., and Blank, D. A. *J. Phys. Chem. C* **111**(42), 15404–15414 (2007).
20. Yagita, Y. and Matsui, K. *Journal of Luminescence* **161**, 437–441 (2015).
21. Shimizu, H., Yamada, M., Wada, R., and Okabe, M. *Polym. J* **40**(1), 33–36 (online November 13, 2007).
22. Scharsich, C., Lohwasser, R. H., Sommer, M., Asawapirom, U., Scherf, U., Thelakkat, M., Neher, D., and Köhler, A. *J. Polym. Sci. Part B Polym. Phys.* **50**(6), 442–453 (2012).
23. Niles, E. T., Roehling, J. D., Yamagata, H., Wise, A. J., Spano, F. C., Moulé, A. J., and Grey, J. K. *J. Phys. Chem. Lett.* **3**(2), 259–263 (2012).
24. Ohkita, H. and Ito, S. *Polymer* **52**(20), 4397–4417 (2011).
25. Guo, J., Ohkita, H., Bente, H., and Ito, S. *J. Am. Chem. Soc.* **131**(46), 16869–16880 (2009).
26. Berera, R., van Grondelle, R., and Kennis, J. T. M. *Photosynth Res* **101**(2-3), 105–118 (2009).
27. Molloy, M. S., Snyder, J. A., DeFrancisco, J. R., and Bragg, A. E. *J. Phys. Chem. A* **120**(23), 3998–4007 (2016).
28. Snyder, J. A. and Bragg, A. E. *J. Phys. Chem. A* **119**(17), 3972–3985 (2015).
29. Guo, X., Zhou, J., Siegler, M. A., Bragg, A. E., and Katz, H. E. *Angew. Chem. Int. Ed.* , n/a–n/a (2015).
30. Molloy, M. S., Snyder, J. A., and Bragg, A. E. *J. Phys. Chem. A* **118**(22), 3913–3925 (2014).

31. Cook, S., Furube, A., and Katoh, R. *Energy Environ. Sci.* **1**(2), 294–299 (2008).
32. Hernandez, V., Castiglioni, C., Del Zoppo, M., and Zerbi, G. *Phys. Rev. B* **50**(14), 9815–9823 (1994).
33. Magnanelli, T. J. and Bragg, A. E. *J. Phys. Chem. Lett.* **6**(3), 438–445 (2015).
34. Bragg, A. E., Yu, W., Zhou, J., and Magnanelli, T. *J. Phys. Chem. Lett.* **7**(19), 3990–4000 (2016).
35. McCreery, R. L. *Raman Spectroscopy for Chemical Analysis*. John Wiley & Sons, New York, (2000).
36. Bernath, P. *Spectra of Atoms and Molecules*. Oxford University Press, Inc., New York, New York, 2nd edition, (2005).
37. Zhao, B., Niu, K., Li, X., and Lee, S.-Y. *Sci. China Chem.* **54**(12), 1989–2008 (2011).
38. McCamant, D. W., Kukura, P., Yoon, S., and Mathies, R. A. *Rev. Sci. Instrum.* **75**(11), 4971–4980 (2004).
39. Kukura, P., McCamant, D. W., and Mathies, R. A. *Annu. Rev. Phys. Chem.* **58**(1), 461–488 (2007).
40. Schott, S., Steinbacher, A., Buback, J., Nuernberger, P., and Brixner, T. *J. Phys. B: At. Mol. Opt. Phys.* **47**(12), 124014 (2014).
41. Tan, H.-S., Piletic, I. R., and Fayer, M. D. *J. Opt. Soc. Am. B* **22**(9), 2009 (2005).
42. Tokmakoff, A. *J. Chem. Phys.* **105**(1), 13–21 (1996).

Chapter 2

Experimental Methods

Methodology was developed and implemented to conduct experiments on materials related to systems described in Chapter 1. Several techniques were adapted from sources for fabricating nanoaggregates or supramolecular assemblies to serve as microcosms of condensed phase behavior and emulate films made of these same materials. The sizes, approximate shape, and dispersivity of aggregates were estimated using either dynamic light scattering (DLS) or transmission electron microscope (TEM) imaging where applicable. These materials were characterized using standard steady state electronic absorption (UV-Vis) from which concentrations could be altered to obtain a particular optical density to suit the experiment at hand and broad comparisons could be made between different samples or those with related solution phase/aggregated preparations. Most experimental proceedings centered around the collection of more intricate spectroscopic data, particularly of ultrafast electronic absorption, vibrational coherences, and polarization anisotropy. Sophisticated equipment and data processing algorithms were utilized to parse, collect, and process the relevant information accordingly.

2.1 Nanoaggregate Synthesis

Nanoaggregates and supramolecular assemblies were prepared for spectroscopic analysis using one of the methods described below. Each description outlines the given technique, including its utilities and to what materials each was applied. Samples were prepared in air and stored in sealed containers in the dark to minimize exposure to air and light. Each sample for which data is presented in this dissertation produced consistent signatures for the duration over which experiments were conducted, indicating little to no degradation due to laser or air exposure or storage times of varying durations. Descriptions of alternative sample preparation techniques explored but not utilized in this work are included as Appendix 8.1.1.

2.1.1 Nanoparticles Formed through Injection Reprecipitation

The formation of nanoparticles through reprecipitation is a standard procedure that has been described elsewhere.¹ Kinetic suspensions rely on trapping pockets of solute of a given (low or high) polarity material within a solvent of the opposite polarity. The goal is to utilize the strength of the surrounding solvent's bonding network to form a shell around small nanoscopic collections of the material and inhibit the material from aggregating further and precipitating on a macroscopic scale. As a result of its strong and intricate hydrogen bonding networks, water serves as an ideal solvent for hydrophobic materials and is the only solvent for which this technique is used in this work. Critical to the method is the means by which the non-polar ma-

terial is introduced into water to form aggregates of an appropriate size (<200 nm) and sufficient concentration. Nominally, this is accomplished by dissolving the material in a solvent of sufficient solubility that is directly miscible with water, i.e. Tetrahydrofuran (THF). 500 μL aliquots of the concentrated sample in THF were then rapidly injected into 5-10 mL of vigorously stirred water to induce nanoparticle (NP) formation. The added THF was then driven off of the mixture by blowing compressed air over the sample; removal of THF promoted long term stability and, for Raman measurements, reduced contributions by the solvent to the fingerprint region (<1600 cm^{-1}). An example preparation of poly-3-hexylthiophene (P3HT) NPs is shown in Figure 2.1.

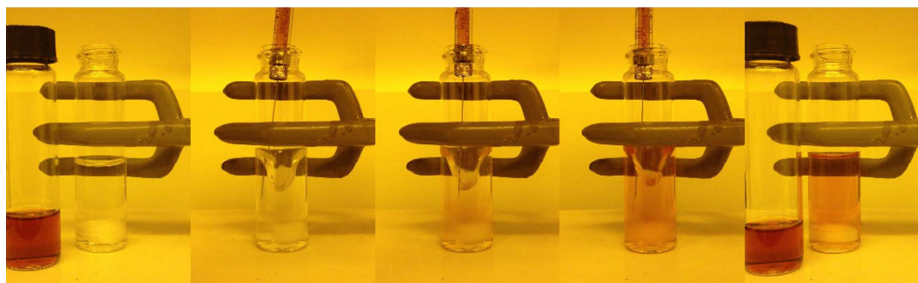


Figure 2.1: Visualization of Reprecipitation: example reprecipitation of RR-P3HT NPs from THF into water, forming a purple kinetically trapped suspension

Optimization of the procedure for suspensions of regio-regular (RR-)P3HT NPs yielded the following considerations. Rapid injections and vigorous stirring were preferred over slower injections and sonication to inhibit formation of macroscopic material in place of NPs by permitting the polymer to be enclosed in water before grouping into larger aggregates or refreshing the solution at the injection site more effectively, respectively. Select RR-P3HT samples were syringe filtered to remove

extraneous macroscopic material, though subsequent improvements to the sample preparation methodology as described above made this step unnecessary. These syringe filters would become plugged up by the polymer, leading to smaller size distributions and dramatically lower NP concentrations. Injecting into less water improves the resulting concentration of NPs but the improvement plateaus at approximately 10:1 H₂O:THF as lower ratios yield a substantial amount of macroscopic aggregation instead. The process is not particularly temperature dependent as samples prepared with and without denaturing RR-P3HT in THF prior to addition were found to yield particles with similar steady state absorbances. However, denaturing the polymer prior to reprecipitation may impact the type or extent of intermolecular packing within particles in ways that UV-Vis measurements may not be sensitive enough to gauge.

The electron acceptor phenyl-C₆₁-butyric acid methyl ester (PCBM) was also occasionally incorporated 1:1 by weight as a co-aggregate to improve charge separation within hetero-domain nanoparticles formed of similar shapes and sizes. TEM reveals that reprecipitated P3HT and PCBM particles blend together as no smaller, more spherical PCBM-only NPs are found when reprecipitating the blend. TEM images also suggest that they form small, indiscernible domains within the same NP rather than as different (adjacent) NPs or ones with larger and very visible domains of P3HT and PCBM.

Several sparged, air-free samples of P3HT NPs were prepared but showed negligible improvement in the quality of their signals or resistance to degradation. As a result, all subsequent samples were prepared open to ambient air. Samples

prepared in this way demonstrated resistance to oxidation and degradation by the laser which did not always correlate with solution phase or film analogues. Generally P3HT showed no oxidative/laser degradation while PTMT showed slight degradation over time. These samples exhibit various lifetimes depending on the stability of the compound and its ability to locate and aggregate with other molecules within solution. P3HT and PTMT samples are stable for months and poly-3-cyclohexyl-4-methyl-thiophene (PCMT) samples were only stable from 1-3 days depending on preparation conditions with a lower shelf life at higher concentrations. In general, this technique creates relatively disordered H-aggregate suspensions and is preferred to films or other aggregates where applicable due to their relatively long shelf life, resistance to laser and air exposure, use of water as a solvent, lack of impedance of Raman features, and ease of preparation. Other aggregate preparation methods and considerations are included in Appendix 8.1.1.

2.1.2 pH-Mediated Peptide Assembly

pH-mediated aggregation was utilized to prepare peptidic supramolecular assemblies of donor-acceptor dyads and mixed energy transfer systems.^{2,3} As the organic chromophores of interest are embedded along peptide backbones, changes in environmental pH can result in the aggregation or denaturing of strands with amino acid moieties located along adjacent strands. At high pH, Coulombic repulsion between carboxylate groups minimizes aggregation. As the pH is lowered and the carboxylate groups are protonated, the Coulombic repulsion is reduced and the materials

self-assemble into intermolecular π -stacked networks that emulate beta sheets. Comparisons of the sample under acidic and basic conditions provide a reasonable approximation to assembled and isolated behaviors of this system, respectively. While the latter is not strictly the case due to some residual interaction between adjacent peptide chains in basic environments, the deprotonation and resulting negative charging of carboxylate groups produces very unfavorable interactions at these sites that prevent nearly all prolonged assembly.

Specifically, (un)assembled dyad suspensions of 0.2 mg/mL dyad/H₂O were prepared by adding several drops of 0.1M NaOH to a stock solution to ensure that the samples were relatively denatured (with pH>10, as a neutral pH promotes some aggregation). The samples were then divided in half, with several drops of 0.1M HCl added to one (such that pH<4) to induce aggregation and an equivalent amount of DI H₂O added to the other to maintain a consistent analyte concentration. These samples yielded dramatically different steady state electronic absorption spectra, indicative of successful assembly. The method is applicable to additional peptidic materials not considered here, and only the samples including oligo-phenylene-vinylene (not discussed in this dissertation) were found to be photosensitive. Figure 5.2b shows an example set of aggregates assembled from one of the dyads (DA-2) considered in Chapter 5.

2.1.3 Nanoparticle Size Characterization: DLS and TEM

Dynamic light scattering is a technique where the frequency of fluctuations in a laser's beam path deflections are autocorrelated and used to estimate the sizes of aggregates within the aqueous medium of interest. The technique provides rapid statistical information about the distributions of sizes of these particles suspended in solution, specifically their hydrodynamic radii (the radius from the center of the particle over which light is diffracted). The technique encounters limitations by overestimating aggregate sizes due to its measurement of excluded volume rather than physical particle size and becomes less reliable when particle shapes are not spheroidal. DLS is also not recommended for samples significantly contaminated by macroscopic material as the fluctuations become too severe and long-lived to be measured accurately. Only a few initially prepared samples were characterized using DLS as TEM provides a more accurate depiction of their shapes and estimation of their particle sizes. These measurements were conducted using a ZEN3600 DLS (Malvern Instruments) and were analyzed with Zetasizer v7.04 software.

Transmission electron microscopy utilizes a focused beam of electrons as an imaging tool with resolution surpassing the diffraction limitations of conventional light based microscopes. The electron beam is focused to a relative tight spot through a sample and then re-magnified and imaged onto a sensitive CCD array. The high energy flux can result in sample degradation but allows examination of particles with single nanometer resolution. Careful alignment and tuning of the instrument are also critical in avoiding astigmatism and anomalous spectral patterns to obtain images of

sufficient quality, but further experimental considerations with regards to the specific microscope are beyond the scope of this section.

Samples studied here were prepared by adhering aggregated particles onto a thin film (≈ 10 nm) of durable polymer (Formvar) coated in carbon and stretched across the openings of a copper grid for support. Grids were positively ionized to promote adhesion. Particles were then adhered to the surface either by inverting a sample onto a droplet of solution containing the aggregates and allowing particles to cling to the surface randomly for ten to twenty minutes, or by allowing a droplet placed on top of the grid to evaporate leaving aggregates behind. The former method yields significantly lower particle densities but also produces more accurate particle shapes by not distorting them through exposure to relatively high concentration, precipitation environments. Certain samples were negatively stained using 0.2% uranyl acetate to provide contrast between them and the predominantly carbon background of the grids. TEM images were acquired using a Technai 12 electron microscope at the JHU Integrated Imaging Center (IIC). The images were processed and analyzed statistically using ImageJ and a homemade LabVIEW visual interface (VI). Individual reprecipitated nanoparticles were found to be 40-140 nm diameter depending on the concentrations of solution in THF used for reprecipitation and with varying degrees of uniformity and circularity depending on the sample considered. Example images that I collected are shown in Figure 2.2 for reprecipitated particles described above, and alternative materials prepared according to procedures described in Appendix 8.1.1 not directly considered here.

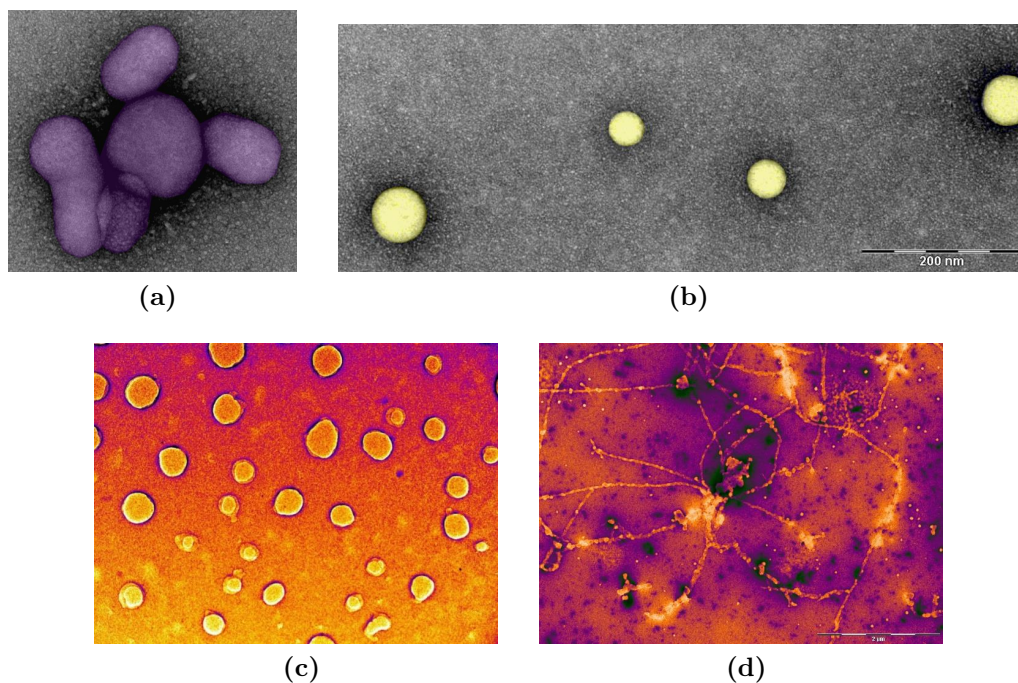


Figure 2.2: Example TEM Images: (a) RR-P3HT NPs, (b) RRa-P3HT NPs, (c) RR-P3HT-PCBM core-shell nanoparticles, and (d) J-aggregated RR-P3HT nanofibers

2.1.4 Sample Steady State Characterizations

One of the simplest ways to characterize a sample photochemically is by measuring its electronic absorption. UV-Vis spectra were collected using one of two diode array spectrometers: a Stellarnet Black C-25 (200-800 nm) or Blue Wave Vis-25 (350-1100 nm) spectrometer in conjunction with either or both of deuterium or tungsten lamp light source. Dark background and references were collected relative to a similar path length cuvette containing a solvent blank where possible and relative to air otherwise. Fluorescence measurements were conducted using a Perkin-Elmer LS-5 luminescence spectrometer, though none are presented within this thesis. These spectra provide an indication of the sample's absorptivity and concentration and allow for excitation wavelengths to be identified and selected as applicable to each sample.

2.2 Ultrafast Spectroscopic Techniques

While ultrafast experimentation does not encompass every spectroscopic tool or method we use, it forms our most substantive and powerful set of techniques for examining systems of interest. These ultrafast experiments can be broken down into the four major types of measurements conducted by our research group, namely transient absorption (TA), femtosecond stimulated Raman (FSRS), pump-re-pump probe (PRP), and broadband polarization anisotropy (BPA) spectroscopies. TA is the most broadly applicable and is used to elicit details concerning populations of electronic excited states as a function of time after photo-excitation. It can also elucidate wavepacket propagation along excited state surfaces, vibrational relaxation, and the kinetics of energy and charge transfer. While TA is useful for information about electronic states and transitions, FSRS is utilized for obtaining vibrational information on an ultrafast time scale. FSRS involves the systematic scattering of light at wavelengths offset from a particular frequency based on the amount of energy deposited into or absorbed from particular vibrational modes. By contrasting signals due to excited states with those of the ground state, it is possible to obtain structural information about the material's transients.

PRP and BPA are more specialized techniques developed and implemented a couple years to expand the foundation of research in the Bragg Lab. PRP extends TA by using an additional photo-excitation pump pulse to either re-excite a particular excited state through resonance with a transient absorption signal or selectively

deplete (dump) the transient population via resonance with a stimulated emission band. Though this methodology was not extensively studied as part of this thesis, it allows for unique and powerful mechanistic conclusions to be drawn in identifying how the populations of certain transients respond to further photoexcitation of itself or other transients, as well as over what timescale photo-generated holes in transient populations can recover. Typically as part of a TA measurement, anisotropic effects imposed by the use of a polarized excitation source are nullified by filtering the probe beam with a wire grid polarizer, (WGP) to be representative of \parallel and \perp components of the polarization by setting the probe polarization to 54.7deg (magic angle, MA) relative to the pump. By contrast, BPA measurements constitute iterative collection of multiple polarization phases (\parallel and \perp or \parallel and MA) to extract information encoded in the directionality and kinetics of the electronic anisotropy. These measurements reflect changes in transition dipole moment following a polarized excitation that are associated with molecular rotation, structural reconfiguration, or transient state migration and localization. Broadband electronic anisotropy is a particularly novel technique as anisotropy measurements have generally been limited to single wavelength probes with only limited instances of broadband collection.^{4,5}

2.3 Laser System Overview

Ultrafast spectroscopic measurements were conducted using the equipment and methodology described here. Laser light necessary for these measurements is generated by fundamental ultrafast laser pulses from a Coherent Ti:sapphire laser

system consisting of a Mantis-5 oscillator and a Legend Elite-USP-1K-HE regenerative amplifier. The oscillator generates a modelocked, ≈ 6 nJ pulse at a repetition rate of 80 MHz with a FWHM bandwidth spanning from 770-855 nm. This pulse train is temporally stretched and used to seed the regenerative amplifier before being re-compressed back to a temporal pulse width of < 40 fs. This results in an 800 nm fundamental pulse with a power of 4.0-4.5 mJ/pulse at a repetition rate of 990Hz. The output beam is then split into several lines to drive various non-linear optical processes for generating the excitation, Raman, and probe pulses (described below) as needed for each type of experiment.

A small fraction of the beam, several hundred nJ, is split off and was focused into a crystalline material to generate a broadband white light continuum (WLC) to serve as each experiment's probe pulse. Sapphire is used for Raman measurements and those probed at wavelengths above 450 nm and while calcium fluoride (CaF_2) is used to extend the probe range further into the ultraviolet (UV). These pulses are generated with 100-150 fs temporal resolution based on cross-correlation measurements conducted with barium borate (BBO) crystals. The pulses are not compressed after generation, and temporal chirp is accounted for through chirp correction procedures as described in Section 2.5.1. Pulses are passed through a WGP set to MA relative to the excitation polarization immediately before the sample to eliminate polarization anisotropy from TA measurements.

BBO crystals are used in a second line to produce photo-excitation (i.e. actinic) pump pulses at harmonic frequencies of the original 800 nm output. Second harmonic generation (SHG) is conducted by passing the 800 nm pulse through a

type I BBO crystal to frequency double the beam to 400 nm with relatively high fluences (≈ 100 nJ/pulse). This pulse is either used as is or temporally and spatially intersected with the original 800 nm pulse in a second, type II BBO crystal to generate 266 nm third harmonic pulses (< 30 μ J/pulse) via sum frequency generation (SFG).

Alternatively, tunable excitation pulses can be generated by passing approximately 1 mJ of the fundamental into a femtosecond optical parametric amplifier (OPA). A Coherent OPerA Solo is the specific model used and is capable of generating actinic pump pulses at wavelengths between 295-2200 nm, using various combinations of non-linear optical processes. Cross-correlation measurements establish the time resolution of these pulses and the harmonic described above to be between 50-70 fs, and thus should not impose a limitation upon time resolution in comparison to the temporal width of the broadband continuum probe.

Finally, the remaining ≈ 1 mJ of the fundamental pulse is dedicated to generating a tunable, temporally stretched excitation pulse for use as the Raman pump in FSRS measurements. Based on the time-bandwidth product, to obtain spectral resolution of < 10 cm^{-1} , a pulse with a temporal bandwidth of > 1.5 ps must be used. To accomplish this, a second harmonic bandwidth compressor (SHBC) stretches the input pulse in time. The SHBC counter-chirps equivalently split portions of the input light which are then recombined in a type I BBO crystal to drive SHG and generate a spectrally narrowed 400 nm pulse with a power of 300-400 μ J and a pulse duration of 4-5 ps. The SHBC also splits a small portion of the input to generate a seed WLC which is routed along with the spectrally resolved 400 nm pulse into a Light Con-

version picosecond OPA (TOPAS-400WL). Within the OPA, a specific visible-near infrared (NIR) frequency is amplified in three stages by the stretched 400 nm pulse using the SHBC's WLC as a seed, to yield a tunable output pulse of approximately 20-50 μJ at 450-1200 nm.

The relative time delay of each pulse is altered by passing each pump pulses necessary for a given experiment off individual translation stages relative to the fixed delay probe. Actinic pump pulses are reflected off corner cubes or mirror pairs placed atop a Newport ILS250CC translation stage, with a maximum (double pass) travel of 1675 ps, repeatability of <1 fs, and a maximum error in beam displacement of 0.022 $\mu\text{m}/\text{ps}$ of travel at the location of the sample (prior to focusing). The Raman pump is passed off of a smaller Newport MFA-PPD translation stage with a maximum delay of 167 ps and significantly improved repeatability in time delay and beam spot location.

Each pump pulse is attenuated to an acceptable fluence for the given experiment (<30 μJ) and placed through a lens of appropriate focal length, generally $4 < f < 25''$, to further control the beam spot size and fluence at the sample. The probe beam is collimated and focused to a ≈ 50 μm spot size at the sample, with the lens of each pump pulse positioned such that their spot sizes are large enough to completely encompass the probe beam (>100 μm). Each beam is selectively blocked at particular frequencies and by an optical chopper to execute the transient spectral acquisition methods described in Section 2.4. The probe beam is then collimated after the sample and passed through several filters to dampen the intensity of fundamental light (800 nm) and remove pump scatter or second order artifacts. The probe beam

is then focused through a slit into a Princeton Acton SP2300 spectrograph and dispersed on a Princeton Pixis 100BR CCD array camera. Each probe pulse produced by the laser is collected individually via a 1 ms acquisition. Fluctuations in probe light intensity are normalized through shot-to-shot signal comparisons, the mechanics of which depend on the details of the experiment.

2.4 Advanced Spectral Collection through Four and Eight Phase Data Acquisition

Several data acquisition modes have been developed to acquire and compute spectra based on the use of successively more complex phase arrangements to automate and improve corresponding results. In the simplest form of a differential spectroscopic experiment, one would measure a continuum of UV-NIR light in the presence of a sample relative to in its absence to determine the molecule's ground state electronic absorption or UV-Vis spectrum. Measuring a transient change in a sample absorbance in response to photoexcitation involves, instead, the comparison of a continuous probe beam in the presence of an overlapping pump beam to its absence. This comparison measures a sample's transient absorption (TA) or its ground state Raman (GSR) spectrum for actinic and Raman excitation pulses, respectively. These spectra can be collected by blocking the pump pulse with a rotating chopper, spinning at a rate in which every other incident laser pulse is blocked, resulting in an 'on, off, on, off...' behavior relative to a constantly present (unblocked) probe. TA spectra

can then be calculated by taking the ratios of each "on-off" pair. The identification of on versus off phases is accomplished through passive monitoring during collection of the camera and optical choppers outputs which are sampled and processed through a digital to analog converter (DAQ) board. Accumulations can be used to increase the number of individual phase pairs averaged or the sum of each phase to be considered (Section 2.5.1) in order to improve the signal:noise ratio (S/N) of collected results.

However, this simple experimental set-up has limited capability. Pump probe experiments carry with them spontaneous emission (e.g. fluorescence) and pump scatter that contribute to artificial signals not strictly resulting from the photoinduced modification of the sample's electronic absorption. For transient Raman, an additional (actinic) pump pulse must be introduced to permit collection of a sample's pump-induced Raman (PIR) spectrum, but TA and GSR spectra must also be measured in order to correct and extract information from the PIR spectrum. PRP and BPA measurements are not feasible without the use of multiple "on/off" phases for the pump(s) and probe beams. The easiest means to achieve this is to include an additional optical choppers to block a second beam at different harmonic frequencies, yielding additional phases.

2.4.1 Fluorescence-Corrected TA (FCTA) and FSRS by Four-Phase Acquisition

Four phase data collection schemes utilize two choppers positioned in front of two different pulses and blocking them at $\frac{1}{2}$ and $\frac{1}{4}$ of the repetition rate of the laser.

This leads to ‘off, on, off, on’ and ‘off, off, on, on’ phase progressions for the two pulses respectively. Each laser shot now represents a unique combination of pulses to be measured that is available for more advanced calculations; these are labeled as phases 1-4. The assignments for each phase from each data acquisition mode are spelled out in Table 2.1. Equation 2.1 below describes how FCTA is calculated and contrasted to ordinary TA. There is no set requirement for which chopper is placed within the path of each beam, i.e. the optical choppers are interchangeable. Positioning one chopper to block the pump, and the other the broadband probe, allows TA data to be collected and modified by phases with no probe present. Correcting for spectral contributions due to fluorescence and pump scatter requires twice as many laser shots to obtain a single TA spectrum, thus decreasing the spectral S/N by a factor of $\sqrt{2}$. Despite this and the more intricate experimental set-up, the removal of fluorescence/scatter features, which often obscure sizable portions of transient spectra is well worth the trade-off. A diagram of the laser table set-up utilized for FCTA measurements is included as Figure 2.3

$$FCTA = \frac{4 - 2}{3 - 1} \quad (2.1a)$$

$$TA = \frac{4}{3} \quad (2.1b)$$

For pump-induced Raman measurements, placing different repetition rate choppers in front of the actinic and Raman beams allows for the four phases to be collected as described in Table 2.1. Comparing pairs of phases allows for spectra useful in iso-

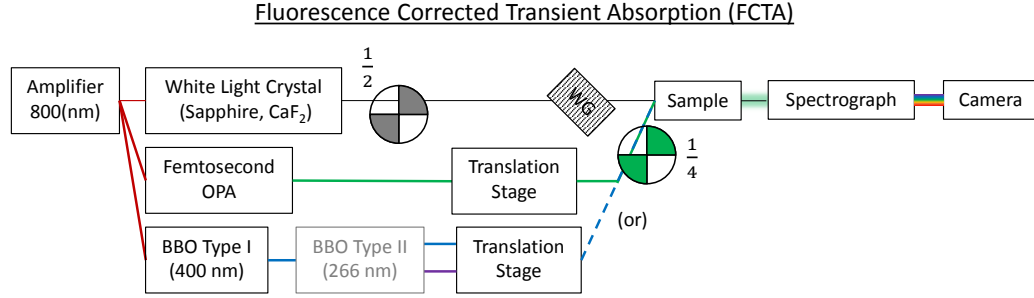


Figure 2.3: Fluorescence Corrected Transient Absorption Experimental Set-up

lating Raman features attributable to specific transients to be determined. Over the sequence of four laser shots PIR, GSR, and TA (limited to the narrow region about the Raman scattering) spectra are all obtained as well as an additional spectrum known as synchronous chop (SC). Removing solvent Raman, GSR, and TA background signatures from either the SC or PIR spectra, permits isolation of the spectral characteristics due only to the resonant transient of interest. In instances where the full spectrum of the transient is obtained, it is labeled as the excited state's pure transient Raman (PTR) spectrum. As all of these component spectra are necessary for PTR extraction and transient mode characterization, four phase collection modes are necessary for a proper FSRS measurements. Schematically, a PRP measurement is synonymous with FSRS, by replacing the Raman pump with a re-excitation pump in each phase, though details of its measurement and implementation are reserved for Appendix 8.1.2. An experimental layout of the laser table used for FSRS is included as Figure 2.4.

$$PIR = \frac{4}{3} \quad (2.2a)$$

$$SC = \frac{4}{1} \quad (2.2b)$$

$$TA = \frac{3}{1} \quad (2.2c)$$

$$GSR = \frac{2}{1} \quad (2.2d)$$

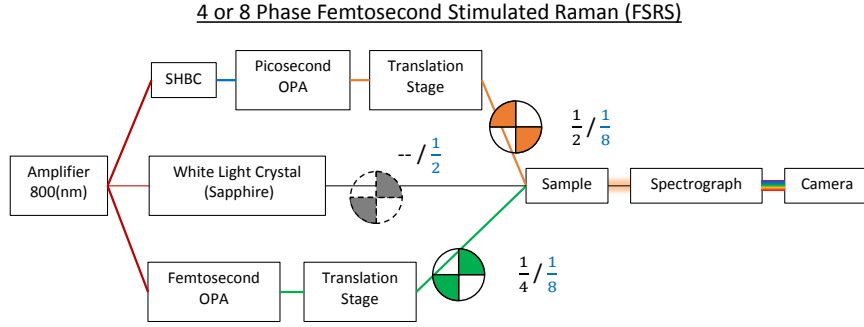


Figure 2.4: Femtosecond Stimulated Raman Experimental Set-up

Typically, FSRS measurements are not impacted by a lack of fluorescence and scatter correction as the narrow region of interest and data collection avoids regions of pump scatter. The complex nature of the broad baseline in a FSRS spectrum, which incorporates spectrally broad features including fluorescence and poorly resolved vibrational modes, necessitates rigorous but often simple correction as described in Section 2.5.1. However, in cases where information about lower frequency modes is desired, eliminating scatter and fluorescence requires an identical set of phases in the absence of the probe to be collected. Additionally, as BPA necessitates the simultaneous consideration of two probe beams with differing polarizations, two separate sets of FCTA measurements must be collected (one for each polarization) suggesting use of

eight total phases. Thus, to incorporate FCTA into FSRS (or PRP) methodology and permit BPA measurements, schemes involving eight phases must be developed.

2.4.2 Eight Phase Measurements: FSRS, PRP, and BPA

As the complexity involved in ascribing additional phases increases, so too does the variability amongst various applications of the set-up. Eight phase measurements still only require two optical choppers, although one must now be slowed to an eighth of the laser repetition rate to yield eight distinct optical phases. The possible chopper repetition rates are now $\frac{1}{2}$, $\frac{1}{4}$, and $\frac{1}{8}$ of the laser repetition rate. For FSRS/PRP measurements, two different schemes are possible and commonly used: the first involves passing one of the three beams (amongst the two pumps and single probe) involved in the experiment through a single phase of the $\frac{1}{8}$ chopper while the other two are passed through adjacent phases of a $\frac{1}{4}$ chopper, while the second involves passing two beams through individual phases of the $\frac{1}{8}$ chopper that are spaced exactly two or six phases apart and the other through a $\frac{1}{2}$ or $\frac{1}{4}$ chopper (though the latter can create issues). Primarily, this allows two pump pulses and the probe to be iteratively blocked at rates that will produce eight distinct phases, enabling the application of fluorescence correction to FSRS or PRP measurements as described in the previous section. Equation 2.3 describes the calculations for each spectrum in this mode.

$$PIR = \frac{8 - 6}{4 - 2} \tag{2.3a}$$

$$SC, \frac{PRP}{P} = \frac{8-6}{3-1} \quad (2.3b)$$

$$TA, \frac{PP}{P} = \frac{4-2}{3-1} \quad (2.3c)$$

$$GSR, \frac{RP}{P} = \frac{7-5}{3-1} \quad (2.3d)$$

BPA can be set-up by using the latter methodology where the $\frac{1}{8}$ chopper to blocks the excitation pulse and the broadband continuum, (two or six phases apart) while using the second, $\frac{1}{2}$ chopper to select between split polarizations of the white light probe. Namely, the use of the BPA experimental set-up diagram, reflective neutral density filter, and wire grid polarizer(s) after the sample (as shown in Figure 2.5) can split the probe light after the sample into near identical spots with information encoded along different polarizations set by each WGP. The two beams are routed along nearly collinear trajectories that will eventually enter the spectrograph/detection set-up but are separated enough to alternately block them using a $\frac{1}{2}$ chopper such that only one reaches the camera on each laser shot. Sequential shots of slower moving phases will encode information due to two different anisotropic states, from amongst parallel, perpendicular, and magic angle relative to the polarization of the excitation source. In this way, polarization anisotropies can be collected at each time delay without having to average and collect a large number of spectra at one polarization before switching to another, by which point the sample, laser, or overlap conditions may have changed (leading to spectral discrepancies not due to anisotropy). The identities math associated with determining each quantity as part of a typical BPA

measurement are included as Equation 2.4.

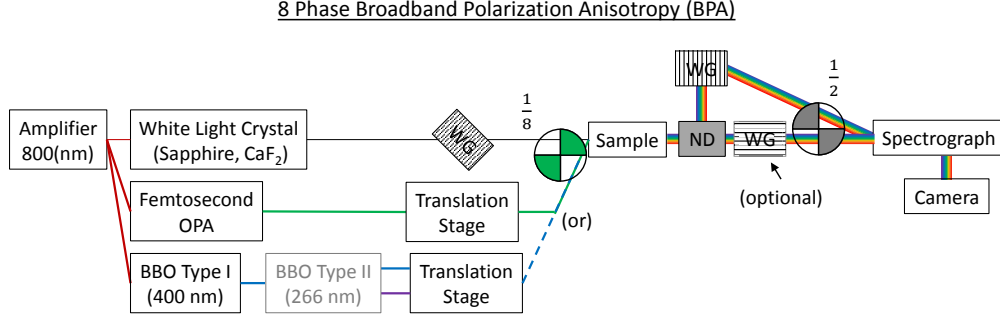


Figure 2.5: Broadband Polarization Anisotropy Experimental Set-up

$$TA_{\perp} = \frac{7-3}{5-1} \quad (2.4a)$$

$$TA_{\parallel} = \frac{8-6}{4-2} \quad (2.4b)$$

$$TA_{MA} = \frac{TA_{\parallel} + 2TA_{\perp}}{3} \quad (2.4c)$$

$$TA_{\parallel}^* = 3TA_{MA} - 2TA_{\perp} \quad (2.4d)$$

$$TA_{\perp}^* = \frac{3}{2}TA_{MA} - \frac{1}{2}TA_{\parallel} \quad (2.4e)$$

$$r_{t,\lambda} = \frac{TA_{\parallel} - TA_{\perp}}{TA_{\parallel} + 2TA_{\perp}} \quad (2.4f)$$

As mentioned in Section 2.2, phases for each mode are monitored passively by digital input/output (I/O) channels that the DAQ uses to sample output pulses from the camera and optical choppers. These phases are read and used to parse which spectra among the progression of camera read-out pulses correspond to each

numerical phase. These phases are then identified by features that are anticipated for each, as shown in Table 2.1 and assigned empirically by the user. For example, in a four phase FCTA measurement of a fluorescent sample, the four phases can be identified based on which show the white light spectrum, fluorescence spectrum, both, or neither. Table 2.1 shows the anticipated pulses occurring within each phase of a particular measurement in which the designations B, P, R, WL, \parallel , and \perp correspond to background, pump, Raman pump (or re-pump), white light, parallel, and perpendicular, respectively. MA corresponds to magic angle, and $r(t, \lambda)$ is the electronic polarization anisotropy.

Phase #	FCTA (4)	FSRS or PRP (4)	FSRS or PRP (8)	BPA (8)
1	B	WL	B	\perp B
2	P	R + WL	P	\parallel B
3	WL	P + WL	WL	\perp P
4	P + WL	P + R + WL	P + WL	\parallel P
5			R	\perp WL
6			P + R	\parallel WL
7			R + WL	\perp P + WL
8			P + R + WL	\parallel P + WL

Table 2.1: Chopper Phase Assignment Table

2.5 Data Processing and Analysis Techniques

Based on these phase assignments, the quantities of each spectroscopic experiment were calculated from Equations 2.1, 2.2, 2.3, and 2.4, corresponding to four phase FCTA, four phase FSRS/PRP, eight phase FSRS/PRP, and eight phase BPA, respectively. All data collection and processing was accomplished using LabVIEW virtual interfaces (VIs) enhanced or created over the course of my dissertation. These

quantities, specifically, are calculated automatically by the LabVIEW data acquisition VI for each accumulation and averaged over the course of several accumulations before moving on to the next delay.

Originally, the data collection VI involved measuring and recording each iteration of each phase, determining the corresponding ratios from individual pairs/sets of spectra, and then average the subsequent ratios within each accumulation. While the process of ratioing, then averaging the resulting (RTA) spectra, as shown in Equation 2.5a below, is the mathematically rigorous approach, it often tends toward $\pm\infty$ with erroneous baselines in regions of low white light intensity. Thus the program was reconfigured to average corresponding phases and then calculate the necessary ratios (ATR) as shown in Equation 2.5b below. While this introduces a slight systematic error, in that the sum of a series of products is not strictly equivalent to a product of the sums of the component numerators and demoninators; however, the error for an average 0.01 optical density (OD) signal was found to be far less than the resolution set by the S/N of the experiment (approximately 0.02 mOD). Extending the usable range of our broadband probes should outweigh the error introduced by not calculating the formally correct quantities, an error minimized by the small magnitude of the typical signal measured (in an absolute sense). Subsequent data and data analysis within this thesis were determined via the ATR method, unless indicated otherwise.

$$RTA\ FCTA = \sum_{i=1}^n \frac{\left(\frac{4-2}{3-1}\right)_i}{n} \quad (2.5a)$$

$$ATR\ FCTA = \frac{\sum_{i=1}^n 4_i - \sum_{i=1}^n 2_i}{\sum_{i=1}^n 3_i - \sum_{i=1}^n 1_i} \quad (2.5b)$$

2.5.1 Spectral Processing and Fitting Algorithms

Each computed spectrum acquired from the ultrafast experimental set-up is saved as a tab-delimited text files and read into stand-alone LabVIEW VIs for data processing. The first step involved smoothing the spectra using a variable Savitsky-Golay filter and subsequently truncating the data to the region of usable white light by inspection. A Savitsky-Golay filter is a built in smoothing function that considers continuous polynomial fits of a particular order and through a number of side points about a given data point (both of which are variable) and is applied to minimize high frequency noise within the data. Smoothing is applied to the extent to which it does not modulate either the height or position of involved signatures, limiting Raman spectra with sharper modes to very low levels of smoothing. Typical orders and numbers of side points for PIR and TA data are 10-4 and 20-4, respectively. From here, the data processing procedures deviate depending on the type of spectra and what information is to be extracted from it.

For TA, PRP, and BPA measurements, the next step is to "chirp-correct" the spectra. As the broadband probe continuum spans a wide range of wavelengths with variable refractive indices through optical materials and solvent, it will exhibit a reasonable amount of temporal (and to a lesser extent spatial) chirp, which causes shorter (bluer) wavelengths to lag relative to longer (redder) wavelengths. This results in kinetics at bluer wavelengths occurring at later time delays than red wavelengths, the extent of which depends on the details of the experimental set-up, e.g. how much glass the probe passed through, the sample thickness, and etc., and can be

anywhere between a few hundred fs and a ps. To account for this, the data must be shifted in time such that the onset of transient signals at each wavelength are initiated and proceed from an identical start time. Depending on the analysis the time of initial signal induction, i.e. time zero (t_0), is set to either the half-rise time or the extrapolation of the peak intensity through the half-rise back to a linearly estimated "starting point" for overlap of the most intense, resolvable transient signal. By default, the former is considered the formal time zero.

Briefly, chirp correction was accomplished by identifying the delay at which the half-rise of the signal occurs at each wavelength and fitting these delays with a function based upon a zeroth order approximation of the behavior of the chirp. Temporal chirp arises mostly due to low (second) order group velocity dispersion (GVD) of the probe beam passing through substrates and solvent and is given by Equation 2.5.1. Applying this fit provided a temporal correction that, when subtracted from the set of collected time delays, would individually and continuously offset each wavelength by a different amount in time. Finally, the shifted data was extrapolated back to a common set of time delays for ease of analysis and plotting, particularly as waterfall plots, two-dimensional plot with spectra collected/measured at different delays overlaid on one another as shown in Figure 3.2. When insufficient chirp signal was available to cover the entire range or excited state dynamics are too convoluted to provide a thorough correction of the initial dynamics, often from signals with delayed induction times, a "chirp file" comprised of a solvent (e.g. H₂O or THF) was collected under identical experimental conditions and used to map out the time dependence of the chirp. As BPA measurements encode different temporal responses (not strictly due to

population kinetics), the chirp correction file of the parallel or magic angle spectrum was applied to both that and the perpendicular spectrum in order to ensure that the two remain identical temporally.

$$\Delta t(\lambda) \propto \frac{a^2}{\lambda} + \frac{b^4}{\lambda} + \dots \quad (2.6)$$

Chirp-correction was not applied to FSRS spectra that cover a significantly smaller spectral window, limiting the extent of temporal chirp across the entire probe window (let alone individual vibrational modes) to less than the time resolution of the experimental set-up (<50 fs). The analysis of Raman spectra (PIR and GSR spectra) is handled as follows after the limited amount of smoothing is applied. Along with the data of interest, a discrete solvent sample was always measured immediately preceding or following a given FSRS measurement with all other conditions kept identical to provide a means to spectrally calibrate the frequencies of observed Raman modes. Typically, chlorobenzene (ArCl) was used for the sharpness and wide range of vibrational modes it contains, though other non-resonant solvents could also serve this purpose. These spectra were compared with known spectra for the molecule and used to calibrate the excitation frequency of the Raman pump, which may deviate from the setting of the ps-OPA. This internal standard provides an accurate measure of the relative frequency shifts (cm^{-1}) that measured features relative to the calibrated pump frequency. From here, features seen within the broad backgrounds of the PIR and GSR spectra, due to Raman and actinic pump induced TA and low resolution

FSRS modes, are fit to a polynomial or spline model and are removed to isolate only the sharp persistent features due to resonant Raman scattering. This process varies dramatically by sample and can also involve subtraction of the solvent spectrum to correct for and eliminate these features from the resulting spectra. This is not necessary for aqueous samples as the Raman bands of H₂O are broad and of minimal intensity.

Resulting TA, BPA, and markers from time dependent FSRS spectra were then further analyzed by applying non-linear least squares fitting models to kinetic traces derived from integrated cuts of certain spectral regions, customized techniques based on singular value decomposition (SVD), or Gaussian peak modeling to spectra converted to component frequencies. Details associated with each specific technique are included accordingly in each chapter. Generally, kinetic fits involve applying a customized function comprised of a discrete number of exponential decays, rises, constant offset, and (occasionally) a stretched exponential function to relative intensities plotted as a function of time. Instrument response is modeled by multiplying an error function (commonly referred to as an erf) by this customized function and fitting its width and offset and model parameters simultaneously. An error function is the integration of a Gaussian, the anticipated intensity profile of our excitation source, and provides a good approximation to the onset transient signals in response to photoexcitation. While it is not equivalent to a direct convolution of the instrument response with the exponential decay model, the difference is quantitatively negligible for timescales >1 ps and only systematically/predictably less accurate for timescales below this threshold. Convolutions were often plausible but not applied to kinetic fit

models to reduce convergence times for more complicated models.

2.5.2 Error Propagation and Uncertainty Predictions

The data collection VI outputs errors associated with each set of spectra as a function of wavelength, by calculating the standard deviation associated with each raw spectrum or calculated ratio. Optionally, these can be used to predict uncertainties in individual results as necessary. Inaccuracies in Raman frequencies and absolute polarization anisotropies largely stem from these along with sample collection noise. Presented errors, however, were often associated with parameters determined by the non-linear least squares fitting of kinetic decay traces from integrated regions of a particular spectra, in which the uncertainty resulting from the fit dramatically outweighed that of the individual data points. In that case, each model was constrained and re-optimized by setting the parameter of interest to fixed values offset from the converged solution. A mapping of the X^2 of these fits as a function of the considered lifetime or pre-exponential generates an anharmonic well representative of how precisely converged the parameter is. F-distribution thresholds were determined for how many degrees of freedom/parameters are available to and used by the model. Locating the parameter values over which the X^2 wells cross these critical values allowed for confidence intervals of those parameters to be extracted.⁶ This is more accurate than relying on the linear least squares error predictions provided by many standard software packages and is mathematically rigorous in determining whether or not a particular model is necessary for fitting the system of interest.

2.6 Acknowledgments

Dr. Julie Bitter and Miranda Gallagher assisted in the collection and work-up of these DLS results. Dr. Michael McCaffery and the IIC staff instructed me on how to use the TEM and worked with me to collect images of sample studied earlier on.

References

1. Shimizu, H., Yamada, M., Wada, R., and Okabe, M. *Polym. J* **40**(1), 33–36 (online November 13, 2007).
2. Sanders, A. M., Magnanelli, T. J., Bragg, A. E., and Tovar, J. D. *J. Am. Chem. Soc.* **138**(10), 3362–3370 (2016).
3. Ardoña, H. A. M. and Tovar, J. D. *Chem. Sci.* **6**(2), 1474–1484 (2015).
4. Takaya, T., Hamaguchi, H.-o., and Iwata, K. *The Journal of Chemical Physics* **130**(1), 014501 (2009).
5. Tice, D. B., Weinberg, D. J., Mathew, N., Chang, R. P. H., and Weiss, E. A. *J. Phys. Chem. C* **117**(25), 13289–13296 (2013).
6. Seber, G. A. F. and Wild, C. J. *Nonlinear Regression*. John Wiley & Sons, Hoboken, New Jersey, (2003).

Chapter 3

Time-Resolved Raman Spectroscopy of Polaron Pair Formation in Poly(3-hexylthiophene) Aggregates

3.1 Abstract

The ultrafast formation of bound charge pairs, or polaron pairs (PPs), in mixed-order poly-3-hexylthiophene (P3HT) aggregates was investigated using femtosecond stimulated Raman spectroscopy (FSRS). Spectral dynamics in the carbon-carbon stretching region reveal a significant photoinduced depletion in steady state features associated with lamellar stacked, ordered polymer regions upon visible photoexcitation. This precedes the appearance of red-shifted vibrational features attributable to PPs by a few hundred femtoseconds, which subsequently decay with concomitant recovery of the steady state Raman depletion over a few picoseconds. The pure transient vibrational spectrum of PP exhibits a modest red shift (15 cm^{-1}) and lower Raman activity relative to steady-state features in the C=C stretching region but is notably similar about other modes. In total, this project demonstrates the potential of time-resolved Raman as a morphologically selective and structurally

sensitive probe for tracking ultrafast charge separation and recombination dynamics within polymer regions of conjugated materials. Comparable and opposing results in structural markers of isolated polaron transients for aggregates of different types of order indicated the applicability of the methodology to other transient states.

3.2 Introduction

Organic photovoltaics (OPVs) assembled from conjugated polymers continue to present an alluring alternative technology for solar-energy capture because of the promising processing advantages they offer relative to other photovoltaic materials.¹⁻³ However, a significant shortcoming of these materials stems from variations in intermolecular ordering (or morphology) that pervade organic films and aggregates. Variations in intermolecular order result in domains characterized by different types and distributions of trapping, recombination, and annihilation sites for photoinduced excitations (excitons) and charged transient species, thus affecting charge transport and OPV device properties nonuniformly.⁴⁻⁶ A challenge with OPVs is to identify how domains characterized with different types or degrees of intermolecular order affect specific steps within each relaxation mechanism following photoexcitation and, likewise, the nature of pertinent transient species. Once these dependencies are identified, it may be feasible to eliminate, minimize, or balance the impact of interactions that are detrimental to specific energy- or charge-transfer pathways through judicious choice of material preparation conditions or constituents.⁷⁻¹¹

Numerous insights can be gleaned about how morphology impacts the kinetics

of excited states and charges through transient electronic behaviors.^{12–15} Under low light fluences, similar to those of ambient sunlight, excitation of poly-3-hexylthiophene (P3HT)’s broad visible absorption band promotes the polymer to its lowest-lying singlet state, a bound charge-pair exciton.^{12,16,17} Polymer excitons relax by migrating along or between polymer chains toward lower-energy sites where they become trapped and localized on a sub-picosecond time scale.^{16–19} The spatial extent and reactivity of excitonic states are highly dependent on the intra- and intermolecular order of the polymer, as well as the prevalence and nature of nearby charge acceptors.²⁰ Photoexcitation of neat aggregated regio-regular (RR)-P3HT may also lead to the formation of isolated charge separated transients, namely polarons and locally coupled charge pairs (PPs), and each of these transient species has distinctive spectroscopic features and kinetics.^{12,21–24}

Polaron and PP yields are generally small at low excitation fluences, though the initial population of PPs varies superlinearly with photoexcitation intensity. This occurs because at higher fluences, as the density of singlet excitons prepared increases, the ultrafast annihilation of two such states yields an exciton with much higher excitation energy.¹² The excess energy and more pronounced charge-transfer character of the resultant exciton facilitate its relaxation into charge-separated states, specifically PPs.²⁵ Although the presence and role of PPs in an OPV device under ordinary operating conditions (i.e., low light fluences) are negligible, PPs nevertheless serve as a valuable subject for interrogating singlet-singlet interactions and migration length scales, as well as how morphology influences charge-pair formation and recombination in conjugated polymer materials.^{12,23,26}

Spectroscopically, the PP exhibits an absorption band peaking near 650 nm, which overlaps with both the polymer’s ground-state bleach (GSB) and stimulated emission (SE), the two of which range from 400 to 700 nm. The isolated polaron absorption peaks in the near-infrared (NIR) at 1000 nm, and the singlet exciton absorption band occurs further into the NIR, peaking near 1200 nm.^{12,23} The population kinetics of PPs within films have been characterized from the dynamics of this feature, which exhibits a combination of ultrafast exponential and stretched-exponential decays; this behavior reflects a variation in charge recombination time scales given the distribution of nascent PP energies and the heterogeneity of polymer films. The relative prominence of subpicosecond to longer time scale decays depends on excitation fluence, with higher fluences favoring more rapid decay.^{12,14,21,22} PPs that recombine cannot regenerate the lowest-lying singlet excited state, as was originally supposed; instead, this species invariably reverts to the ground state of the polymer upon recombination.²⁷

Previous works have suggested a correlation between the prevalence of morphologically well-ordered regions within the polymer film and the formation of the PP and isolated polaron species.²³ The polarization anisotropy of PPs formed by SE annihilation is quite large immediately after formation with $r_0(t) = 0.35$ in region-random (RRa)-P3HT. This suggests that the direction of the transition moment is essentially conserved through annihilation and the most rapid encounters of exciton pairs occur in ordered polymer regions.¹² Additionally, tuning to lower excitation energies has been shown to dramatically increase the efficiency of generating charge-transfer states in aggregated P3HT films, a further sign that selective excitation of

more ordered polymer domains likely has a significant role in their formation.²² A relationship between morphology and the formation of PPs and stability has also been suggested by recent work with highly controlled J- and H-aggregated polymer nanofibers.²³ Despite these promising correlations, electronic spectroscopy has limited photoselectivity for probing intermolecular order and is not able to directly interrogate the structural characteristics of PP states and the nature of polymer regions in which they are formed.

On the other hand, photoselective vibrational probes hold promise for direct spectroscopic characterization of the local molecular ordering that underlies the properties and dynamics of transient states generated after photoexcitation.^{28,29} Specifically, Raman spectroscopy is sensitive to variations in intermolecular order and charge separation and serves as a direct tool for evaluating the properties of transient states and the morphological characteristics of material regions in which they are formed.

Raman spectroscopy is a natural probe for interrogating conjugated polymers and their transient states and has been used extensively to characterize both amorphous and aggregated polymers and polymer-based materials.^{30–33} Conjugated polymers generally have strong Raman activity along in-phase, intra-ring C=C and C-C stretching modes owing to large structural displacements between the ground and excited/charged states.³⁴ Raman spectroscopy has been demonstrated to be a sensitive probe of intermolecular order, particularly in conjugated materials, with a few groups reporting morphological dependencies in the steady-state Raman spectra of P3HT films.^{31,33} Significant differences have been observed in the Raman spectra of P3HT films characterized by different degrees of polymer regioregularity, anneal-

ing, and doping with electron acceptors, e.g. phenyl-C₆₁-butyric acid methyl ester (PCBM); lower C=C stretching frequencies are consistently observed with films prepared under conditions that promote assembly of ordered polymer domains, e.g. through lamellar stacking.^{31,33,35–38} A general explanation for these variations is that higher intramolecular conformational order is obtained in accordance with higher intermolecular ordering, resulting in an overall greater delocalization within constituent polymers and corresponding softening of the C=C stretch potential.^{33,39} The sensitivity of this mode to discrepancies in intermolecular order and excited-state or charge (de)localization implies that time-resolved Raman spectroscopy should provide a valuable probe of the nature of photoinduced transient states in polymer materials.

This chapter specifically makes use of femtosecond stimulated Raman spectroscopy (FSRS) to characterize the vibrational signatures of transient species in aggregated polymer materials. FSRS has been described extensively elsewhere,^{40,41} and has been previously applied by our group to interrogate conformational dynamics of photoexcited amorphous polymers in solution.^{42,43} FSRS holds a number of advantages relative to spontaneous Raman spectroscopy described in Section 1.2.2. These include an effective decoupling of time and frequency resolution⁴¹ and the ability to utilize resonance enhancement in order to photoselectively interrogate the transient PP state. Herein is presented a study of the spectroscopy and formation dynamics of coupled charge pairs or PPs, generated upon photoexcitation of aggregated RR-P3HT using time-resolved Raman spectroscopy.

3.3 Experimental Methods

RR-P3HT was obtained from Rieke Metals (#4002-E and #RMI-001E) and used as received. Nanoparticles (NPs) were prepared via the reprecipitation method (from Section 2.1 by rapidly injecting two aliquots of 500 μL of 0.1 wt% P3HT in THF into 10 mL of vigorously stirred water. All samples remained stable and unchanged for the duration over which measurements were conducted. The size, shape, and uniformity of NPs were assessed using both transmission electron microscopy (TEM) and dynamic light scattering (DLS). Samples for TEM analysis were adhered to formvar-carbon grids and subsequently reversed stained using 0.2% uranyl acetate to provide better contrast between the NPs and the primarily carbon background. TEM images were acquired using a Technai-12 electron microscope.

Transient absorption (TA), and pump-induced Raman (PIR) FSRS measurements were conducted as detailed in Section 2.2 and 2.4. 500 nm was selected as the actinic excitation wavelength, while 643 nm was selected as the Raman excitation wavelength to overlap with the anticipated peak of the polaron pair absorptive feature. In power dependent measurements, the intensity of the actinic pump was measured through examination of the simultaneously collected transient absorption profile, to serve as an internal standard (rather than relying on measurement of pump scatter). Each time delay and intensity dependent pump-induced Raman (PIR) spectrum was scaled relative to the peak intensity of the simultaneously collected, ground state Raman (GSR) spectrum to account for fluctuations in the Raman excitation

pulse intensity across multiple scans.

3.4 Results and Discussion

3.4.1 Steady State, GSR, and TA Considerations

Figure 3.1 displays steady state measurements taken of reprecipitated RR-P3HT NPs studied throughout this work. Figure 3.1a displays the cumulative size distribution determined for the primary sample examined and includes an example TEM image as an inset. Sampling over several TEM images revealed a distribution of particles 59 ± 22 nm in size. Particle sizes obtained are comparable to what has been reported in the literature for similar sample preparation conditions.^{9,44} Steady-state spectroscopy of NP samples reveals their photophysical similarity to drop-cast polymer films. A comparison of the UV-vis spectrum of a typical RR-P3HT NP sample with that of the same amorphous polymer isolated in solution is presented in Figure 3.1b and highlights the resemblance of the electronic absorption of NPs to that of polymer films.⁴⁵ In both cases, the absorption band is significantly red-shifted and exhibits vibrational structure not found in the spectrum of the isolated polymer.³³ These features of the steady-state spectrum have been explained previously and reflect the predominant formation of regions of polymer H-aggregates via both methods.^{45–47} Figure 3.1c displays the steady-state preresonant GSR spectrum of the NP sample collected as part of a FSRS measurement using 643 nm Raman excitation. Bands are observed at similar frequencies as have been observed previously in the steady-state

Raman of polymer films.^{5,33} Assignments for all features are made by comparison to theoretical calculations and previous findings⁴⁸. The modes showing the most significant Raman activity and sensitivity to charge separation and morphology are highlighted in the high frequency region of the spectrum. These features, of greatest relevance to this study, are the intra-ring C-C stretching mode at 1360 cm^{-1} and C=C totally symmetric stretching or “ring-breathing” mode at 1440 cm^{-1} . Importantly, these features appear at frequencies characteristic of ordered (lamellar-stacked) polymer aggregates and also exhibit a similar peak intensity ratio ($I_{C-C}/I_{C=C} = 0.34$) as that observed via preresonant Raman excitation of ordered polymer regions (shown to be ~ 0.30).³³ Hence, we conclude that the 643 nm Raman excitation wavelength likewise is preresonant with ordered polymer regions within the NPs.

NPs are also notably similar to polymer films in their transient spectral dynamics (TA signatures) upon electronic excitation.^{23,24} Figure 3.2 plots the transient spectral dynamics as probed in the visible after photoexcitation at 500 nm with a “high” excitation fluence of 0.17 mJ/cm^2 . The negative signal below 600 nm corresponds with bleaching of the polymer’s steady-state absorption spectrum (GSB) and reflects signatures of the vibronic progression of ordered aggregates. The positive signal above 600 nm corresponds to absorption of photoinduced transients, which consist of overlapping contributions predominantly from the PP, but also from the polaron and single exciton that exhibit absorption peaks further into the NIR. The spectral dynamics observed in the (primarily) PP signal at this fluence is similar to what has been observed when exciting polymer films at similarly high fluences, namely that the PP band decays predominantly on a timescale of a few ps.^{12,21,22,27} Addition-

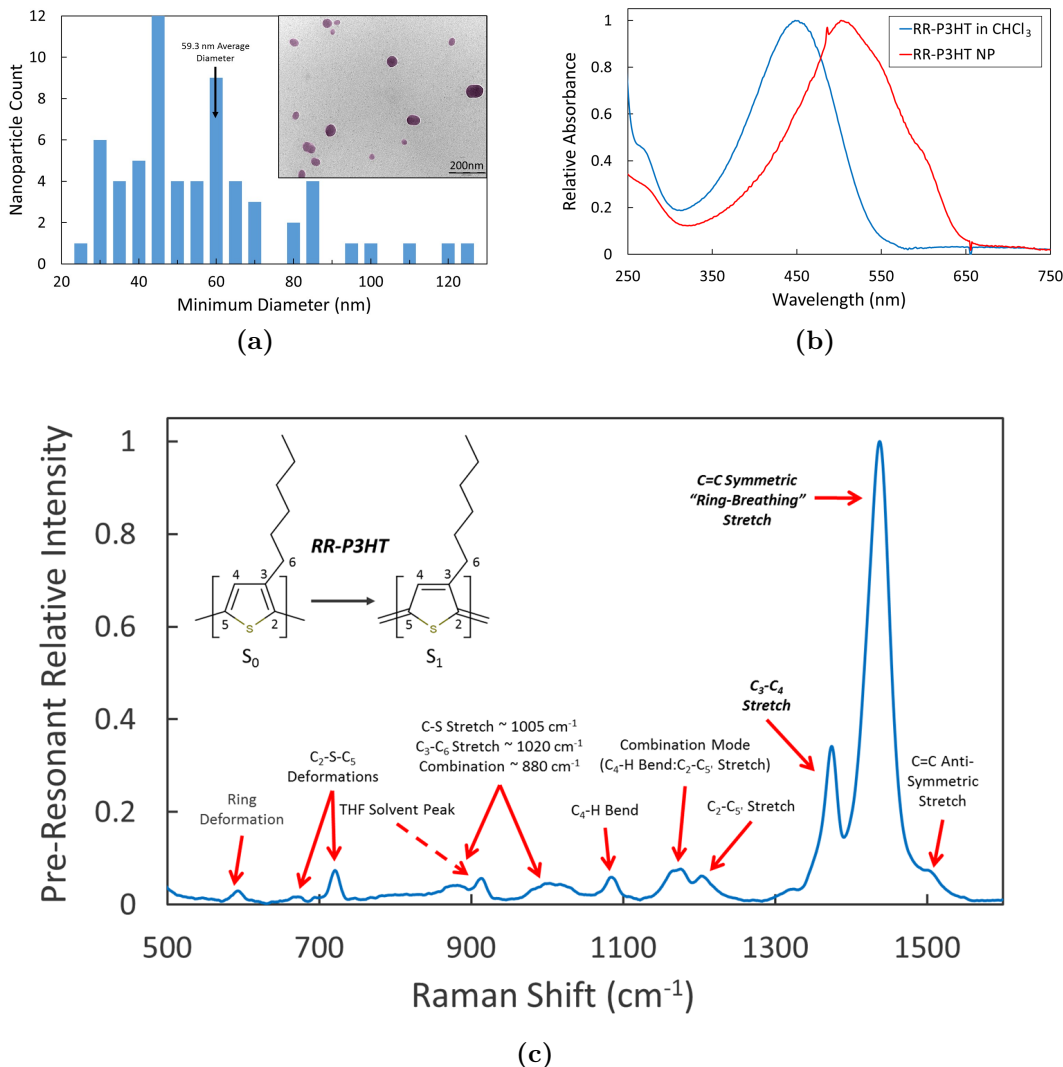


Figure 3.1: Steady State RR-P3HT NP Characterizations: (a) RR-P3HT reprecipitated nanoparticle size (particle diameter) histogram with an inset of a representative TEM image used in sampling sizes and colored for effect, (b) steady state UV-Vis comparison of RR-P3HT dissolved in solution to reprecipitated NPs scaled relative to the size of each visible absorbance feature, and (c) GSR spectrum for RR-P3HT NPs with labels indicating the identity of each band confirmed by comparison to ab initio calculations and previous findings.⁴⁸

ally, ultrafast spectral dynamics are captured in the first few hundred fs following excitation, which show a rapid increase in TA signal at long wavelengths (>650 nm) and concomitant decrease in their GSB intensity. This behavior is a signature of the exciton annihilation process that creates some portion of the PPs. As two excita-

tions meet within the aggregate, they interact energetically to form a single, high energy, exciton that subsequently charge separates; this reduction in the number of excitations induces a fast bleach recovery in addition to the disappearance of exciton absorption at longer wavelengths as charge-separated pairs are formed. Recently, it has also been suggested that transient decay near 700 nm may be associated with an unstable, short-lived PP species.²³ On longer time scales (10s-100s of ps), the transient signature of the PPs decays, as the GSB recovers; this process is accompanied by a red shift in the wavelength at which the spectrum crosses zero ΔOD (605 to 640 nm) and reflects a small fraction of longer-lived charge separated polarons remaining once the PPs have relaxed and recombined. The fluence dependence of PP kinetics in photoexcited NPs are similar to those previously observed in films.^{14,21,27}

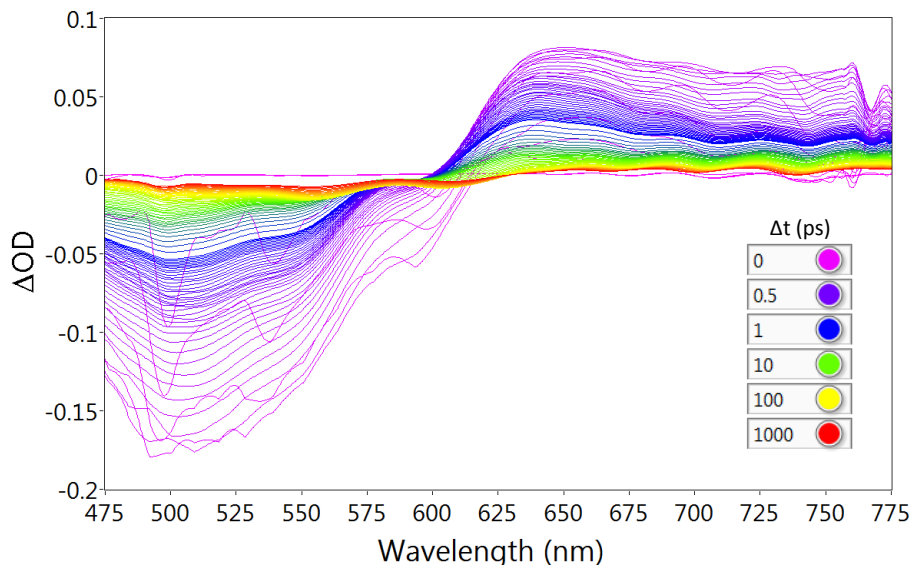


Figure 3.2: RR-P3HT NP Transient Absorption Spectra

Time-resolved Raman spectroscopy presents a new perspective on PP formation by serving as a selective and nuclear probe of the bleaching of polymer domains

associated with PP formation. Figure 3.3 displays a contour plot of the NP PIR spectrum in the region of the highlighted C-C and C=C stretching modes as a function of time after 500 nm photoexcitation, using the same 643 nm Raman excitation wavelength to resonantly and photoselectively interrogate the vibrational spectroscopy of the PP transients. Spectral dynamics reflect a marked decrease in the totally symmetric C=C and C-C stretch intensities immediately following the actinic photoexcitation at 500 nm (1 to 2 in Figure 3.3), which is depleted by $\approx 40\%$. This decrease is comparable to the magnitude in GSB observed from TA measurements, and is sensible given that high fluence laser pulses are used to produce the high excitation density necessary for efficiently forming PP transients. Both the C=C and C-C stretches exhibit a noticeable spectral red shift that lags depletion of ground-state features (2 to 3). These shifts rebound and recover most of their original shape and intensity within a few picoseconds, with a smaller fraction recovering beyond 100 ps (3 to 4). A slight, incomplete recovery in spectral intensity by 400 ps is most likely the result of localized trapping of longer-lived charge-separated pairs (polarons) also created under high-fluence excitation, as is also evident from absorption transients shown in Figure 3.2.

3.4.2 Time Dependent FSRS and Kinetic Markers

The spectral dynamics observed via time-resolved PIR are much more subtle than those observed in TA spectra; yet, spectroscopic markers and trends encompassed within the intensities and peak positions of resonant vibrational modes make

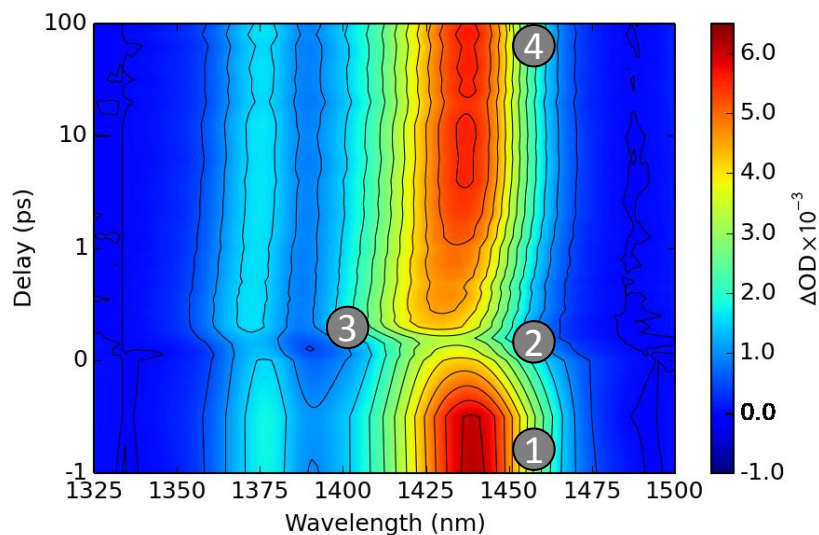


Figure 3.3: RR-P3HT NP PIR Contour Plot: contour plot of PIR spectra collected from a prototypical FSRS measurement reveal a noticeable bleach and shift of the two primary vibrational modes. The latter is offset from the former in maximum amplitude by ~ 100 fs.

it possible to decipher the polymer's underlying kinetics. Although a mere depletion of the PIR relative to the GSR signal would indicate only an excitation-induced reduction in the effective ground-state population, the measurable frequency shift observed in Figure 3.3 indicates that two species, states, or morphologies must contribute to the Raman spectrum in this region. A frequency shift could be expected if photoexcitation at 500 nm preferentially depleted ordered versus disordered polymer regions of NPs (or vice versa), provided that the steady-state Raman spectrum is inhomogeneously broadened by variations in morphology. Although this scenario would formally involve two motifs, it cannot underlie the progression in Figure 3.3 for two reasons. First, the low energy (red) Raman excitation wavelength used here preferentially probes the ordered lamellar-stacked regions of the unexcited polymer aggregates, and we therefore expect that the GSR spectrum should include a set of

features only from this polymer morphology.³³ Second, selective depletion of one type of morphology over another upon photoexcitation would result in a simultaneous decrease in intensity and shift spectrally. However, the Raman signal depletion and red shift observed here are offset from one another in time. The largest Raman depletion occurs at an earlier delay than the maximum frequency red shift, as demonstrated the highlighted points and contours of Figure 3.3. Thus, the data shows consistency with the delayed appearance of a new set of vibrational features arising from the nascent, transient PP state that is superimposed on top of the depleted spectrum of unexcited NPs.

Assignment of these spectral dynamics to the formation and transient decay of PPs is supported by correlations between the TA and time-resolved PIR measurements. Figure 3.4 plots the relative intensities of integrated segments from regions in the broadband TA measurements associated with the GSB and PP TA against the relative time-dependent changes in the C=C feature intensity and frequency shift from the accompanying PIR spectra. Both the GSB and C=C depletion intensity decrease quickly during the first ≈ 200 fs, followed by slower intensity decay on longer time scales. This time dependence is consistent with the description of the transient spectral dynamics in Figure 3.2. On the other hand, the integrated PP TA and the Raman frequency shift do not exhibit the same ultrafast signal induction and only decay on longer time scales.

Figures 3.2, 3.3, and 3.4 demonstrate that correlations between FSRS and TA measurements support a common kinetic description of PP formation in aggregated polymer. Furthermore, FSRS measurements provide an additional perspective on the

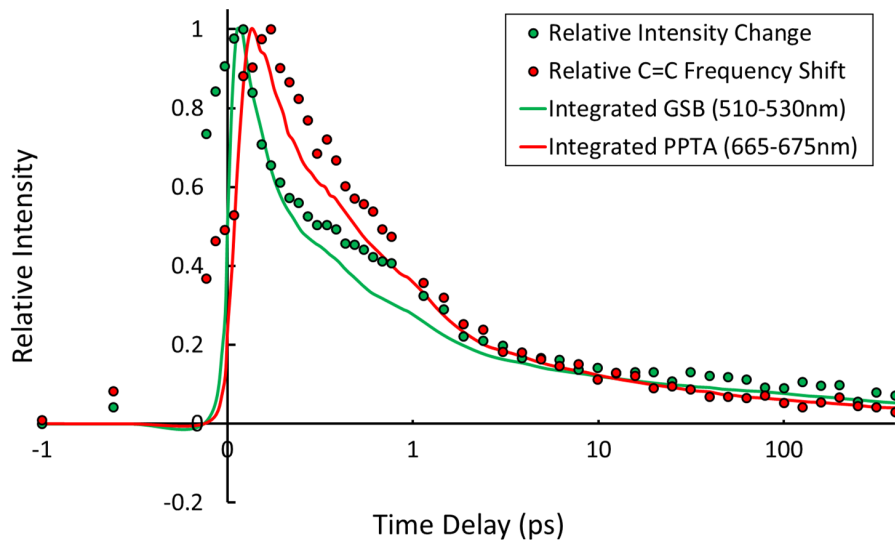


Figure 3.4: RR-P3HT NP PIR Kinetic Markers vs. TA Comparison: comparisons between TA (line) and PIR (dot) features ascribed to depletion of the ground state population (GSB, green) and population of the transient polaron pair state (PP TA, red).

mechanism of PP formation. The enhanced photoselectivity of Raman measurements to morphological order of the unexcited polymer compared with electronic absorption enables more direct observation of the relationship between the formation of PPs and a specific morphology within the mixed-order aggregate. Figure 3.3 demonstrates that the delayed appearance of transient Raman features in the C=C and C-C stretching region is followed by their concomitant relaxation and a recovery of the depletion in the Raman spectrum of unexcited polymer aggregates. As 643 nm is only selectively pre-resonant with ordered regions of the polymer and is resonant with absorption of the PPs, the correlation between the appearance and decay of transient PP Raman and the transient GSR depletion reflects that PP formation is directly linked with ordered polymer morphologies.

3.4.3 Extraction of PTR Raman Spectra of RR-P3HT PP and Related Transients

Raman spectroscopy also provides a new perspective on the properties of transient charge-separated states of aggregated polymers. Here, the pure Raman spectrum of PPs was obtained through spectral analysis of a progression of Raman spectra collected at various photoexcitation intensities. Figure 3.5a plots the pump-induced Raman (PIR) spectrum of RR-P3HT NPs as a function of approximate pump-pulse intensity and illustrates a decrease in the C=C and C-C stretching frequencies with increasing pump power when measured 350 fs after 500 nm actinic photoexcitation. Much like the time-dependent data in Figure 3.3, a spectral shift is observed as the photoexcitation power is increased; this shift can be quantified against the concentration of PPs generated, as shown in Figure 3.6a. Here, the shift has been specifically plotted against the simultaneously measured TA to serve as an internal standard of PP concentration. If the Raman frequency shift arises from a population-dependent superposition of ground-state and PP features then it would make sense for the progression to correlate roughly linearly with absorbance. However, Figure 3.6a illustrates that the pump-intensity dependent frequency shift observed deviates from linearity slightly at sufficiently high PP absorbances and that the trend is best fit by a saturation model rather than a linear one. This saturation likely stems from experimental considerations for the three-pulse FSR measurement that become relevant at higher pump fluences, including intensity-dependent variation in the actinic pump penetration relative to the region of the sample that overlaps with the Raman excitation

beam (as this beam transmits through the entire sample).

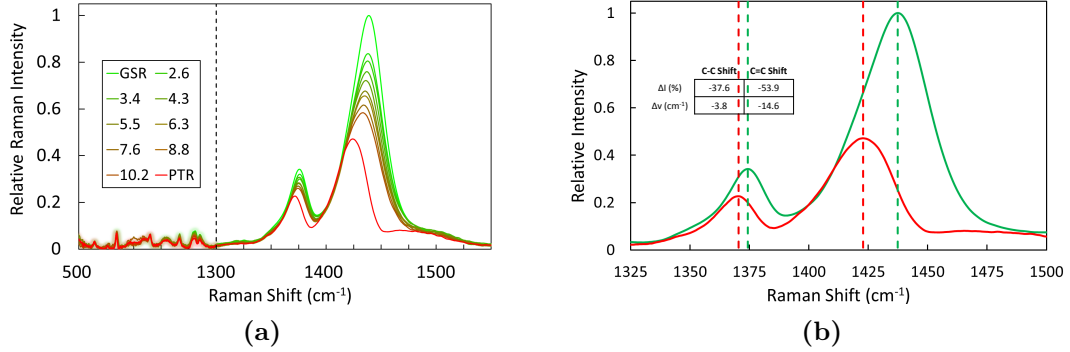


Figure 3.5: RR-P3HT NP Intensity Dependent PIR Spectra: (a) progression of PIR spectra collected for different pump intensities plotted along with the averaged GSR and extracted PTR spectra (b) comparison of average GSR and extracted PTR spectra with intensity and frequency shifts

Despite this, the saturation of the Raman shift with increasing TA signal enables the use of a saturation model to extract a pure PP Raman (PTR) spectrum from the intensity-dependent Raman progression as highlighted by Figure 3.5b. Spectral variations with intensity were analyzed using singular value decomposition (SVD),⁴⁹ with a thorough description provided elsewhere.⁵⁰ Here, SVD extracts a pseudo ground state (PGS) spectrum, which resembles the average GSR, and a difference function (DF) spectrum, which is weighted and added to the PGS in linear combination to recover each intensity-dependent PIR spectrum as a function of pump fluence. This fitting procedure provides relative weights of these two for each spectrum, and applying a saturation model to them permits extrapolation of the PP PTR spectrum. Trends in the PGS and DF weights versus TA intensity are plotted as Figure 3.6b. Among the models considered, the power saturation model gives the best residuals and most rigorous end point prediction; nonetheless, all models gave rise to qualitatively similar predicted spectra.⁵⁰

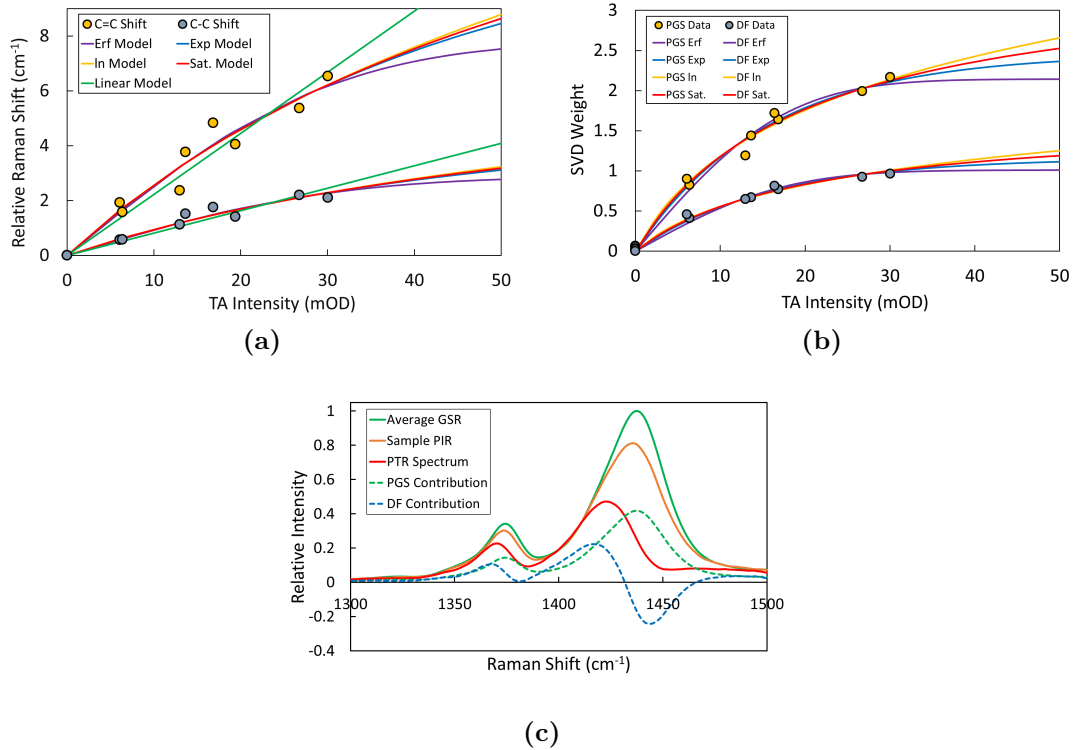


Figure 3.6: C=C and C-C Shifts and SVD Component Plots of RR-P3HT NP PIR: (a) frequency shift (cm^{-1}) of C=C and C-C stretching modes as a function of TA signal intensity fit with a linear and various saturation models, (b) PGS and DF SVD components plotted as a function of TA signal intensity and fit with different models of saturation, and (c) spectra of GSR, prototypical PIR, and PTR with SVD components combined to produce it

The PGS and DF components and resulting PTR spectra are compared to the average GSR and an example experimental PIR spectrum and plotted together in Figure 3.6c. The PTR spectrum of the RR-P3HT PP and GSR spectrum exhibit several differences as seen in Figure 3.5b, primarily that the former is red-shifted and less intense relative to the latter. The symmetric C=C and C-C stretching bands in the Raman spectrum of the PP extracted from SVD are red-shifted by 15 and 4 cm^{-1} while their intensities are 54 and 38% lower relative to the steady-state GSR spectrum, respectively. Additionally, the overall spectral shape in the C-C/C=C stretching region is largely maintained in the PP state, with only a modest 2.3 cm^{-1}

decrease in C=C stretching bandwidth and a slight increase in the ratio of C-C/C=C stretch intensities from 0.34 to 0.48. Finally, there is little other evidence of structural modulations as there are only minimal changes in less intense vibrational features outside of the C-C/C=C stretching region as seen in Figure 3.5a.

Although the significant reduction in the spectral intensity for the PP compared to that for the ground-state polymer provides evidence about state-dependent Raman cross sections, quantitative assessment of PP and ground-state populations and relative cross sections is difficult given the entangled nature of these parameters and further complications involving differences in enhancement conditions (resonant versus preresonant respectively). A smaller Raman cross section for the PP's PTR spectrum would not be surprising as the Raman transition from the PP is determined through resonance with a higher-energy state. This could serve to diminish its coherence lifetime and deplete its signal relative to the ground-state polymer's transition which occurs by way of a bound excited state, and persist with a lifetime that exceeds the duration of the Raman excitation pulse. Excitation to this higher-lying state is also anticipated to induce further charge-pair separation, hence, limiting resonant enhancement as a result of the dynamics of the PP in a higher-lying resonant state. An additional consideration is that the extracted PP PTR spectrum is predictive of how a spectrum of saturated depletion of the GSR, rather than an entire conversion to population of PP states, would look. Thus the intensities in the resulting spectrum are scaled by the net yield of PPs compared to other non-resonant states, a factor which could skew its intensity lower than a pure, 1:1 numerical comparison with an equivalent population of ground state molecules would have produced.

Concerning the shifting of the vibrational modes, their tendency towards lower frequencies is consistent with the spectroscopy of doped polymers and reflects the charge separated character of the PP.^{51,52} Chemically and electrochemically doped polymers exhibit strong Raman features on the red side of the neutral C=C stretch, commonly referred to as the quinoidal stretch band ($\sim 1400\text{-}1420\text{ cm}^{-1}$ for poly(3-alkylthiophenes)). The 15 cm^{-1} shift obtained here for the saturation model PTR represents an upper limit as other applied models (e.g. error function and exponential models) predict smaller frequency shifts of $7\text{-}10\text{ cm}^{-1}$. This magnitude is similar to what has been observed for polaron formation in other polymer-fullerene heterojunctions,²⁹ and it is not surprising that the extent of the spectral shift is fairly modest upon charge pair formation. The proximity of charges could be anticipated to induce an effectively lower charge density on adjacent polymer sites than is the case in isolated polarons, only modestly softening the C=C stretch frequency relative to the unexcited polymer. Furthermore, π -stacking interactions may be expected to partially distribute charge density between chains, giving rise to weaker shifts than those observed in amorphous or unordered polymer regions.

Additional experiments interrogated isolated polarons of RR-P3HT and the coupled PP state of regio-random (RRa)-P3HT NPs using FSRS with a 900 nm Raman pump pulse set to be resonant with those states. Figure 3.7 shows the ground state spectra of these two materials (green and dashed dark green) compared with corresponding PTR spectra obtained from a similar saturation model SVD analysis (red and dashed dark red). The intensities of the spectra of each material were scaled relative to the peak of C=C stretching mode from the corresponding PTR spectrum.

In the case of these two PTR spectra, the totally symmetric C=C stretching mode is significantly more intense than for the GSR spectra, predominantly because the comparison is being made between a resonant transient with a non-resonant ground state coherence. While only a fraction of photoexcitations will result in polaron or PP states for RR- and RRa-P3HT respectively, the increase in absorption cross-section provided by resonance, on the order of a few orders of magnitude, leads to reasonably higher Raman gain intensities than seen in their GSR spectra.

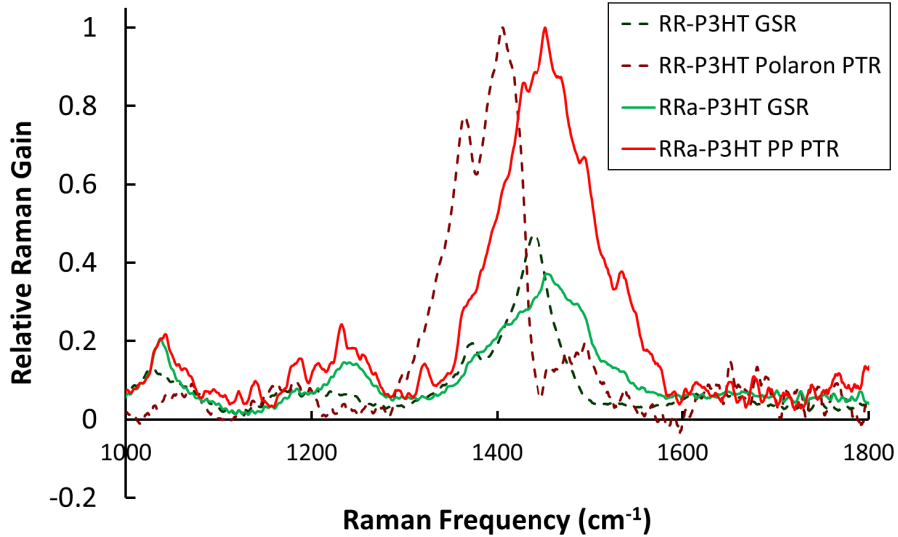


Figure 3.7: Extracted PTR Spectra of RR-P3HT Polaron and RRa-P3HT PP NPs: comparison of GSR spectra of RR- and RRa-P3HT NP's (solid light green and dashed dark green) using a Raman excitation wavelength of 900 nm to the PTR spectra of their resonant polaron and PP states (solid red and dashed dark red), respectively.

Interestingly, the two states exhibit substantially different amounts of spectral shifting, with red shifts for the RR-P3HT polaron and RRa-P3HT PP states of 34 and 1.5 cm^{-1} , respectively. Isolated polarons of RR-P3HT show a trend similar to but more intense than that seen for RR-P3HT's PP transients (Figure 3.5), with over twice as much of a red-shift to lower vibrational frequencies compared to the

ground state. This larger magnitude shift is likely the result of two factors. First, the more selective localization of these transients compared to PP states indicates that a greater degree of structural flexibility may be possible for an isolated polaron, as it does have to accommodate or couple to a second, adjacent polaron, and could provide leeway towards localizing along significantly more prolonged or well-ordered sites. Second, the now isolated positive charge on the polaron is likely to reduce the electron density within the thiophene π -conjugated network along its backbone, which will soften the bonding network and decrease the corresponding vibrational frequency.

As this latter shift lies well below the anticipated resolution of the measurement ($\approx 5\text{-}10\text{ cm}^{-1}$), it is safe to conclude that the frequency of the C=C stretching mode in RRa-P3HT shifts only negligibly upon charge separation. This corroborates previous findings that intermolecular steric hindrance produced by RRa-P3HT's randomly oriented hexyl side-chains imparts a great deal of intramolecular disorder, preventing prolonged π -interaction and localization of charge transfer states along extended segments of the polymer. Thus these unorganized charge transfer transients are not formed as efficiently and either do not strongly prefer or cannot reside on sites of a particular morphology over others. This would result in relatively little impact on the frequency of the synchronous "ring-breathing" C=C stretch as seen by Figure 3.7. These additional results highlight the ability of FSRS to selectively probe a particular transient and for advanced methodology to extract information concerning the structural nature, location, and photoinduced dynamics of these transients.

3.5 Conclusions

A combination of time- and pump-intensity-dependent Raman measurements was used to selectively probe the formation and vibrational spectroscopy of photo-generated transient polaron pairs in ordered regions of P3HT nanoparticle aggregates characterized by heterogeneous domains of intermolecular order. This work demonstrates the potential of time-resolved Raman as a morphologically selective probe for tracking ultrafast charge separation dynamics within polymer regions of conjugated materials, much as infrared absorption has been used successfully to interrogate the transient charge migration dynamics that occurs within domains of electron acceptors in bulk heterojunctions.²⁸ Measurements and subsequent analysis have exemplified the capabilities of ultrafast vibrational probes (FSRS) for examining and characterizing the morphological nature of charge-coupled PP states, providing vibrational markers to corroborate kinetic information derived from electronic transient absorption studies, and extracting pure vibrational spectra of these and related transient states within photoexcited conjugated materials.

3.6 Acknowledgments

As mentioned previously, I would like to acknowledge Julie Bitter and Miranda Gallagher as well as Dr. Michael McCaffery for their assistance in conducting DLS and TEM measurements on the P3HT nanoparticles studied here, respectively. I would also like to acknowledge Wenjian Yu and Jiawang Zhou for conducting comparable

solution phase measurements and initially setting up our FSRS experimental set-up which both facilitated the publication of this work.

References

1. Gunes, S., Neugebauer, H., and Sariciftci, N. S. *Chem. Rev.* **107**(4), 1324–1338 (2007).
2. Facchetti, A. *Chem. Mater.* **23**, 733–758 (2011).
3. Scharber, M. C., Mühlbacher, D., Koppe, M., Denk, P., Waldauf, C., Heeger, A. J., and Brabec, C. J. *Adv. Mater.* **18**(6), 789–794 (2006).
4. Yang, X. N., Loos, J., Veenstra, S. C., Verhees, W. J. H., Wienk, M. M., Kroon, J. M., Michels, M. A. J., and Janssen, R. A. J. *Nano Lett.* **5**(4), 579–583 (2005).
5. Gao, Y., Martin, T. P., Thomas, A. K., and Grey, J. K. *J. Phys. Chem. Lett.* **1**(1), 178–182 (2010).
6. Huang, Y., Kramer, E. J., Heeger, A. J., and Bazan, G. C. *Chem. Rev.* **114**(14), 7006–7043 (2014).
7. Schwartz, B. J. *Annu. Rev. Phys. Chem.* **54**(1), 141–172 (2003).
8. Scharsich, C., Lohwasser, R. H., Sommer, M., Asawapirom, U., Scherf, U., Thelakkat, M., Neher, D., and Köhler, A. *J. Polym. Sci. Part B Polym. Phys.* **50**(6), 442–453 (2012).
9. Kurokawa, N., Yoshikawa, H., Hirota, N., Hyodo, K., and Masuhara, H. *ChemPhysChem* **5**(10), 1609–1615 (2004).
10. Janssen, G., Aguirre, A., Goovaerts, E., Vanlaeke, P., Poortsmans, J., and Manca, J. *Eur Phys J Appl Phys* **37**, 287–290 (2007).
11. Ayzner, A. L., Wanger, D. D., Tassone, C. J., Tolbert, S. H., and Schwartz, B. J. *J. Phys. Chem. C* **112**(48), 18711–18716 (2008).
12. Guo, J., Ohkita, H., Benten, H., and Ito, S. *J. Am. Chem. Soc.* **131**(46), 16869–16880 (2009).
13. Ohkita, H., Kosaka, J., Guo, J., Benten, H., and Ito, S. *J. Photon. Energy* **1**(1), 011118–011118 – 12 (2011).
14. Cook, S., Furube, A., and Katoh, R. *Energy Environ. Sci.* **1**(2), 294–299 (2008).
15. Kurniawan, M., Salim, T., Tai, K. F., Sun, S., Sie, E. J., Wu, X., Yeow, E. K. L., Huan, C. H. A., Lam, Y. M., and Sum, T. C. *J. Phys. Chem. C* **116**(34), 18015–18022 (2012).

16. Banerji, N., Cowan, S., Vauthey, E., and Heeger, A. J. *J. Phys. Chem. C* **115**(19), 9726–9739 (2011).
17. Clarke, T. M. and Durrant, J. R. *Chem. Rev.* **110**(11), 6736–6767 (2010).
18. Chen, K., Barker, A. J., Reish, M. E., Gordon, K. C., and Hodgkiss, J. M. *J. Am. Chem. Soc.* **135**(49), 18502–18512 (2013).
19. Wells, N. P., Boudouris, B. W., Hillmyer, M. A., and Blank, D. A. *J. Phys. Chem. C* **111**(42), 15404–15414 (2007).
20. Wu, G., Li, Z., Zhang, X., and Lu, G. *J. Phys. Chem. Lett.* **5**(15), 2649–2656 (2014).
21. Piris, J., Dykstra, T. E., Bakulin, A. A., van Loosdrecht, P. H., Knulst, W., Trinh, M. T., Schins, J. M., and Siebbeles, L. D. *J. Phys. Chem. C* **113**(32), 14500–14506 (2009).
22. Herrmann, D., Niesar, S., Scharsich, C., Köhler, A., Stutzmann, M., and Riedle, E. *J. Am. Chem. Soc.* **133**(45), 18220–18233 (2011).
23. Martin, T. P., Wise, A. J., Busby, E., Gao, J., Roehling, J. D., Ford, M. J., Larsen, D. S., Moulé, A. J., and Grey, J. K. *J. Phys. Chem. B* **117**(16), 4478–4487 (2013).
24. Clifton, S. N., Huang, D. M., Massey, W. R., and Kee, T. W. *J. Phys. Chem. B* **117**(16), 4626–4633 (2013).
25. Scholes, G. D. *ACS Nano* **2**(3), 523–537 (2008).
26. Martini, I. B., Smith, A. D., and Schwartz, B. J. *Phys. Rev. B* **69**(3), 035204–035204 – 12 (2004).
27. Gao, B.-R., Wang, H.-Y., Wang, H., Yang, Z.-Y., Wang, L., Jiang, Y., Hao, Y.-W., Chen, Q.-D., and Sun, H.-B. *IEEE J. Quantum Electron.* **48**(3), 425–432 (2012).
28. Barbour, L. W., Hegadorn, M., and Asbury, J. B. *J. Am. Chem. Soc.* **129**(51), 15884–15894 (2007).
29. Provencher, F., Bérubé, N., Parker, A. W., Greetham, G. M., Towrie, M., Hellmann, C., Côté, M., Stingelin, N., Silva, C., and Hayes, S. C. *Nat Commun* **5**, 4288 (2014).
30. Niles, E. T., Roehling, J. D., Yamagata, H., Wise, A. J., Spano, F. C., Moulé, A. J., and Grey, J. K. *J. Phys. Chem. Lett.* **3**(2), 259–263 (2012).
31. Gao, Y. and Grey, J. K. *J. Am. Chem. Soc.* **131**(28), 9654–9662 (2009).

32. Lefrant, S., Baltog, I., de la Chapelle, M. L., Baibarac, M., Louarn, G., Journet, C., and Bernier, P. *Synth. Met.* **100**(1), 13–27 (1999). 13.
33. Tsoi, W. C., James, D. T., Kim, J. S., Nicholson, P. G., Murphy, C. E., Bradley, D. D. C., Nelson, J., and Kim, J.-S. *J. Am. Chem. Soc.* **133**(25), 9834–9843 (2011).
34. Hernandez, V., Castiglioni, C., Del Zoppo, M., and Zerbi, G. *Phys. Rev. B* **50**, 9815–9823 (1994).
35. Carach, C., Riisness, I., and Gordon, M. J. *Appl. Phys. Lett.* **101**(8), 083302–083302–5 (2012).
36. Miller, S., Fanchini, G., Lin, Y. Y., Li, C., Chen, C. W., Su, W. F., and Chhowalla, M. *J. Mater. Chem.* **18**(3), 306–312 (2008).
37. Lee, Y.-b., Lee, S. H., Kim, K., Lee, J. W., Han, K.-Y., Kim, J., and Joo, J. *J. Mater. Chem.* **22**(6), 2485–2490 (2012).
38. Lee, S. H., Lee, Y. B., Park, D. H., Kim, M. S., Cho, E. H., and Joo, J. *Sci Technol Adv Mater* **12**, 025002–025002 – 6 (2011).
39. Milani, A., Brambilla, L., Del Zoppo, M., and Zerbi, G. *J. Phys. Chem. B* **111**(6), 1271–1276 (2007).
40. Kukura, P., McCamant, D. W., and Mathies, R. A. *Annu. Rev. Phys. Chem.* **58**(1), 461–488 (2007).
41. McCamant, D. W., Kukura, P., Yoon, S., and Mathies, R. A. *Rev. Sci. Instrum.* **75**(11), 4971–4980 (2004).
42. Yu, W., Zhou, J., and Bragg, A. E. *J. Phys. Chem. Lett.* **3**(10), 1321–1328 (2012).
43. Yu, W., Donohoo-Vallett, P. J., Zhou, J., and Bragg, A. E. *J. Chem. Phys.* **141**(4), 044201–044201 – 13 (2014).
44. Shimizu, H., Yamada, M., Wada, R., and Okabe, M. *Polym. J* **40**(1), 33–36 (online November 13, 2007).
45. Brown, P. J., Thomas, D. S., Köhler, A., Wilson, J. S., Kim, J.-S., Ramsdale, C. M., Sirringhaus, H., and Friend, R. H. *Phys. Rev. B* **67**(6), 064203–064203 – 16 (2003).
46. Baghgar, M., Labastide, J. A., Bokel, F., Hayward, R. C., and Barnes, M. D. *J. Phys. Chem. C* **118**(4), 2229–2235 (2014).
47. Spano, F. C. *Acc. Chem. Res.* **43**(3), 429–439 (2010).
48. Louarn, G., Trznadel, M., Buisson, J. P., Laska, J., Pron, A., Lapkowski, M., and Lefrant, S. *J. Phys. Chem.* **100**(30), 12532–12539 (1996).

- 49. Hendler, R. W. and Shrager, R. I. *Journal of Biochemical and Biophysical Methods* **28**(1), 1–33 (1994).
- 50. Magnanelli, T. J. and Bragg, A. E. *J. Phys. Chem. Lett.* **6**(3), 438–445 (2015).
- 51. Gao, J., Roehling, J. D., Li, Y., Guo, H., Moulé, A. J., and Grey, J. K. *J. Mater. Chem. C* **1**(36), 5638–5646 (2013).
- 52. Shoute, L. C. T., Pekas, N., Wu, Y., and McCreery, R. L. *Appl. Phys. A* **102**(4), 841–850 (2011).

Chapter 4

Exciton Dynamics in Thiophene-Methanoannulene Polymers and their Aggregates

4.1 Abstract

Transient absorption (TA) and broadband polarization anisotropy (BPA) were employed to interrogate the photoinduced behaviors of several novel thiophene- 1,6-methano (10)annulene- thiophene polymers (PTMT)s. The structure of these polymers hinders large-scale intermolecular π -interactions while not compromising intrachain π -electron delocalization. The goal of this work was to investigate how the highly non-planar structure of these materials impacts the photoinduced dynamics of polymer excitation both in isolation and as nano-aggregated particles (emulating films). Contrasting TA responses of aggregates with those from unassembled polymer in solution reveals that PTMT transients are only weakly impacted by intermolecular interactions. Polymers with different substituents were compared to determine how their photophysics are impacted by perturbations to local intramolecular structure. BPA measurements indicated greater excited-state localization along

the polymer backbone when alkyl substituents are positioned to disrupt the planarity of bio-thiophene moieties, and that the persistent “polarization memory” of triplet states varies with substitution pattern along the polymer backbone.

4.2 Introduction

Thiophene-methanoannulene-thiophene polymers (PTMT) are non-planar conjugated materials designed to frustrate intermolecular π -interaction (i.e. maintain an amorphous morphology) without compromising the ability for electronically excited transient states to delocalize intramolecularly along the polymer strand. Hexyl chain substituents have been introduced at different positions along the thiophene segments of the polymer backbone to improve solubility in organic solvents but can also be used as a degree of freedom in tuning their photophysical properties and electrical conductivity. These substituents have been shown to hypsochromically shift the visible feature of both the ground state electronic absorbances (UV-Vis) by 2000 cm^{-1} and the accompanying steady state photoluminescence spectra by 1500 cm^{-1} relative to the unsubstituted polymer.¹ The direct effects on these steady state characteristics indicate that deconfiguring the hexyl chains to form different stereoisomers can significantly alter intramolecular ordering through the steric repulsion of neighboring molecular moieties along a given strand. The torsional strain induced by these substituents can also have an impact on intermolecular stacking within an aggregated environment, leading to disruptions of effective conjugation length and further inhibiting the formation of long range π -network domains. Derivatives of PTMT polymers

utilized as part of organic field effect transistors (OFETs) produced semiconducting layers in which hole mobilities varied with substituent, showing a 16% decrease for the hexyl substituted polymer compared to the unsubstituted polymer.¹ Semiconductor conductivity is critical to device performance and is directly dependent on the underlying microstructures formed by each polymer. Since the nature of the corresponding excitonic states also depends on the polymer’s structure, developing a better understanding of how their delocalization depends on local structure, and the photo-physical impacts of tailoring the polymers via incorporation of substituents would be instrumental in understanding how to improve their material conductivity.^{1,2}

Figure 4.1 displays the structures of the different PTMT polymers explored herein. The two primary candidates for establishing the photophysical effects induced by systematically positioned hexyl substituents are (a) tail-in (TI)- and (b) tail-out (TO)-PTMT. Tail-in and tail-out designate whether the substituent is directed towards or away from the methanoannulene moiety, which occurs when the hexyl groups are located at the 2 and 2” or 3 and 3” positions of the thiophene rings in each repeating unit, respectively. It is anticipated that the TI isomer will not impact conjugation across the bithiophene moieties substantially when compared with the unsubstituted ”no-tail” PTMT (c), and that the primary intramolecular effect should be to produce kinks between thiophenes and adjacent methanoannulenes to further disrupt long range conjugation. TO, on the other hand, should disrupt conjugation between each adjacent pair of thiophenes due to “head-to-head” steric interactions and result in blue-shifted absorption relative to the TI and NT polymer. This would reflect shorter effective conjugation lengths and hence more compact local-

ization of excited states along the polymer chain. Figure 4.2 shows three dimensional structures of oligomeric segments (using ethyl groups to emulate hexyl side chains) optimized using *ab-initio* density functional theory (DFT) calculations. These support the previous descriptions and show that the thiophene-methanoannulene bond angle increases by 14° in TI (4.2b) relative to NT (4.2a) and the thiophene-thiophene bond angle increases by 66° in TO (4.2c) relative to NT (4.2a). These PTMT's can be contrasted with an analogous polymer containing terthiophene segments, theoretically permitting more delocalized transients and greater variability/heterogeneity in ordering amongst individual segments along the backbone, designated as PTMTT (d).

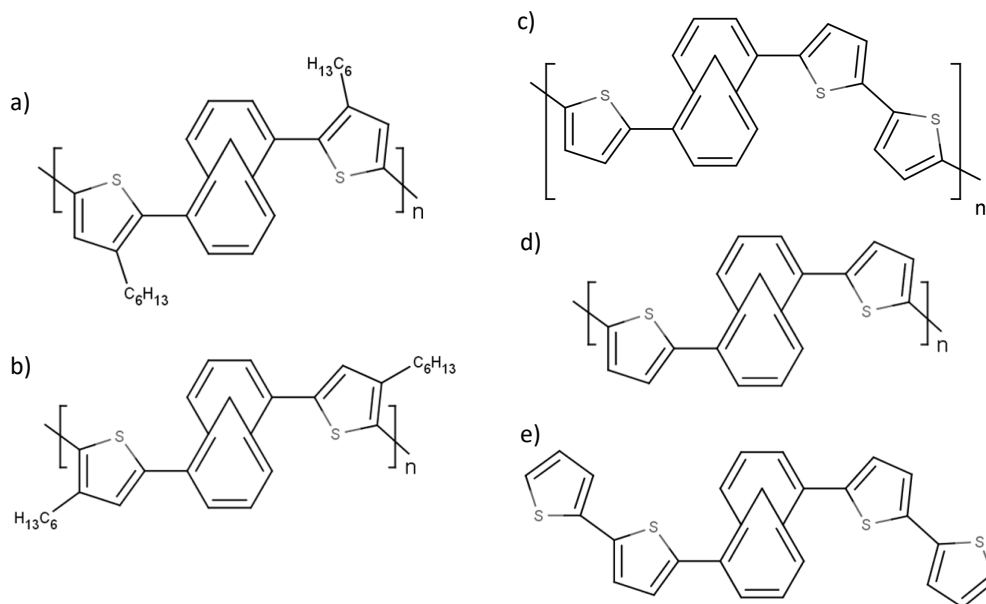


Figure 4.1: Thiophene-Methanoannulene Polymer and Oligomer Structures: Structures of (un)substituted PTMTs studied herein, including (a) TI, (b) TO, (c) NT, (d) PTMTT, and (e) TTMTT (oligomer)

Polymer nanoaggregates provide the primary means to probe intermolecular

interactions between adjacent polymer strands. By comparing the transient signatures and resulting kinetics following photoexcitation for an isolated strand of polymer (susceptible only to intramolecular ordering effects) and these aggregates, the differences can be used to illustrate differences in how transients states are localized and whether intermolecular interactions lead to energy/charge transfer, additional pathways for relaxation, or new transient states altogether. The final molecule to aid in these comparisons is the oligomeric segment, consisting of two bi-thiophene and a central methanoannulene core, TTMTT (e). In addition to the anticipated simplified spectra progression for drawing information about isolated excitations, the oligomer likely also entails additional structural patterns upon aggregation that can help to isolate and identify what is occurring within PTMT aggregates.

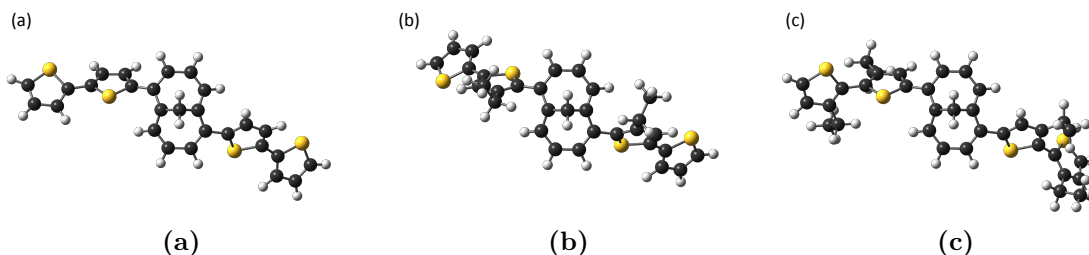


Figure 4.2: DFT Oligomer Estimate 3D Structures: Estimated *ab-initio*, DFT, structures used to estimate the bond angles and intramolecular order of (a) NT, (b) TI, and (c) TO

Finally, broadband polarized transient absorption, has also been used to track the dynamics of polymer excitations to interrogate how intra- and intermolecular structure impact their photoresponses as described in Section 1.2.3. Briefly, anisotropy in transition polarizations, $r(t, \lambda)$, provides a means to track the change in each transition dipole as a function of time delay after excitation and can be used to determine the timescales and extent of molecular rotation, energy or charge migration in a com-

plex molecule (e.g. polymer) or the movement or dipole re-orientation of a specific chromophore over time. The broadband version of this measurement (BPA) allows for time-dependent anisotropy of multiple transients to be compared simultaneously to affirm which states are intrinsically linked to one another and which incur state-specific motions over time.

4.3 Experimental Methods

Solution-phase TO, TI, and TTMTT were prepared by dissolving weighed solid samples of each polymer in chlorobenzene (ArCl) to concentrations of 0.1, 0.1, and 0.2 mg/mL, respectively. NT was similarly prepared as a 0.2 mg/mL solution in chloroform (CHCl_3) and PTMTT as an 0.1 mg/mL solution in benzene. TO, TI, and TTMTT nanoaggregates were prepared using the standard reprecipitation method (Section 2.1), involving the addition of three to four 500 μm aliquots of a 0.1 mg/mL solution of TO, TI, or TTMTT in tetrahydrofuran (THF) into 5 mL of rapidly stirred H_2O . The added THF was driven off after each addition using compressed air. Only PTMTT solutions showed substantial evidence of instability as a function of storage time; the polymer would gradually coalesce into macroscopic particles and precipitate, with benzene being the best solvent available to keep the polymer solvated for much longer than the timescales necessary to conduct spectroscopic measurements.

Transient absorption (TA) and broadband polarization anisotropy (BPA) measurements were conducted on the five molecules highlighted above, using 400 and 480 nm excitation pulses and experimental set-ups described previously in Section 2.2.

TO- and TI-PTMTT exhibited minimal degradation in response to laser exposure over the course of a single measurement. PTMTT was a particularly difficult sample to analyze as larger aggregates gradually accumulated in response to laser exposure or prolonged storage in a cuvette, resulting in significant light scattering that limited the quality of the probe. However, this aggregation did not significantly impact the observed sample concentration or transient signal intensities over the course of corresponding measurements.

4.4 Results and Discussion

4.4.1 UV-Vis and Characterization

Steady state electronic absorbance (UV-Vis) spectra collected for each polymer are shown in Figure 4.3 and reflect differences in their conformational order through the energy of the lowest transitions accessible from their ground states. Figure 4.3a shows spectra for each individually isolated in solution, in which the primary absorbance band peaks between 400 and 475 nm, with λ_{Peak} : TO > TTMTT > TI > NT > PTMTT. TO and PTMTT each exhibit shoulder features centered at 575 nm that are assumed to be anomalies due to the cuvette, while NT and PTMTT contain broad scattering tails due to undissolved polymer dispersed in each solution. Figure 4.3b compares the steady state absorption spectra of TO, TI, and TTMTT solution samples with their corresponding nanoaggregates. The reprecipitated particles force the polymers/oligomer into an aggregated environment, but the absence

of significant spectral shifting provides preliminary indication that there is little intermolecular ordering between adjacent strands of polymer/oligomers, unlike what is observed for polythiophenes as seen in Figure 3.1b.

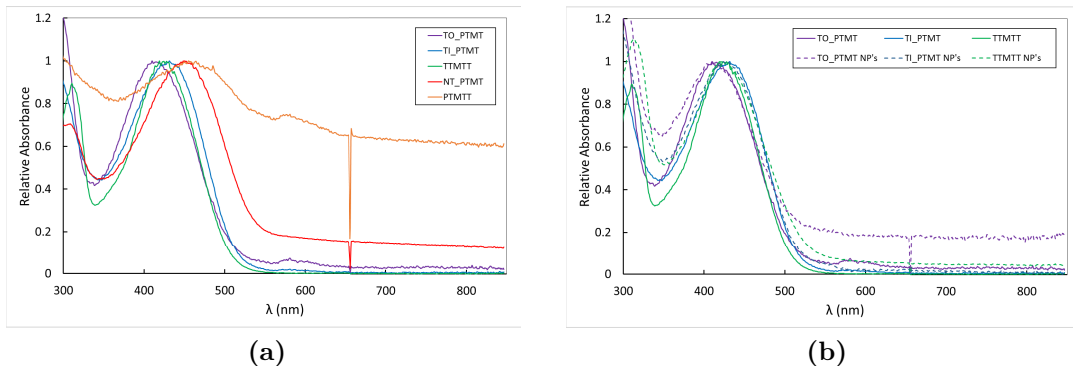


Figure 4.3: Steady State Absorption Spectra of PTMTs: (a) solution phase UV-Vis spectra for various substituted PTMT polymers and TTMTT and (b) comparison of UV-Vis absorption spectra for TO, TI, and TTMTT in solution phase to their respective nanoaggregates

4.4.2 Transient Absorption: Impacts of Substituents and Comparisons to Oligomer and PTMTT

Transient absorption spectra collected with 480 nm excitation of each of the various polymers are presented in Figure 4.4. Here, the unsubstituted, “no-tail” NT-PTMT can serve as a frame of reference for understanding the impact of solubilizing substituents on excited state properties and dynamics. Figure 4.4a shows TA spectra of solution phase NT excited at 480 nm. The spectra exhibit three features that are present immediately upon photoexcitation; these include a bleach of the ground state absorption (GSB) centered at 470 nm, a stimulated emission (SE) ascribed to the S_1 singlet state at 590 nm, and a broad transient absorption (TA), also due to S_1 , in the near infrared (NIR) at 1075 nm. Integrated cuts from the GSB and S_1

TA regions of the spectra exhibit bi-exponential decay kinetics with lifetimes of 52, 902 and 30, 230 ps respectively. At later time delays, a broad absorbance appears at 660 nm, obscuring the decay kinetics of the SE band. Based on comparisons to the transient spectra of other thiophene polymers and oligomers in solution^{3,4} this feature is ascribed to the lowest triplet state, T_1 , populated via intersystem crossing (ISC) from S_1 . The SE decays concomitant with the growth of the triplet spectra with bi-exponential lifetimes of 4.2 and 47 ps. These fast timescales, coupled with the decay kinetics of the singlet, indicate a relatively rapid ISC rate that competes with other radiative and nonradiative relaxation pathways.

The position of solubilizing hexyl substituents markedly impacts local conformation in the polymer and is anticipated to affect the extent of excited-state delocalization, transition energies of transient spectral features, and dynamics of transient states. In line with these expectations, 480 nm excitation of TO-PTMT (Figure 4.4b) exhibits transient spectra with dramatic hypsochromic (blue) shifts of both the S_1 and T_1 absorbances relative to the NT polymer by 1363 and 2025 cm^{-1} , respectively. The spectral dynamics of TI, presented in Figure 4.4c, only show subtle differences relative to that of NT. Similar to TO, the S_1 absorbance and SE of TI are blue-shifted, though only by 602 and 405 cm^{-1} , respectively. Interestingly, the T_1 absorbance of TI exhibits a slight bathochromic (red) shift of 180 cm^{-1} relative to NT. These spectral shifting patterns indicate that incorporating the hexyl chains into the polymer such that they face towards the methanoannulene (TI) has less impact on the spectroscopic characteristics of transient excited states than directing them away from the methanoannulene (TO). Despite these significant spectral shifts, the decay kinetics

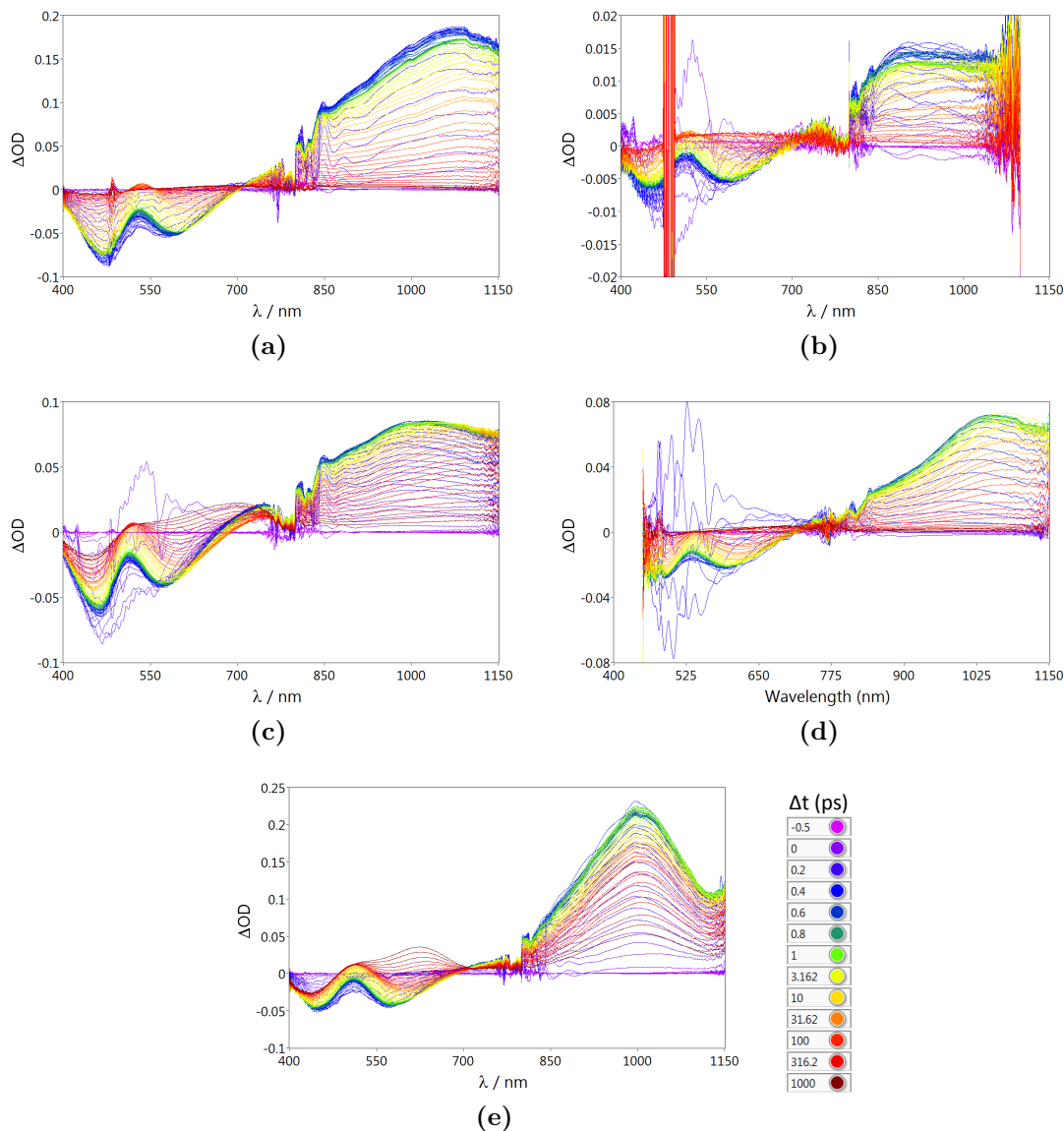


Figure 4.4: 480 nm Excitation Transient Absorption of PTMTs: (a) NT-, (b) TO-, and (c) TI-PTMT, and (d) PTMTT polymers and (e) TTMTT oligomer

associated with the S_1 absorbance bands of TO and TI are quite similar to those of NT. A significantly larger fraction of GSB signal in TI remains by a delay of one ns (53 vs. 16 %), though the fraction decaying on a faster timescale does so significantly more rapidly, with relaxation lifetimes of 862 and 11 ps, respectively.

In order to explore the impact of structure on excited-state localization, the photoresponses of these polymers can be further compared against spectral dynam-

ics associated with the oligomer TTMTT. Figure 4.4e displays the TA spectrum of TTMTT, and although it exhibits the same qualitative features and dynamics as the PTMTs, the transient features are discernibly sharper than the polymers but with kinetics comparable to those seen for TI. This contrasts markedly from what is observed for oligo- vs. polythiophenes.⁴⁻⁷ The T_1 absorption band of TTMTT lies between that of NT and TO and is generated with significantly greater intensity than the PTMTs for this excitation energy, either due to a higher absorption cross-section or more efficient ISC. TA spectra of PTMTT are also included as Figure 4.4d. With extended terthiophene moieties, trends in the electronic absorption align fairly well with anticipated differences in conjugation: the GSB and T_1 absorption bands are significantly red-shifted by 909 and 363 cm^{-1} , respectively, which corresponds well with the bleaching of a more conjugated ground state population and triplets characterized by increased delocalization across the thiophene moieties. The GSB recovery timescales are also more rapid (12 and 153 ps), despite similar dynamics of the S_1 absorption band. Interestingly, there is no discernible shifting of either the SE or S_1 absorption bands relative to NT, suggesting that these transient state absorptions are associated with either very localized interactions dispersed over two or fewer conjugated thiophenes, or that the involved states only span the immediate vicinity about a methanoannulene. While the methanoannulene is conjugated, the deviation that it induces away from planarity may disrupt broadly delocalized thiophene interaction and conjugation, inhibiting the ability for a third thiophene to participate effectively in localizing a singlet transient.

4.4.3 Photodynamic Effects of Increasing Pump Frequency

Heterogeneous broadening of the polymer absorption spectrum can arise from conformational disorder along a strand of polymer within an amorphous environment. Energy-dependent selectivity for exciting conformations with different effective conjugation lengths is a consequence of this heterogeneity: lower pump energies preferentially excite regions of the polymer with greater conformational order (i.e. greater effective conjugation lengths), whereas higher pump energies can access more conformationally disordered regions of the polymer (i.e. shorter effective conjugation lengths). Experimentally this could be recognized from excitation-dependent variations in transient spectral features. Complete tables documenting the shift of each polymer/oligomer relative to NT, between solution and aggregates, and excited at 400 nm relative to 480 nm are included as Figure 8.1a and 8.1b in Appendix 8.2. Figure 4.5 presents TA spectra for the same samples excited using a 400 nm excitation pulse. The magnitude to which the GSB blue-shifts when excited at 400 nm compared to 480 nm varies only slightly with substituent with shifts of 990, 845, 850, and 1140 cm^{-1} for NT, TI, TO, PTMTT respectively. The GSB of TTMTT exhibits significantly less shifting than the PTMT (206 cm^{-1}), which is expected because the molecule is definitively smaller than any of the polymers, and small energetic differences exist between various conformer structures. This also yields little potential for intramolecular energy transfer or excitation of specific spectroscopic subpopulations independently of one another. The shifts of the singlet and triplet absorption bands vary quite markedly. In general, TO exhibits the greatest shifts, followed by NT

and TI with TTMTT shifting only negligibly. PTMTT is an outlier in this case as the T_1 band shifts quite substantially (1611 cm^{-1}) while the S_1 absorption does not (95 cm^{-1}). Higher excitation energy also slightly increases the relative amount of triplet formation in PTMTT, TO, and NT but does not substantially impact triplet signals of TI or TTMTT.

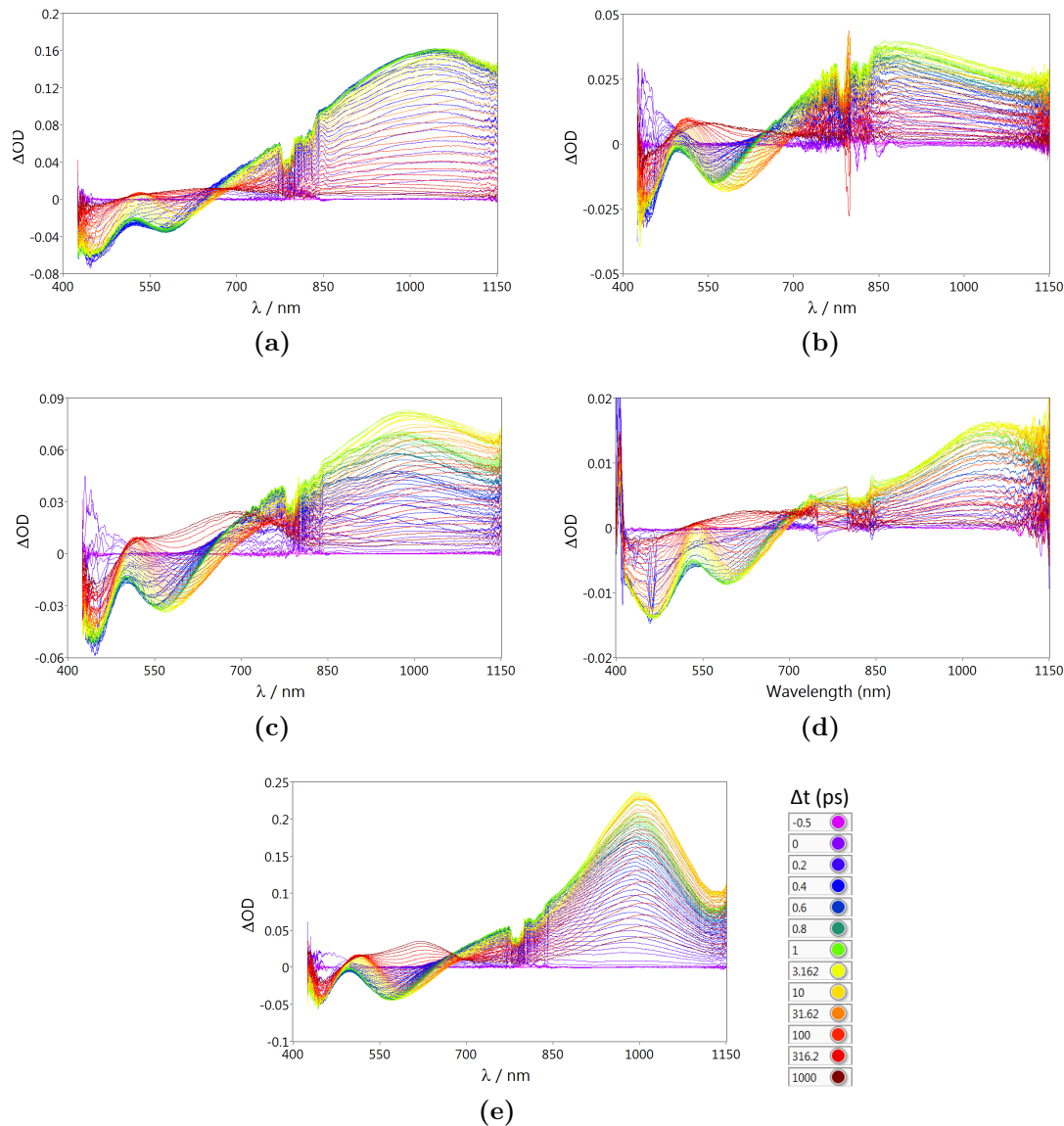


Figure 4.5: 400 nm Excitation Transient Absorption of PTMTs: (a) NT-, (b) TO-, and (c) TI-PTMT, and (d) PTMTT polymers and (e) TTMTT oligomer

TTMTT contains the easiest triplet absorbance band to isolate, and kinetic

fits of its growth rate indicate that the ISC rate increases for higher energy excitation as the triplet absorbance grows in on a scale of 1270 and 300 ps at 480 and 400 nm respectively. Overall, the heterogeneous nature of the polymer strands in solution leads to a clear distribution of chromophores characterized by variation in conformational order that can be selectively photo-excited; furthermore, this distribution appears to be only moderately affected by inclusion of solubilizing hexyl substituents. The SE bands of each material at the peak intensity of the feature shifts by $<400\text{ cm}^{-1}$ relative to those measured at lower-energy excitation.

Unlike low-energy excitation (480 nm), excitation at higher energies results in an induction of the S_1 absorption and SE bands over the first 200 fs for NT and each of the other materials. While this could be a signature of intramolecular energy migration and localization along the polymer backbone, the prevalence of the trend in TTMTT (without extended intramolecular domains) indicates that the transient signals gradually grow in over time following vibrational relaxation or other conformational dynamics. Decay traces of the GSB and S_1 absorption in NT reveal slightly more prolonged relaxation for higher energy excitation. In the case of the latter, the bi-exponential decay lifetimes increase by about 15-20% from 30 and 230 ps (480 nm) to 35 and 284 ps (400 nm), respectively.

An additional comparison can be made by examining how the SE band of each polymer and TTMTT shift as a function of time after excitation. This shift is particularly sensitive to excitation wavelength in showing substantial shifting over time and providing a better handle on conformational dynamics than the broad S_1 or cutoff GSB features. Figure 4.6 plots traces of the peak of each SE feature over time;

each peak red-shifts over the span of a few to a couple hundred ps depending on the substituents and excitation wavelength. Consistently, lower energy excitation results in an energetically lower lying stimulated emission band, which corresponds to only more conformationally ordered sites being populated at lower excitation energies (and hence the emission from states lying lower in energy). The magnitude and timescale of the SE red-shift can be associated with the degree/extent and corresponding kinetics, respectively, of excited state vibrational relaxation and localization onto more ordered molecular conformers.

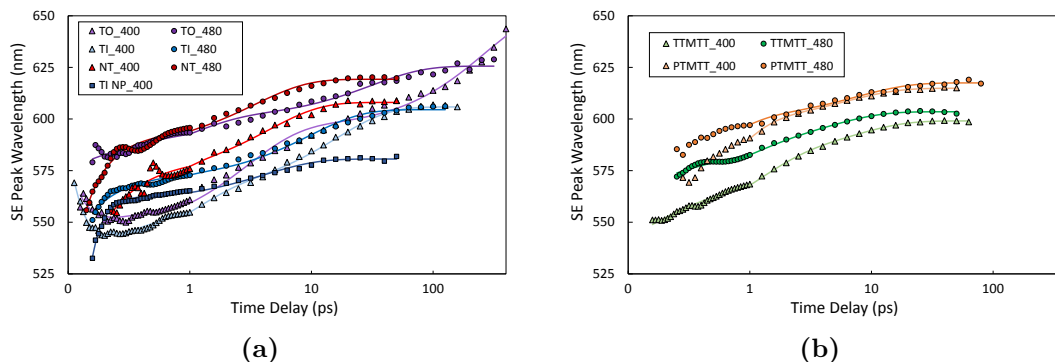


Figure 4.6: PTMT Stimulated Emission Peak λ Traces: (a) NT, TO, and TI PTMTs and (b) PTMTT and TTMTT with substituents and pump wavelength indicated by the keys

Table 4.1 lists the initially recorded SE emission wavelength (omitting initial sub-ps shifts) and wavelength shift by the time of the latest traceable delay for each material and both excitation wavelengths. Amongst the PTMTs, TO excited at 400 nm shows the largest shift over time, while at 480 nm shows a significantly redder band than either TI or NT. This indicates that TO exhibits more heterogeneity and the ability to localize higher energy excitations onto sites with greater conformational disparity (more ordered by comparison to sites of initial excitation) than TI or NT

over time. This comparison also further validates the similarity between TI and NT given by their similar SE shift dynamics. PTMTT exhibits both redder bands and smaller shifts than the PTMTs which is explainable considering their more prolonged conjugation (terthiophene vs. bithiophene), and the conformational order that likely arises from that. TI nanoparticles (NPs), shift by a similar amount but at slightly bluer wavelengths than in solution phase, perhaps a sign of disrupted ordering in response to aggregation and intermolecular steric hindrance from adjacent strands.

PTMT Label	400 nm Initial SE λ	400 nm λ Shift	480 nm Initial SE λ	480 nm λ Shift
<i>NT</i>	555	53	556	63
<i>TO</i>	551	95	579	46
<i>TI</i>	544	62	551	53
<i>TI NPs</i>	532	49	—	—
<i>PTMTT</i>	572	43	585	32
<i>TTMTT</i>	551	48	564	31

Table 4.1: PTMT Stimulated Emission Peak Initial λ and Shift

4.4.4 Photophysical Response to Aggregation

The UV-Vis spectra of TO and TI show only slight, near negligible hypsochromic shifts in response to aggregation (Figure 4.3b), indicating only very limited interchain coupling and tendency towards H-aggregation within the nanoaggregates. TTMTT shows little to no shift, though the predominant feature in the visible broadens significantly. Figure 4.7 presents transient absorption spectra collected for suspensions of TI, TO, and TTMTT nanoparticles. Exciting the TI nanoparticle suspension at an actinic pump wavelength of 480 nm produces a spectrum with very similar features observed in solution-phase measurements, but with a lower resultant triplet signal as shown in Figure 4.7a. Additionally, the relaxation kinetics proceed

on timescales that are nearly an order of magnitude faster with the S_1 absorption decaying with bi-exponential lifetimes of 3 and 85 ps compared to 24 and 407 ps for the solution phase. Furthermore, excitation of TI aggregates at both 400 and 480 nm (Figures 4.7a and 4.7b) produces transient absorption dynamics that strongly resemble those measured for TI in solution excited at 480 nm (Figure 4.4c). Only a minimal signal induction of the NP singlet signal when excited at 400 nm (<50 fs), and the positions of the GSB and SE bands are closer to those measured following 480 nm solution phase excitation. Comparisons of high and low fluence measurements on the particles suggest that the observed dynamics do not change appreciably by increasing the fluence and that the transients arise due to single excitation mechanisms. Despite the difference in excitation wavelength dependence for TI aggregates, TA signatures of TO nanoparticles (Figures 4.7c and 4.7d) do not deviate spectrally from their corresponding solution phase measurements. TO S_1 decay lifetimes are significantly faster in aggregates than in solution with bi-exponential decay lifetimes decreasing from 18/292 and 118/382 ps to 3/80 and 4/181 ps for 400 and 480 nm excitation, respectively.

Excitation of TTMTT nanoparticles at 480 nm (Figure 4.7e) also produces spectra that are qualitatively similar to those measured for TTMTT in solution, but with significantly faster relaxation dynamics and each band is red-shifted by 600-800 cm^{-1} , except for the S_1 absorbance which only shifts by 150 cm^{-1} . Both 480 and 400 nm excitation (Figure 4.7f) yield dramatically increased rates of triplet formation, with associated ISC lifetimes decreasing by a couple orders of magnitude from solution phase timescales, specifically from 1270 and 300 to 2.8 and 11 ps for 480

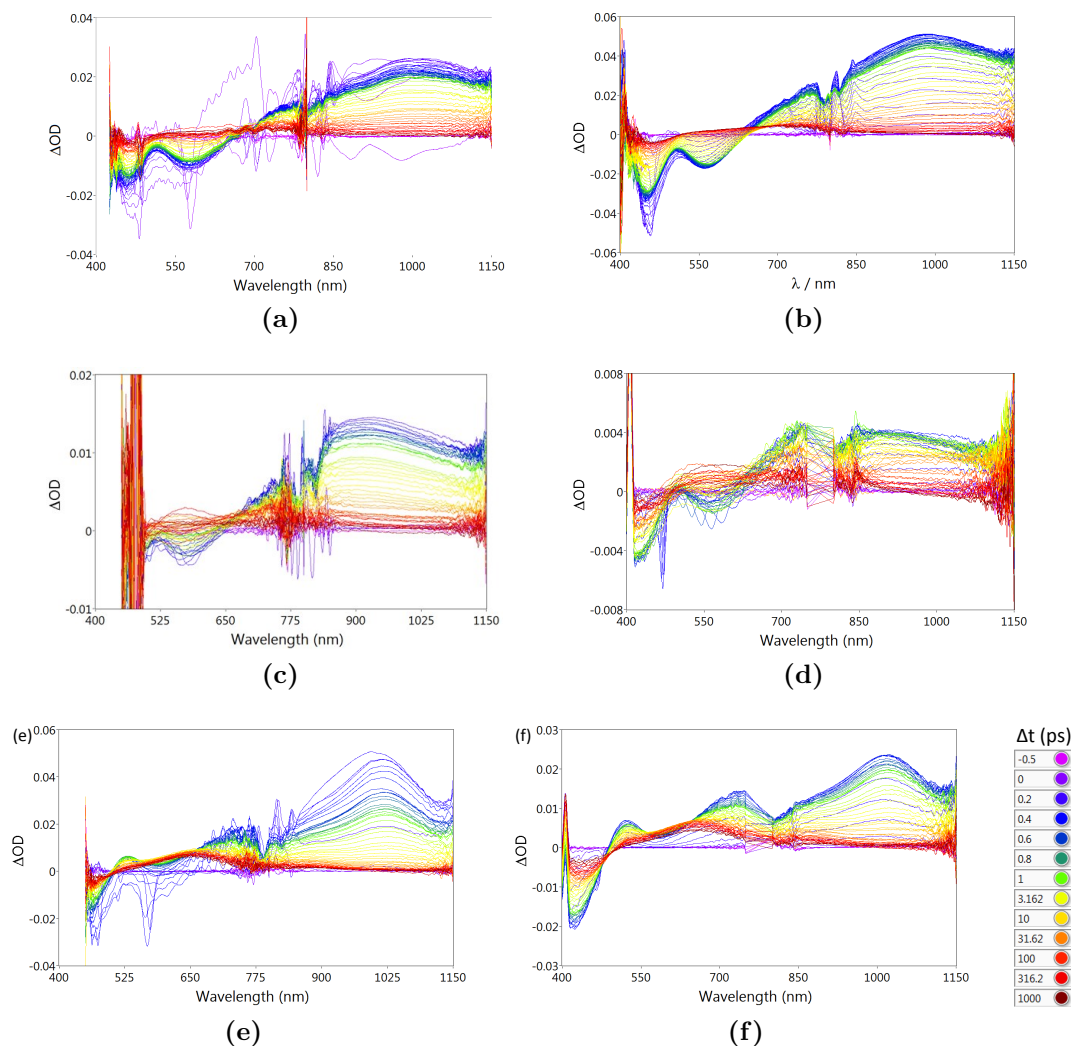


Figure 4.7: 480 and 400 nm Transient Absorption of (a, b) TI-PTMT, (c, d) TO-PTMT, and (e, f) TTMTT, respectively

and 400 nm excitation respectively. Higher energy (400 nm) excitation also yields an additional absorptive feature centered at 750 nm that decays concomitantly with the S_1 absorbance. The relaxation of this band is obscured by the presence of the T_1 absorbance, but does exhibit decay timescales that are comparable to those of the S_1 absorbance band (0.56, 17, and 1800 for the 750 nm band vs. 1.6, 16, and 750 ps for the S_1 band). This feature may be ascribable to a coupled polaron state seen previously in regio-regular poly-3-hexylthiophene (RR-P3HT) nanoaggregates

(Figure 3.2) arising from the ability of bithiophene units to π -stack vertically with methanoannulene groups directed outward. This arrangement is unobtainable for PTMT polymers due to the proximity of bulky methanoannulenes on either end of each bithiophene moiety. This steric hindrance severely restricts or prevents, ordered intermolecular coupling and coupled exciton solvation (as seen in other thiophene containing polymers) from occurring with PTMTs. The significant reduction in transient lifetimes of TI and TO-PTMT aggregates indicates that intermolecular interactions facilitate relaxation of the involved transients. However, the similarities seen within their transient absorptive features suggest that similar molecular conformations and no additional types of transients are generated via aggregation of the PTMT polymers.

4.4.5 Polarization Anisotropy: Substituent Effects and Insights from Aggregation and the Oligomer

Figure 4.8 presents contour plots of the broadband polarization anisotropy collected via 400 and 480 nm excitation of TTMTT. Figure 4.8a illustrates the BPA spectrum of TTMTT photoexcited at 480 nm in solution and provides an excellent reference system for testing BPA methodology. Here, no energy transfer is expected and the dominant relaxation of the polarization anisotropy should arise from molecular structural/conformational evolution and rotational diffusion in solution over time. The overlapping GSB, SE and T_1 bands obscure one another, rendering quantitative assessment of the bands difficult, except the T_1 absorption at very late times. By

contrast, the isolatable NIR absorption provides a more accurate estimate and indicate a very high degree of polarization anisotropy with $r_0(t, \lambda) = 0.4$. This anisotropy decays to an offset of 0.13 over a 239 ps lifetime. Though the amplified model suggests that 0.13 should be a constant offset, this is likely a reflection that molecular rotation may be slow enough to extend into the ns-regime. Excitation at 400 nm (Figure 4.8b) yields a reasonably lower initial anisotropy, $r(t, \lambda) = 0.25$, which decays towards zero on a similar timescale 226 ps. One possible explanation of this lower polarization anisotropy would be that 400 nm is resonant with a higher lying transition whose dipole is not entirely parallel with the S_0 to S_1 transition dipole which seems unlikely given the shape of the UV-Vis progression. It is also possible that a sizable degree of vibrational relaxation or conformational motion occurs on an ultrafast timescale upon higher energy excitation.

The polarization anisotropy of the same S_1 NIR absorption in TTMTT NPs (Figure 4.8c) is also initially lower than that seen for solution-phase with $r_0(t, \lambda) = 0.307$, though the most noticeable difference is that it relaxes towards zero nearly an order of magnitude faster, with bi-exponential decay lifetimes of 1.6 and 39 ps. This cannot be due to molecular rotation as the positions within large aggregates are relatively fixed. Rotation of a chromophore in response to photoexcitation is possible, but energy transfer through non-parallel intermolecular orbitals is more likely. Integrated decay traces are presented in conjunction with PTMT anisotropy data considered below as part of Figure 4.9a.

These same comparisons can be made for each PTMT, though the individual contour spectra are omitted here and included as Figure 8.3 in Appendix 8.2 for

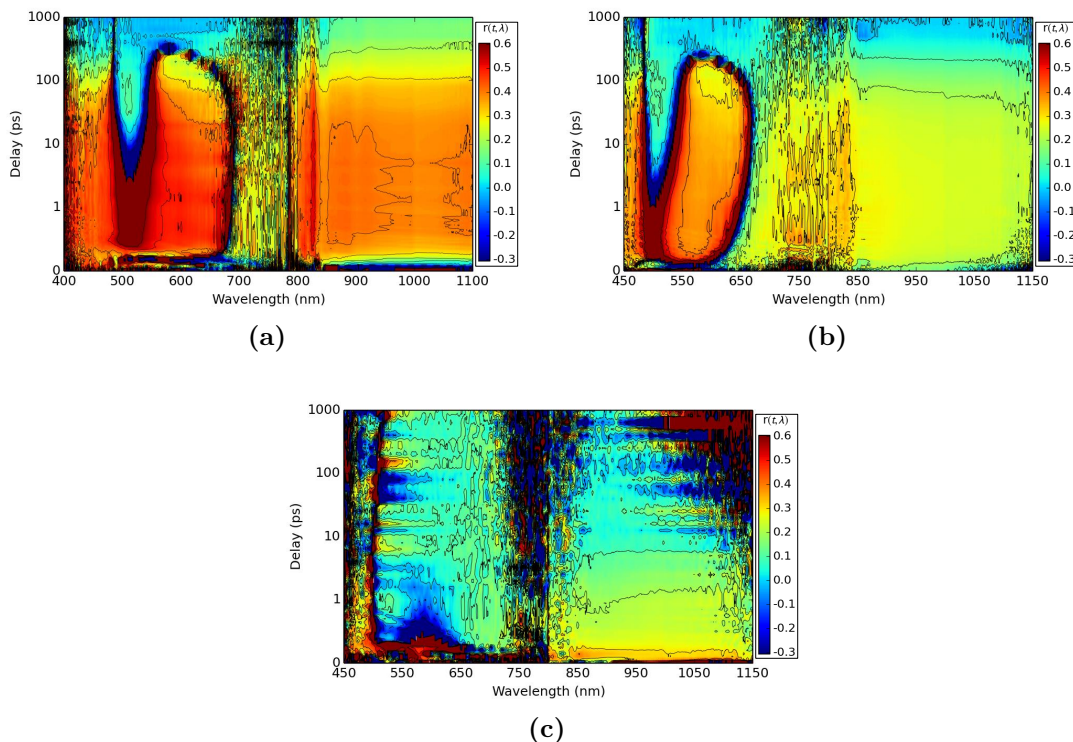


Figure 4.8: Polarization Anisotropy Spectra of TTMTT: TTMTT BPA contour plots for (a) 480 and (b) 400 nm excitation of the solution phase and (c) 480 nm excitation of aggregates

brevity. Instead, decay traces of the anisotropy measured for integrated regions of the S_1 NIR absorption are included as eluded to previously as Figure 4.9. NT and TI (red and blue traces respectively in Figure 4.9b) show similar tendencies to TTMTT, with a higher initial polarization anisotropy for 480 nm excitation (0.24 and 0.22, respectively) than for 400 nm excitation (0.17 and 0.18). These results, as a whole, coincide with the anticipation that lower frequencies should be limited to exciting lower energy, more ordered conformers that migrate less readily than regions excited by higher-energy excitation. Thus, the alignment of the measured transition dipoles with the excitation dipole, such that every feature encodes an $r(t, \lambda) > 0$, results in every feature exhibiting a lower $r(t, \lambda)$ when pumped at 400 than when pumped

at 480 nm. TO (purple, Figure 4.9b) exhibits a substantial difference between 480 and 400 nm excitation as well, with an initial $r_0(t, \lambda)$ of 0.33 and 0.19 respectively. Interestingly, the 480 nm anisotropy stands out as a portion of it decays with a lifetime of ≈ 250 fs to a lower $r(t, \lambda)$ than seen for 400 nm excitation by 1 ps.

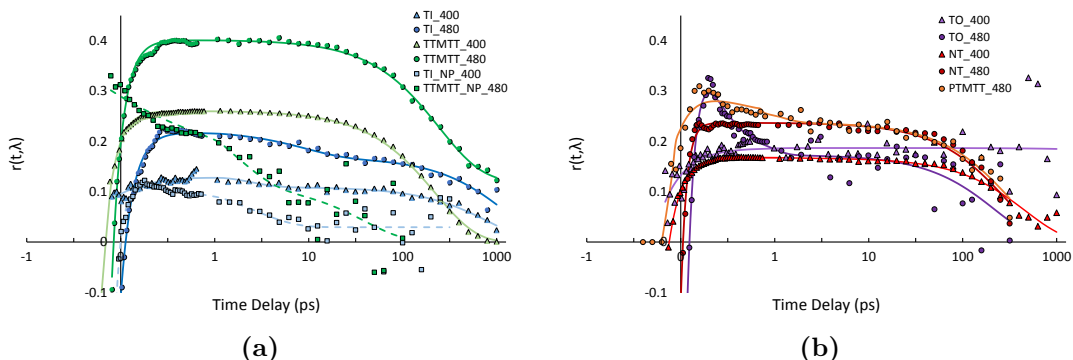


Figure 4.9: S_1 Polarization Anisotropy Decay Traces: (a) solution phase and NP TTMTT and TI, and (b) solution phase TO-PTMT, NT-PTMT, and PTMTT with substituents and pump wavelengths indicated by the keys

The anisotropy decay kinetics do not change substantially as the lifetime of primary decay component for TI and NT only shifts from 469 and 830 to 283 and 1230 ps for 480 and 400, respectively. Polarization anisotropy seen in TO excited at 400 nm persists for significantly longer than when excited at 480 nm, (constant on this timescale compared to a decay lifetime 220 ps). These relatively long anisotropy decay lifetimes cannot be ascribed to molecular rotation as that would occur much more slowly for a prolonged polymeric material than the 230 ps timescale seen in TTMTT. A component of these longer timescale decreases in anisotropy is the overlap with growing relative intensity absorbance from triplets formed through ISC, though comparatively slow energy transfer mechanisms likely also play a factor. For PTMTT, BPA was only collected using 480 nm excitation and the results agree fairly well with

NT, despite an initial relaxation of approximately 0.05 akin to that seen for TO. Given the lack of an accompanying process in its TA spectra (Figure 4.5b), the rapid <1 ps relaxation seen in the anisotropy of the 480 nm excitation of TO likely does not result from exciton annihilation or a rapid relaxation of ordered excitations. Instead, the observation likely indicates that lower energy excitations reorient on an ultrafast timescale to conformations that stabilize the S_1 state and is independent of how 400 nm generated excitons relax structurally.

Examining $r(t, \lambda)$ of the TI-PTMT nanoaggregates excited at 400 nm compared with solution-phase TI, reveals little change spectrally in response to the presence of adjacent polymer strands. The anisotropy does decay much more rapidly for the aggregates, with a singlet band lifetime of 2.7 compared to 830 ps. This decrease in anisotropy lifetime evidences that significant interaction occurs between adjacent polymer strands in an aggregated environment, resulting in rapid decay with no accompanying shift in the transient absorption profile. Intermolecular energy transfer is a viable explanation, as migration of the excitation to similar conformers on adjacent polymer strands would support the rapid decline in anisotropy without an accompanying shift or decline in intensity that would accompany either a conformational reorganization of the molecule or transfer to a different energy-accepting chromophore. Therefore it is likely that excitations in an aggregated environment of one of these polymeric materials are able to migrate across reasonable distances without forming delocalized excitations that span over multiple chromophores (i.e. polaron pairs discussed previously). Unlike TA, BPA also provides a handle on how rapidly these dynamics occur and could be combined with estimated PTMT stacking

behavior units in an aggregated environment to predict how rapidly and the distance over which energy transfer can occur. Discrepancies in triplet polarization memory following ISC are beyond the scope of the discussion here but are evident from comparisons of anisotropy contour plots at later time delays.

4.5 Conclusions

Transient absorption and electronic polarization anisotropies were used to characterize the photophysics of thiophene-methanoannulene-thiophene polymer systems. Photoinduced responses and signatures of ultrafast transients were monitored to develop a better understanding of the steric perturbations introduced by substituents, how adjusting the excitation energy impacted resulting dynamics, and what effects aggregation and incident intermolecular interactions had on transient states. Hexyl side chain substituents twist certain bond angles led to modest spectral shifts and only minorly impact photodynamics. TTMTT illustrated the presence of PP-like states not seen for PTMTs. Aggregation of the PTMT polymers caused far more rapid decay kinetics, but did not result in any additional spectroscopic features or suggest that new transients were formed intermolecularly. Higher energy excitation generally led to induction lifetimes of <1 ps and slightly lower polarization anisotropies, with TO-PTMT showing evidence of heterogeneous domains through discrepancies in anisotropy relaxation.

4.6 Acknowledgments

These molecules were provided to our lab through collaboration with Professor J.D. Tovar and his research group, specifically Ben Streifel for synthesizing them and conducting steady state analyses. Wenjian Yu conducted preliminary ultrafast studies of the PTMTs which laid the groundwork for this analysis.

References

1. Streifel, B. C., Peart, P. A., Martínez Hardigree, J. F., Katz, H. E., and Tovar, J. D. *Macromolecules* **45**(18), 7339–7349 (2012).
2. Streifel, B. C., Zafra, J. L., Espejo, G. L., Gómez-García, C. J., Casado, J., and Tovar, J. D. *Angew. Chem. Int. Ed.* **54**(20), 5888–5893 (2015).
3. Guo, J., Ohkita, H., Bente, H., and Ito, S. *J. Am. Chem. Soc.* **131**(46), 16869–16880 (2009).
4. Zhou, J., Yu, W., and Bragg, A. E. *J. Phys. Chem. Lett.* **6**(17), 3496–3502 (2015).
5. Yu, W., Donohoo-Vallett, P. J., Zhou, J., and Bragg, A. E. *J. Chem. Phys.* **141**(4), 044201–044201 – 13 (2014).
6. Gao, B.-R., Wang, H.-Y., Wang, H., Yang, Z.-Y., Wang, L., Jiang, Y., Hao, Y.-W., Chen, Q.-D., and Sun, H.-B. *IEEE J. Quantum Electron.* **48**(3), 425–432 (2012).
7. Cook, S., Furube, A., and Katoh, R. *Energy Environ. Sci.* **1**(2), 294–299 (2008).

Chapter 5

Photoinduced Electron Transfer within Supramolecular Donor–Acceptor Peptide Nanoassemblies under Aqueous Conditions

5.1 Abstract

Photoresponses of peptidic supermolecular assemblies of conjugated oligomers designed for biological compatibility were interrogated to evaluate their overall effectiveness at prolonged charge separation, estimate distances over which charges could migrate and separate, and measure charge separation and recombination timescales. Transient absorption (TA) and broadband polarization anisotropy (BPA) were used to examine the impact of supermolecular assembly on photoinduced dynamics in peptide-based 4T-NDI donor acceptor dyads of varying donor-acceptor separation distances. Photoexcited dyads were shown to engage in donor-to-acceptor charge transfer, with a substantial increase in charge-pair lifetimes with aggregation (from 5 to 13.7 and >1000 ps lifetimes). TA measurements with mixed assemblies of donor-acceptor dyads and donor-only controls revealed signatures of excited state energy transfer or prolonged/long-range charge separation that spanned an average of three

to four donor units. Charge migration is illustrated to be minimal upon charge separation by consistent transition polarization anisotropies measured at late delays in BPA measurements.

5.2 Introduction

π -conjugated systems are noteworthy for their diverse array of intrinsic properties, not the least of which is the ability to behave as a semiconductor material for relaying electrical signals, creating localized fields, and facilitating specific reactions. A crucial undertaking in the development of such systems is finding a way to incorporate them into biologically compatible materials to apply these capabilities in bioelectronics, facilitate cellular processes, and serve as minimally invasive sensors. Peptidic supramolecular assemblies allow for conjugated materials to be systematically incorporated into environments in which they can form isolated organic monitors or interleave within protein and cellular structures to provide access to the functionality of ordinarily hydrophobic organic molecular units. Here, we discuss the interrogation of charge transfer systems in which an electron donor is positioned along a peptidic backbone, between and bound in close proximity to, a symmetrically spaced pair of electron acceptors added via imidation of lysine residues placed at set distances from the donor. The intent is to validate the ability of self-assembled stacks of these donor-acceptor dyads to spontaneously separate charge on an ultrafast timescale in response to light absorption and characterize the strength, duration, and mobility of these charge separated states.

Quaterthiophene (4T) and naphthalene diimide (NDI) were selected as the electron donating and accepting groups used within the donor-acceptor dyads studied here. Figure 5.1a shows the molecular dyad and controls units studied here, in which the 4T electron donor is located between two NDI acceptor or inert control moieties placed a set number of amino acid groups away, n , leading to the designations DA- n and C- n for the donor-acceptor dyads and controls respectively. 4T was selected as synthesis procedures for embedding it within a peptide network had been thoroughly examined and optimized previously¹, while NDI was selected for the ease with which it could be incorporated into a peptide chain via addition through lysine side-chains and its favorable electronic state energy levels.² The dyads were synthesized via a several step procedure involving N-acylation, exposure to Stille cross-coupling conditions, and concluded with removal of protective groups and imidation using the NDI acceptor or inert control group.³⁻⁵ Figure 5.1b depicts the specific steps of the synthetic procedure by which the dyads were generated with details omitted for brevity.

Additionally, NDI was selected as it was anticipated that charge transfer from excited 4T would occur with minimal energy transfer and inhibited charge recombination based on the positions of their electronic energy levels relative to one another. The highest occupied molecular orbitals (HOMO) and lowest unoccupied molecular orbital (LUMO) of 4T and NDI are qualitatively shown in Figure 5.1c. By design, photoexcitation of the 4T unit should produce a transient state by which electron transfer from (Figure 1.3) 4T to NDI but not from NDI to 4T as NDI's LUMO lies lower in energy than 4T's, thereby permitting acceptance of the electron into the lower level orbital provided there is sufficient overlap. Furthermore, as the 4T

should only produce NDI^- and 4T^+ charge separated states, which both have distinct spectroscopic signatures as seen previously.^{6,7}

Stacking between substituted peptides is controlled in large part by the pH of the surrounding aqueous environment. The substituted peptides are designed such that their theoretical structures exhibit C_2 symmetry and permit vertical π -stacking of 4T units tilted by yaw angles typically between 10-30°. An idealized example of this stacking is shown as Figure 5.2a. In truth, the assemblies are stacked significantly more randomly than this ideal picture due to entropic effects. The formation of these extended π -conjugated networks is facilitated by hydrogen bonding networks established between carefully tailored amino acid groups on adjacent strands. In neutral and acidic pH's solutions, the dyads can form relatively long fibular aggregates as shown transmission electron microscope (TEM) images collected for various dyads in Figure 5.2b. However, basic environments result in deprotonation of terminal carboxylic acid groups, whereby the now negatively charged carboxylates repel one another and disrupt the formation of nearly every aggregate, leading to the isolation of most peptides in solution. Interrogating and contrasting each aggregation condition allows for details of the inter- and intra-molecular charge transfer profiles of the dyads to be explained. Since formation of persistent charges could not be identified from steady-state UV-vis measurements, broadband ultrafast transient absorption (TA) spectroscopy can be used to probe the formation of charged species and assess how the properties of the dyad structures control charge separation and recombination kinetics when they are assembled versus unassembled in aqueous solutions.

Evidence elicited from steady state photoluminescence of mixtures of DA-*n*

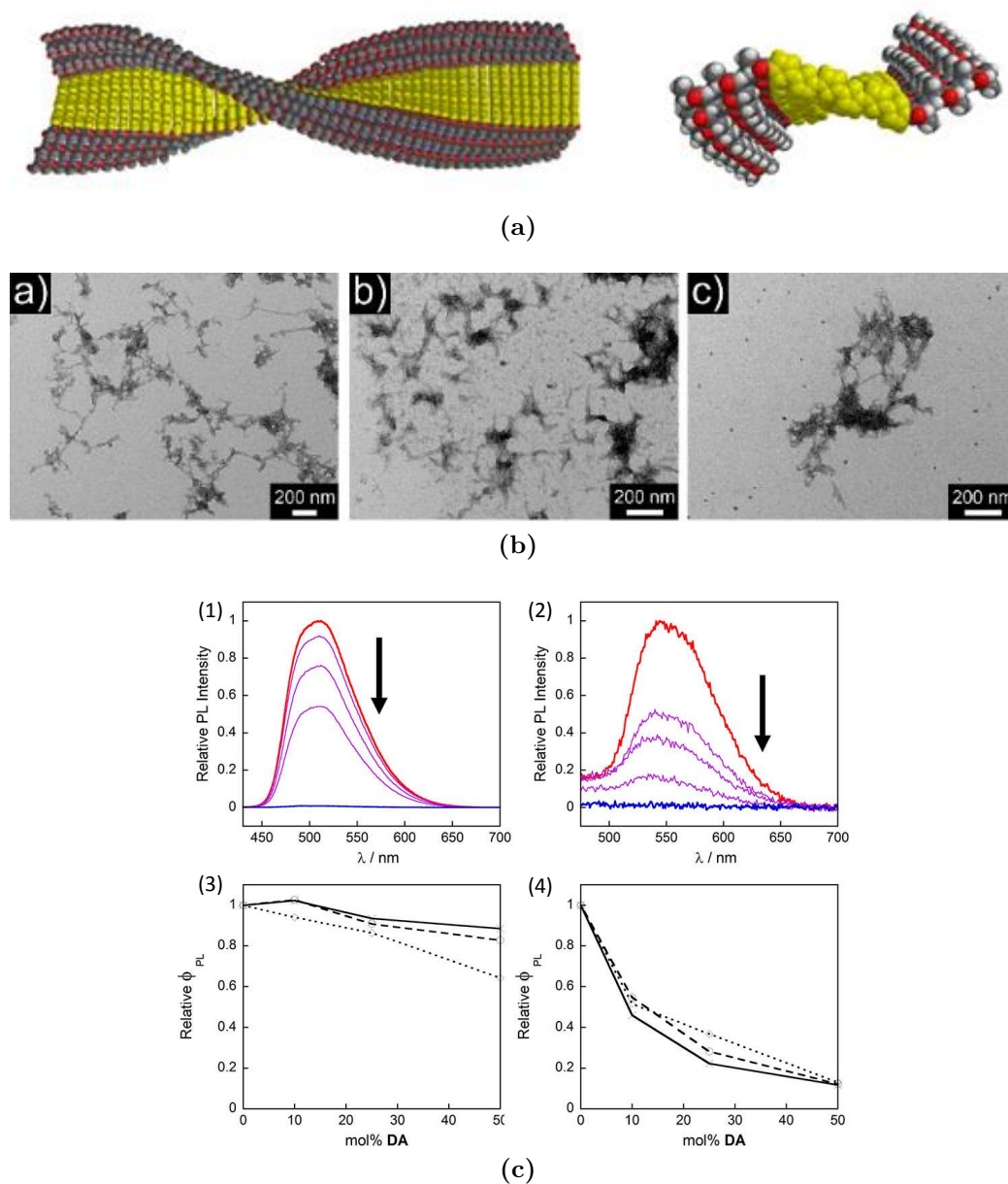


Figure 5.2: Dyad Stacking, Aggregates, and Photoluminescence: (a) idealized rendition of dyad assembly with adjacent 4T units stacked with a yaw angle offset of 10° , (b) TEM images of DA-6, DA-3, and DA-2 fibrous supramolecular assemblies, and (c) photoluminescence of 4T control molecules with increasing mol% of dyad unassembly (1 and 3) vs. assembly (2 and 4)]

and C-*n* molecules has shown the potential for energy migration between assembled 4T groups. Figure 5.2c shows fluorescence data collected for pure C-2 (red) through mixed ratios with increasing amounts of DA-2 to pure DA-2 (blue) for unassembly

(1) and assembled (2) molecules. The dotted spectra from the mol% plots of unassembled (3) and assembled (4) show the relative integrated fluorescence quantum yields as a function of mole percentages of dyad. Here, relative fluorescence quenching is constantly greater in the case of the assembled dyad mixtures in comparison to those in isolation, indicating the potential for 4T to shuttle excitation energy along an assembly from control to dyad sites whereby charge separation can occur and quench singlet excitons that would otherwise luminesce. Other factors can lead to this same behavior though, namely the ability of NDI to disrupt stacking or modify relevant chromophores. Thus, to confirm the presence of energy transfer the ultrafast behaviors of mixed assemblies can be explored. Proportional control:dyad random assemblies can be prepared to determine the extent to which excited state transients can migrate along 4T stacks (if at all) before charge separating. Finally, broadband polarization anisotropy (BPA) can be used to track the positions of various transients within the assemblies and predict how far charges (predominantly $4T^+$) can migrate and on what timescales these phenomena will occur.

5.3 Experimental Methods

4T-NDI peptidic dyads with synthesized by Allix Sanders of the Tovar group to incorporate a pair of NDI moieties spaced symmetrically about a centrally positioned 4T moiety separated by various numbers of amino acids as seen in Figure 5.1a. Each dyad is labeled as DA- n , with n signifying the number of amino acid groups separating the donor from the acceptor (or control moieties) as stated above. DA-2 and C-2

were the primary molecules examined within this study and are shown as the bottom molecule in Figure 5.1b. Each solid sample was dissolved in DI-water, as received, to a concentration of approximately 0.02 mg/mL. These samples were then split in half with an equivalent amount of 0.1 M hydrochloric acid (HCl) added to one and 0.1 M potassium hydroxide (KOH) to the other (several drops) such that the pH of each sets was <4 and >10 , respectively. Mixed assemblies of DA-2 and C-2 were prepared by combining stoichiometric ratios of solutions of a common concentration, adding a small amount of KOH to fully deprotonate and unassemble both molecules, and then stirring in enough HCl to reduce the pH below four to re-induce randomized assembly. While ionic strength is a significant factor in determining how these peptidic molecules assemble, this property of the solution was not tightly controlled as part of the preparation methodology for these samples.

TA and BPA spectroscopies were applied in accordance with details provided in Chapter 2. The 4T moiety was photoexcited using 400 and 480 nm pump pulses and probed for changes in transient absorptivity with broadband continua over the range of 425-1150 nm. A modified singular value decomposition (SVD) analysis, akin to global analysis (GA), was performed with transient spectra of both isolated and assembled DA-2 to extract the spectral and temporal characteristics of each two component system. Descriptions of the mathematical techniques used in analyzing this data are presented in Section 2.5 or included as necessary to accompany results below.

5.4 Results and Discussion

5.4.1 Transient Absorption of Dyads and Spectral Component Isolation and Characterization

Figure 5.3 presents the spectral dynamics of (a) unassembled and (b) assembled DA-2 dyads in aqueous solution following 400 nm excitation. This excitation wavelength approaches the absorption onset for NDI, and while control measurements were conducted at 480 nm, the red side of the steady-state 4T spectrum, the similarity in the spectral dynamics observed at the two excitation wavelengths supports that the 4T moiety is still selectively excited by the 400 nm pulse. Variations in spectral dynamics with excitation fluence were also examined to ensure that spectral dynamics were not a result of two-photon excitation or dynamics of biexcitations. Five transient spectral features can be identified from this spectral progression: a negative signal below 475 nm corresponding with bleaching of the 4T ground-state absorption band (GSB), three transient absorption (TA) bands centered at approximately 500, 670, and 1100 nm, and a rather broad absorption band centered around 775 nm. All features appear almost immediately upon excitation. Whereas the broad feature centered at 775 nm disappears within a few hundred femtoseconds (fs), the other features persist and concomitantly decay on a longer 5 picosecond (ps) timescale.

Figure 5.4 presents principal spectral and kinetic components obtained from a modified SVD algorithm applied to the data presented in Figure 5.3. These extracted components validate the presence of two primary spectral patterns upon excitation

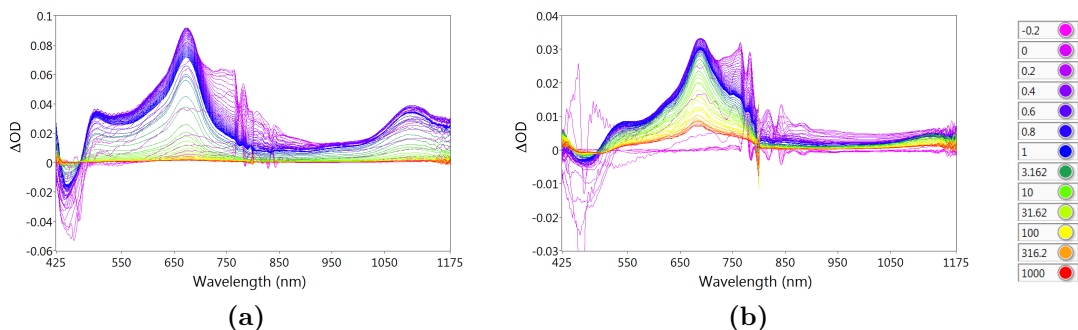


Figure 5.3: Transient absorption spectra of DA-2 dyads: (a) unassembled (b) assembled with Δt color key shown to the right

with associated kinetic behaviors. Figure 5.4a reveals that the broad band centered near 775 nm with a corresponding GSB signal decays within the first picosecond after excitation and resembles the spectrum of isolated 4T photoexcited to its S_1 state as measured in previous works.^{8–10} By contrast, the remaining bands closely match signatures corresponding to reduced NDI or oxidized 4T. The 500 nm band and shoulder at 750 nm match features in the spectra of NDI^- ,^{6,11} while the band at 670 nm matches the well-known absorption band of 4T^+ .⁷ The near infrared (NIR) absorptive band at 1100 nm is thought to be a combination of signal due to both oxidized 4T and a reduced NDI dimer.^{8?} The presence of these bands and their simultaneous decay with concomitant recovery of the 4T bleach indicate that photoexcitation induces charge separation between the donor and acceptor moieties within the unassembled dyad. Charge recombination then occurs on the aforementioned 5 ps timescale.

There are no spectral or temporal signatures suggesting that peptide regions serve as charge acceptors or donors at any point following excitation. However, principal kinetic components plotted in Figure 5.4b demonstrate that charge separation occurs from the photo prepared excited state via two modes. A portion of the charge

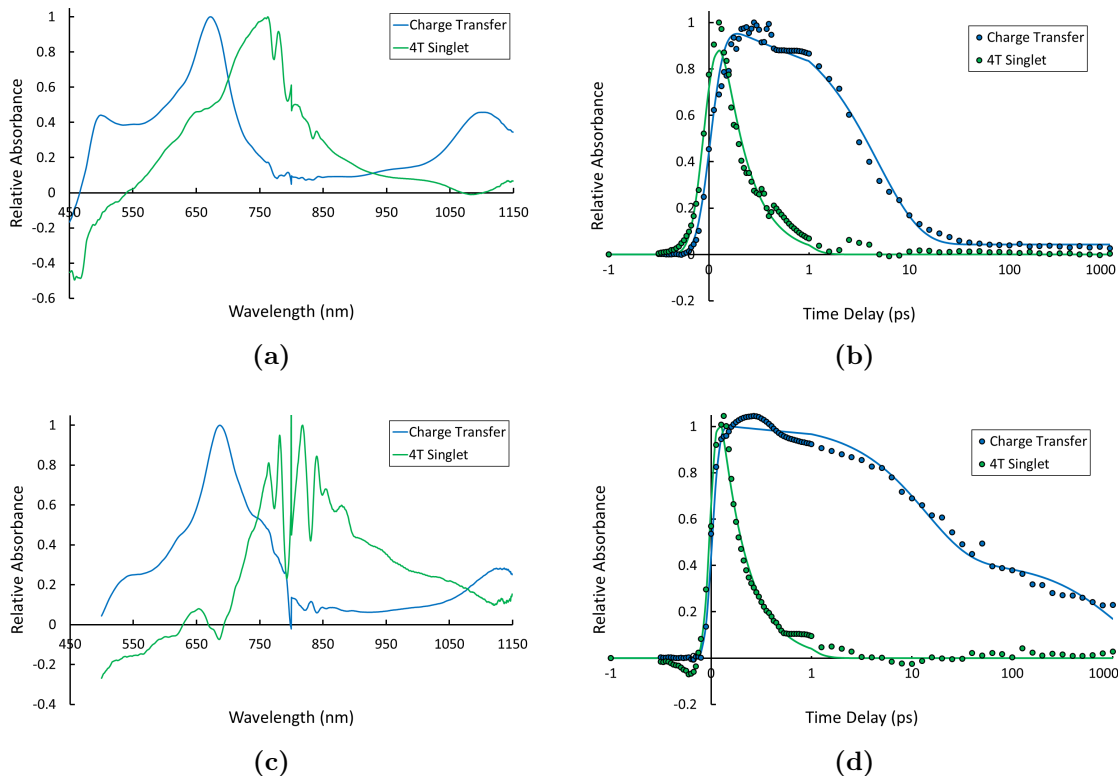


Figure 5.4: Isolated Components from SVD analysis of DA-2 TA Spectra: (a) unassembled and (c) assembled DA-2 spectral profiles and (b) unassembled and (d) assembled associated kinetic progressions with applied regression traces

transfer transients are formed promptly, i.e. within the time resolution of the experiment, while the rest are formed on a delay corresponding to the decay timescale of ≈ 270 fs ascribed to relaxation the S_1 excited state of 4T. The observation of two modes for separating charge suggests that conformation or charge of the bridging peptide impacts the electronic coupling between the 4T and NDI moieties. The transients in Figure 5.4b also reveal that charge separated species recombine predominantly on the 5 ps timescale, with only a small fraction ($\approx 4\%$) persisting onto a nanosecond timescale. Observation of two recombination timescales may reflect differences in the reorganization energy for charge recombination due to peptide conformation or charge. However, the possibility that a fraction of the dyads assemble in solution

even under basic conditions may provide an alternative explanation.¹²

Characteristic decay timescales of the local 4T excitation and charge-separated pairs were obtained as principal components through an SVD procedure similar to GA. Equations 5.1 and 5.2 provide the kinetic models of the system to facilitate separation of component spectra due to each state. $S(t)$ corresponds to the short-lived S_1 state of 4T, whereas $CS(t)$ corresponds to the coupled charge-separated state ($4T^+/NDI^-$). Table 5.1 presents values of fitting parameters determined for kinetic models involving exponential decay functions convoluted with the temporal instrument response. The rise in the CS signal for unassembled and assembled DA-2 was fit with an approximately 270-fs rise observed from the decay of S_1 4T.

$$S(t) = f_S e^{(-t/\tau_{S1})} \quad (5.1)$$

$$CS(t) = f_{CS1} e^{(-t/\tau_{CS1})} + f_{CS2} e^{(-t/\tau_{CS2})} \quad (5.2)$$

Figure 5.3b shows the transient spectral dynamics observed following 400 nm excitation of a suspension of assembled DA-2 dyads in aqueous solution. The shapes and positions of the transient spectra are qualitatively similar to those observed with unassembled dyads, except that the 500, 670, and 1100 nm transient bands associated with charge-separated species are red-shifted by 20-25 nm and broader. Furthermore, 4T's short-lived S_1 absorption also extends over throughout the spectral NIR and overlaps the absorption of NDI^- around 1125 nm. This breadth and substantial redshift in the 4T absorption features are consistent with stacked chromophores in assemblies.⁸

	Unassembled	95% CI	Assembled	95% CI
f_{CS1}	0.958	0.893-1.057	0.585	0.461-0.709
τ_{CS1} (ps)	4.84	3.35-6.35	13.7	6.4-26.2
f_{CS2}	0.042	-0.012-0.097	0.415	0.286-0.0544
τ_{CS1} (ps)	Constant	—	1106	461-Constant
τ_{S1}	0.269	0.203-0.305	0.276	0.228-0.330

Table 5.1: DA-2 Component Kinetic Fit Parameters

Figures 5.4c and 5.4d present the corresponding principal spectral and kinetic components, respectively, obtained through the same SVD related procedure used previously for unassembled dyad spectra. Spectral components plotted in Figure 5.4c are highly similar to those obtained with unassembled dyads. Furthermore, the signature of S_1 4T decays on comparable time scales for both cases, once again around 270 fs, suggesting that charge-transfer dynamics are similar in the two environments and that any energy transfer along the 4T core of an assembly may be limited by the rate of ultrafast charge separation. In contrast, the kinetics of charge recombination differs markedly: whereas recombination occurs on picosecond time scales in unassembled dyads, roughly 40% of separated charges persist for timescales of hundreds of picoseconds to nanoseconds in assemblies (Table 5.1). This observation indicates that 4T stacking (and potentially NDI stacking) provides the ability for charge pairs to migrate or separate over prolonged intermolecular distances along the assemblies. Alternatively, assembly of the dyads may change the driving force or reorganization energy for charge recombination of proximal charge pairs. Nonetheless, these results demonstrate that an increase in the charge-separation lifetime is achieved through aggregation.

5.4.2 Comparisons to Other Dyads and Dyad/Control Mixtures to Identify Energy Transfer

Only modest differences in the transient spectral dynamics are observed for both unassembled and assembled dyads upon increasing the excitation wavelength to 480 nm and with no appreciable change in excited-state and charge-pair lifetimes (Figure 8.4). Figure 5.5a shows that there is little to no fluence dependence observed in the spectral dynamics measured in assembled DA-2, as the signals maintain a constant spectral shape and fairly consistent decay lifetimes over a wide range of excitation fluences. This confirms that the charge separation observed for DA-2 is not due to two-photon transitions or exciton annihilation and is reflective of the photodynamics of the dyad in applications involving lower fluences or peak powers. By contrast, the transient spectra of C-2 control assemblies exhibit signatures of $4T^+$ at high fluence and long-lived $4T$ S_1 signal at lower fluences as shown in Figure 5.5b and seen previously.¹³ This demonstrates that donor-acceptor charge separation competes with and likely dominates multi-photon excitation and annihilation mechanisms along the $4T$ core within the dyad systems.

Transient absorption data was also collected for dyad structures with longer separation distances. The spectroscopic signatures and dynamics of DA-2 are highly representative of the structures with longer separation distances. Transient absorption spectra associated with DA-3 and DA-6 (unassembled and assembled), as shown in Figure 8.5, show no substantial spectral differences relative to DA-2. Comparisons of the time-dependent traces from integrated regions associated with $4T^+$, NDI^- , and

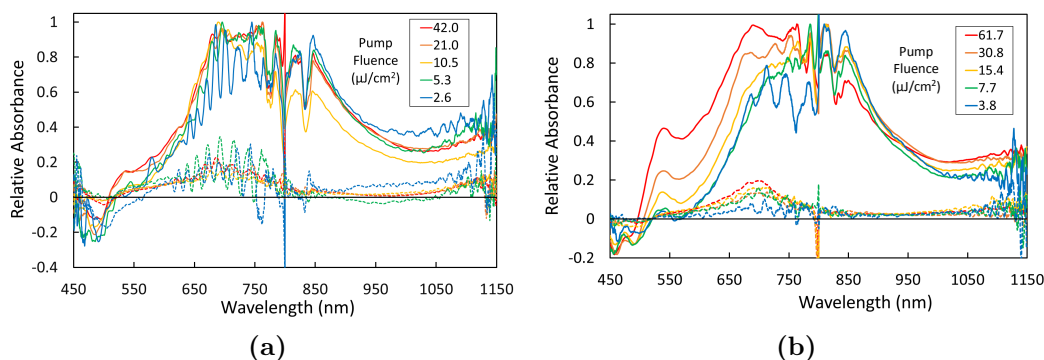


Figure 5.5: Fluence Dependence of DA-2 and C-2 Excited at 400 nm: (a) assembled DA-2 and (b) assembled C-2

S_1 4T absorbances for the various dyad structures are included as Figure 8.6. These decay traces show few differences amongst different separation lengths other than that unassembled DA-2 exhibits a longer-lived population of S_1 (out to a nanosecond timescale) not seen in DA-3 or 6. Spectral dynamics and their time dependence do not vary substantially across the set of unassembled or assembled dyads, regardless of the length of the bridging peptide (and therefore the donor-acceptor separation). Hence, we conclude that the dynamics of photoinduced electron transfer and resulting recombination are not impeded by D-A distance on the length scales of the peptide linkers assessed here, and our general conclusions about charge-transfer in isolated and assembled dyads are valid for all three structures. Figures associated with differences in pump wavelength and comparisons to DA-3 and DA-6, referenced here, are included in Appendix 8.3

Figure 5.6 presents absorption transients collected at 1100 nm under equivalent excitation fluences for control (C-2), dyad (DA-2), and mixed (C-2/DA-2) assemblies with raw spectra shown as (c), (e), and (d) of Figure 8.4, respectively. Significantly

different time dependence is observed at this probe wavelength for control and dyad assemblies, shown as the green and blue points and fit lines, respectively. TA from a randomly assembled of a 1 : 9 DA-2 : C-2 mixture exhibits intermediate behavior and is given by the yellow symbols and fit line. The intensity decay at this wavelength for mixed assemblies cannot be recovered through a 10-90% proportionate linear combination of the control and dyad traces (black dashed line). Rather, a 39%-61% combination of these pure-assembly transients (red dashed line) is necessary to adequately match the data observed experimentally for the mixed assembly system. This comparison indicates that photoexcitation enables some degree of delocalization or energy transfer and supports observations from steady-state measurements (Figure 5.2c). On statistical grounds, using Poisson statistical modeling, this suggests that excitations leading to the charge transferred transient exhibit an effective average delocalization of three to four donor moieties.^{14,15}

5.4.3 BPA and Comments on Prevalence of Charge Migration

BPA was also conducted on DA-2 to interrogate the extent of energy or charge migration within the assembled units prior to and after charge separation, respectively. Figure 5.7 shows decay traces taken from visible and NIR absorption bands within BPA spectra of assembled DA-2 using excited at 400 nm. Table 5.2 contains the relative anisotropies and their relaxation timescales for the bands located at 690 and 1125 nm seen from Figure 5.3b. Previous literature findings support the assignments of the visible and NIR bands as being associated with the $4T^+$ and a combination of

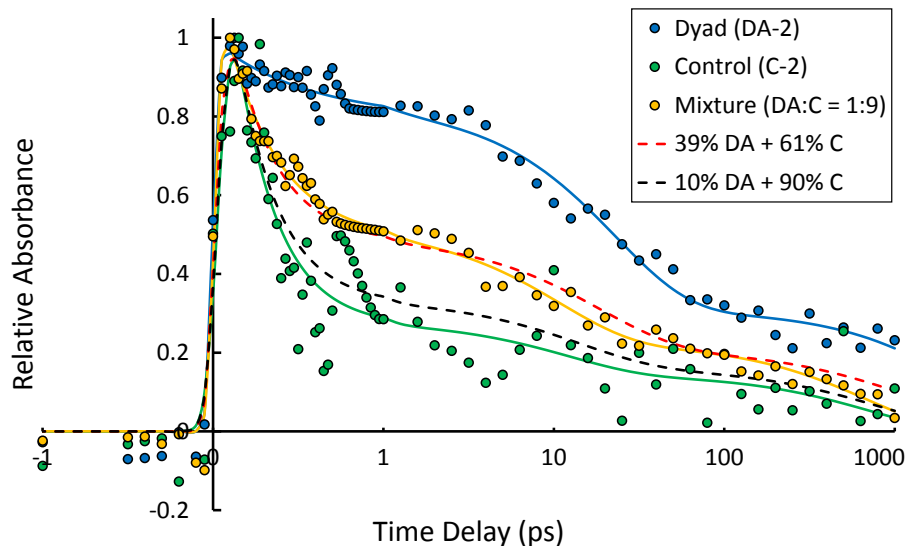


Figure 5.6: DA-2, C-2, and 10:90 Mixture Decay Trace Comparison: dashed lines represented linear combinations corresponding to a binary mixture of signatures based on number density (black) and one fitted to experimental data empirically (red).

$4T^+$ and NDI^- components, respectively which can help in providing plausible explanations for how to interpret parameters determined from associated fits. Namely, the six-fold faster and greater in magnitude recovery of the anisotropy of the band only associated with $4T^+$ suggests that the positive hole is capable of migrating much more rapidly and to a greater extent than the comparable process within the NDI^- polaron. This discrepancy agrees with conclusions derived previous results showing evidence of energy transfer, that a sizable amount of $4T$ π -orbital overlap facilitates migration of associated states. Similarly the result suggests that NDIs either do not exhibit the same π -overlap, do not stack as effectively, or do not move as much following charger transfer. The comparable long lived anisotropies indicate that the charge pairs remain relatively static onto the nanosecond time domain, and that at this point it may be possible for the $4T^+$ polaron to migrate independently of the co-stabilized NDI^-

polaron which (by comparison) remains more static. The timescale associated with the NDI^- polaron anisotropy relaxation is an order of magnitude slower than that of the 4T^+ , but can be considered constant as the measurements are only collected out to 1 ns and cannot precisely estimate such lengthy timescales. BPA provides key evidence that charge migration along the β -sheet assemblies is minimal and that significant charged transient dipole shifting occurs mostly within the timeframe of additional charge pair formation less than 1 ps after photoexcitation.

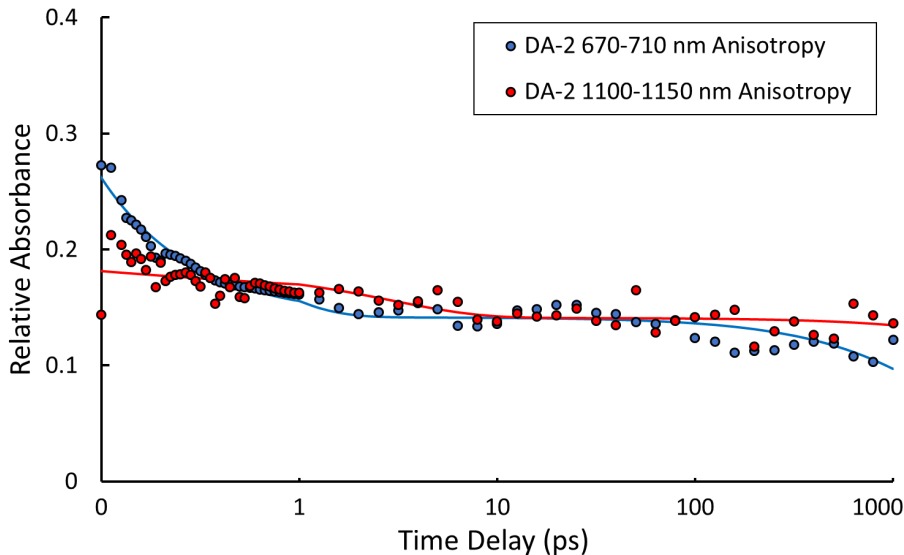


Figure 5.7: Polarization Anisotropy of DA-2: integrated decay traces of BPA collected for assembled DA-2 in regions ascribed to the visible and NIR absorption bands of the charge transfer state. Both wavelength regimes indicate a rapid relaxation of a portion of the anisotropy on a 0.5-3 ps timescale with greater than half of the anisotropy (and >0.1) persisting onto a ns timescale.

	670-710 nm	1100-1150 nm
r_1	0.12	0.04
τ_1 (ps)	0.47	2.97
r_2	0.14	0.14
τ_2 (ps)	2650	21700

Table 5.2: DA-2 Anisotropy Decay Parameters

5.5 Conclusions

We have studied several variations of a novel donor-acceptor π -peptide hybrids, which can self-assemble to form unidirectional, fibrous nanoassemblies in aqueous media. These peptidic dyads undergo photoinduced electron transfer from the initially excited, 4T donor to the peripherally attached NDI acceptor moieties, as demonstrated explicitly by TA spectroscopy. Electron transfer is observed to occur in part promptly, i.e. (<100 fs within instrument response) as well as on a delay of 270 fs corresponding to relaxation of the S_1 state of 4T for assembled and unassembled dyads. This suggests that structural heterogeneities (e.g., conformation or peptide charge) likely impact charge-separation dynamics. Additionally, assembly of donor-acceptor hybrids yields a one to two order of magnitude increase in the resulting charge-separation lifetime, with charges persisting into the nanosecond regime. Co-assemblies were used to dilute the key donor-acceptor unit within a matrix of energy-harvesting donor peptides and provided an avenue for directing energy migration through this nanostructured matrix to a more remote acceptor site. Enhancement of the charged transient signatures which were disproportionate to a composition of dyad and donor-only control molecules supports steady-state quenching of photoluminescence from the donor and validates/clarifies the associated energy transfer processes. Overall, supramolecular platforms offer the unique possibility of merging electric-field creation into biologically relevant nanomaterials and have been shown to viably generate long lived internal electric fields upon photoexcitation as a result

of these ultrafast spectroscopic studies.

5.6 Acknowledgments

Professor J.D. Tovar and his group handled fabrication and much of the steady state characterization of the dyad systems described in this chapter. Primarily, I would like to acknowledge Allix Sanders for synthesizing the DA-*n* and C-*n* used in this study, characterization of the steady state properties: namely, characteristics of their assembly and trends in photoluminescence. I would also like to acknowledge and thank Dr. Michael McCaffery from the JHU integrated imaging center (IIC) staff for assisting me with cryo-transmission electron microscope (TEM) measurements of the dyad molecules prior to publication, though these results were not presented here.

References

1. Vadehra, G. S., Wall, B. D., Diegelmann, S. R., and Tovar, J. D. *Chem. Commun.* **46**(22), 3947–3949 (2010).
2. Bheemaraju, A., Pourmand, M., Yang, B., Surampudi, S. K., Benanti, T. L., Achermann, M., Barnes, M. D., and Venkataraman, D. *J. Macromol. Sci. Part A* **48**(12), 986–993 (2011).
3. Liddell, P. A., Kodis, G., Moore, A. L., Moore, T. A., and Gust, D. *J. Am. Chem. Soc.* **124**(26), 7668–7669 (2002).
4. Beckers, E. H. A., Meskers, S. C. J., Schenning, A. P. H. J., Chen, Z., Würthner, F., Marsal, P., Beljonne, D., Cornil, J., and Janssen, R. A. J. *J. Am. Chem. Soc.* **128**(2), 649–657 (2006).
5. Shao, H., Nguyen, T., Romano, N. C., Modarelli, D. A., and Parquette, J. R. *J. Am. Chem. Soc.* **131**(45), 16374–16376 (2009).
6. Bhosale, S. V., Jani, C. H., and Langford, S. J. *Chem. Soc. Rev.* **37**(2), 331–342 (2008).
7. Paul A van Hal, E. H. A. B. *Chem. Weinh. Bergstr. Ger.* **8**(23), 5415–29 (2002).

8. Zhou, J., Yu, W., and Bragg, A. E. *J. Phys. Chem. Lett.* **6**(17), 3496–3502 (2015).
9. Lap, D. V., Grebner, D., and Rentsch, S. *J Phys Chem A* **101**, 107–112 (1997). 107.
10. Benincori, T., Bongiovanni, G., Botta, C., Cerullo, C., Lanzani, G., Mura, A., Rossi, L., Sannicolò, F., and Tubino, R. *Phys Rev B* **58**, 9082–9086 (1998).
11. Ivnitski, D., Amit, M., Rubinov, B., Cohen-Luria, R., Ashkenasy, N., and Ashkenasy, G. *Chem. Commun.* **50**(51), 6733–6736 (2014).
12. Jayasuriya, N., Kagan, J., Owens, J. E., Kornak, E. P., and Perrine, D. M. *J. Org. Chem.* **54**(17), 4203–4205 (1989).
13. Magnanelli, T. J. and Bragg, A. E. *J. Phys. Chem. Lett.* **6**(3), 438–445 (2015).
14. Spano, F. C., Meskers, S. C. J., Hennebicq, E., and Beljonne, D. *J. Am. Chem. Soc.* **129**(22), 7044–7054 (2007).
15. Herz, L. M., Daniel, C., Silva, C., Hoeben, F. J. M., Schenning, A. P. H. J., Meijer, E. W., Friend, R. H., and Phillips, R. T. *Phys. Rev. B* **68**(4), 045203 (2003).

Chapter 6

Photoinduced Energy Transfer within Aqueous Co-assemblies of Conjugated Poly-Electrolytes

6.1 Abstract

Transient absorption (TA) studies were conducted the conjugated polyelectrolytes (CPEs) poly-([fluorene]-alt-co-[phenylene]) iodide (PFPI), potassium poly-alkylcarboxythiophene and their complexes (CPECs) in aqueous solutions to investigate the kinetics of exciton energy transfer (EET). Pure and mixed (PFPI-PTAK) assemblies of PFPI (donor) and PTAK (acceptor) in varying proportions were excited at 360 nm to preferentially excite PFPI and 600 nm to selectively excite PTAK. The fluence dependence associated with CPECs selectively excited at 600 nm were observed to vary with donor:acceptor (charge) ratio, reflecting morphological changes in the PTAK component with assembly composition. Comparison of a predominantly PFPI-based CPEC excited at 360 nm, PFPI excited at 360 nm, and the PTAK component of the same CPEC selectively excited at 600 nm provided clear evidence of ultrafast EET from PFPI to PTAK in CPECs.

6.2 Introduction

Developing photosystems that efficiently absorb light to drive energy and electron transport in order to harvest solar energy is a grand challenge for the photophysics community. Conjugated organic materials that emulate biological light-harvesting systems and can be manufactured on a commercial scale have remained of particular interest in this regard.^{1,2} Although much work has been done with organically processed materials and devices, a natural extension for light harvesting compounds is to improve the feasibility of processing them in aqueous environments, particularly by designing them as part of water-soluble hierarchies.³⁻⁵ In this way, conjugated poly-electrolytes (CPEs) combine polymeric chromophores possessing useful electronic properties with chargeable end groups that facilitate dissolution and complexation in aqueous solutions.

The goal of the work presented herein was to evaluate how stacking and intermolecular interaction between two components of energy donor-acceptor CPE complexes (CPECs) impact their potential for energy harvesting. Figure 6.1a presents the structures of poly-([fluorene]-alt-co-[phenylene]) iodide (PFPI) and potassium poly-alkylcarboxythiophene (PTAK). These CPEs are highly complementary for light-harvesting applications given their relative electronic bandgaps: Figure 6.1b shows the absorption spectra of PFPI and PTAK as well as the photoluminescence spectrum of PFPI. The strong overlap between the emission spectrum of PFPI and the steady state absorption of PTAK indicates that energy emitted by PFPI can be absorbed by

PTAK. If the two are assembled within reasonable proximity, Förster energy transfer (Figure 1.2) from photoexcited PFPI to PTAK via electronic energy transfer (EET) should be feasible. Other supramolecular assemblies have been constructed based on this design principle, and highlight the ability for energy transfer between phenylene and thiophene-based moieties.⁶ As PTAK and PFPI are oppositely charged, they can be carefully mixed in solution to form CPECs. PTAK and PFPI have been predicted to stack orthogonally in complexes due to electrostatic attraction between their oppositely charged side chains.

In fact, previous measurements of steady state fluorescence from PFPI:PTAK CPECs have shown that EET is possible from the PFP chromophore to the PTA acceptor based on the quenching of PFP and enhancement of PTA emission in response to selective photoexcitation of PFP.⁷ Figure 6.1c shows steady state photoluminescence spectra collected for several preparations of PFPI, PTAK, and mixed CPECs. Addition of as little as 20 %wt PTAK to a PFPI electrolyte solution quenches nearly all of the PFPI's fluorescence and yields a sizable PTAK photoluminescence signature. Notably, PTAK fluorescence is significantly shifted in the case of excitation of and EET from PFPI, which may reflect the impact that PFPI has on local PTAK ordering and interactions that impact its emission characteristics (e.g. formation of aggregates) rather than any energetic discrepancies arising from the source of PTAK excitations.

Though this evidence illustrates EET quite clearly, steady state measurements do not fully explain the photodynamics of this process, including underlying ultrafast kinetics and what conditions are both necessary and optimal for EET. In light of

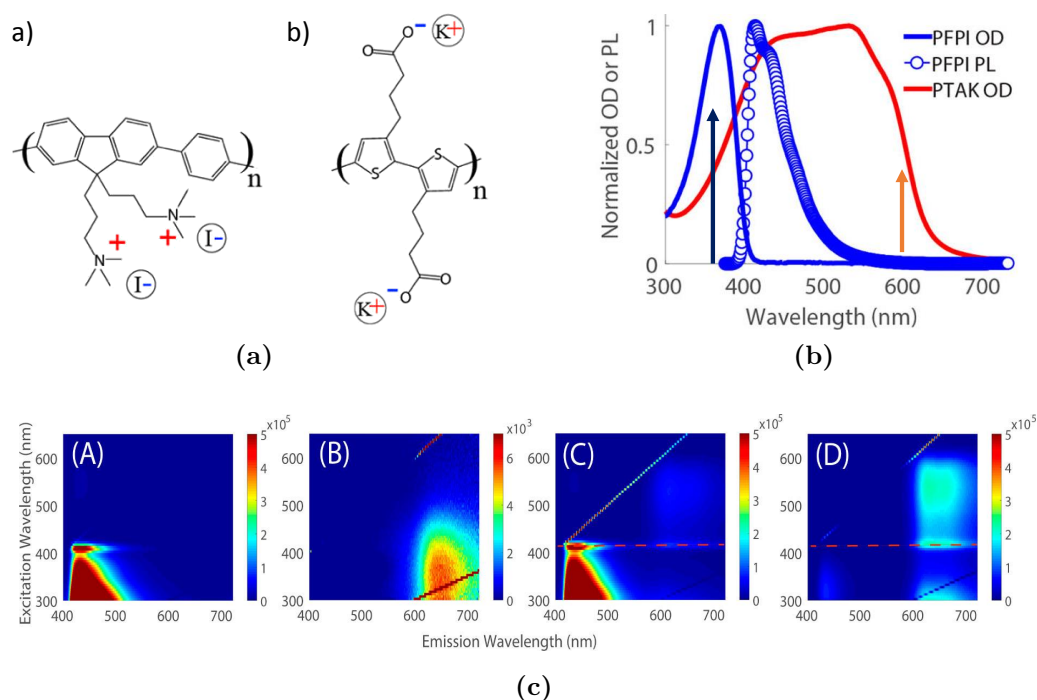


Figure 6.1: PFPI and PTAK Steady State Properties: (a) molecular structures of a) poly((fluorene)-alt-co-(phenylene) iodide (PFPI) and b) potassium poly(alkylcaroxythiophene) (PTAK)⁷, (b) UV-Vis steady state absorption spectra of PFPI and PTAK⁷ where dark blue and orange vertical arrows show 360 and 600 nm excitation respectively, (c) fluorescence emission spectra of (A) PFPI, (B) PTAK, (C) CPEC 99:1, and (D) CPEC 80:20 as a function of excitation wavelength.⁷

this, further examination using ultrafast spectroscopies has the potential to determine the timescales over which EET occurs, for what ratio the process may be the most efficient, and to establish more accurate characterizations of CPEC structure and intermolecular dynamics. Transient absorption (TA) can also yield information pertaining to the nature of transients produced in pure and mixed CPE environments.

6.3 Experimental

CPEC solutions were prepared and provided by the Ayzner group (UCSC) at fixed concentration ratios ranging from 20:80 to 80:20 %wt PFPI:PTAK in increments

of 20% (labeled as CPEC n:100-n (%wt's)). Pure PFPI and PTAK controls, labeled as PFPI- or PTAK-n, were also provided at each incremental absolute concentration loading used to prepare each CPEC. As the interaction between individual CPEs is not dependent on concentration, PFPI-40 and PTAK-60 were selected as controls to measure the pure CPE photophysics of each based on their optical densities. Electronic absorption characteristics were verified by UV-Vis spectra. Solutions were used as received and transferred to stirred 2mm path length cuvettes for ultrafast spectroscopic measurements.

TA was conducted using the experimental set-up described previously in Section 2.4 with 360 and 600 nm excitation wavelengths to be preferentially and solely resonant with the electronic absorbances of PFPI and PTAK, respectively, as shown in Figure 6.1b. 600 nm only corresponds to resonance with the PTAK while 360 nm occurs at the wavelength where the PFPI:PTAK ratio of absorbance cross sections is the highest, ranging from 0.6:1 to 25:1 for 20:80 to 80:20 CPEC. TA measurements were collected with fluences ranging from 3 (low) to 400 $\mu\text{J}/\text{cm}^{-1}$ (high). Data collected at lower fluences (15 $\mu\text{J}/\text{cm}^{-1}$) was weakly impacted by multi-photon excitations of PTAK which complicate the analysis of EET dynamics. However, comparison of data collected at low and high fluences provide a window into the nature of intermolecular interactions between neighboring CPEs. Of the samples studied, only CPEC 40:60 showed degradation in response to prolonged experimentation, which was assumed to be predominantly due to passage of time since rather than incident exposure to femtosecond photoexcitation. TA was collected over the probe range of 450-1150 nm as two sequentially collected spectra (450-800, 800-1150 nm) scaled relative one another

to match and correct for modest discrepancies between the pump alignment or laser power fluctuations between measurements.

6.4 Results and Discussion

Figure 6.2 presents TA spectra obtained by exciting several samples with a range of PTAK compositions from pure PTAK-60 (Figure 6.2a) to 80:20 CPEC (Figure 6.2d) with 600 nm light to elicit the photophysical dynamics associated with direct excitation of PTAK in these various supramolecular environments. Without PFPI present, or with only very little present as is the case with 20:80 CPEC (Figure 6.2b), the transient spectra obtained are similar to those of thiophene assemblies presented in previously (Figure 3.2). Specifically, spectra include a ground state bleach with clear vibronic features (GSB) below 600 nm, a visible absorption feature at 650 nm arising from coupled polaron pair states, and a broad absorbance due to isolated charge separated states centered at 1025 nm. S_1 singlet excitons are also present to some extent at longer wavelengths, peaking further into the NIR. Only subtle differences in relative peak heights are seen in comparing transient spectra obtained with PTAK-60 to 20:80 CPEC. By contrast, 60:40 and 80:20 CPECs (Figures 6.2c and 6.2d) exhibit distinctly different transient spectral shapes and evolution: the signature of charge separated polaron and polar-pair species are no longer present, but rather an absorbance centered further into the NIR (>1150 nm and is consistent with the singlet exciton absorption of polythiophenes) now dominates the transient spectrum. For these, the PTAK GSB signature is slightly blue-shifted by ≈ 10 nm but

still exhibits evidence of an underlying vibronic progression and a band due to stimulated emission (SE) is now visible around 650 nm. At the longest pump-probe delays examined, the broad spectrum of the triplet exciton centered at 900 nm appears for 80:20 CPEC and persists onto a nanosecond timescale.

These results illustrate the effect that PFPI CPEs have on disrupting the intermolecular ordering of PTAK strands in solution. This alteration to PTAK stacking behavior impedes the formation of charge-separated species associated with H-aggregate formation amongst conjugated thiophene domains. Rather, steady state emission indicates that these are replaced by J-aggregates upon mixing with PFPI. Previous comparisons made between the photoluminescence spectra of pure PTAKs and CPECs of varying proportions consistently reflect an increase in the 0-0/0-1 ratio of vibronic peak intensities with added PFPI⁷, suggesting the disruption of H- in favor of J-aggregates.⁸ The spectra from Figure 6.2 then indicate that J-aggregate domains favor population of singlet excitons over polaron formation potentially by destabilizing the latter. Figure 6.2e plots decay traces of an integrated region from the NIR singlet absorption to show the differences in kinetics between pure PTAK and each CPEC. Significantly longer lifetimes are observed for the predominantly J-aggregate domains found in 60:40 and 80:20 CPECs (≈ 15 and 30 ps) compared to the H-aggregate domains of PTAK-60 and 20:80 CPEC (both approximately 6 ps). These spectra provide a frame of reference for comparison to transient spectra observed following preferential excitation of PFPI within these complexes and illustrate what spectral and kinetic effects can be expected following EET.

Correspondingly, Figure 6.3 displays TA spectra collected for pure PTAK

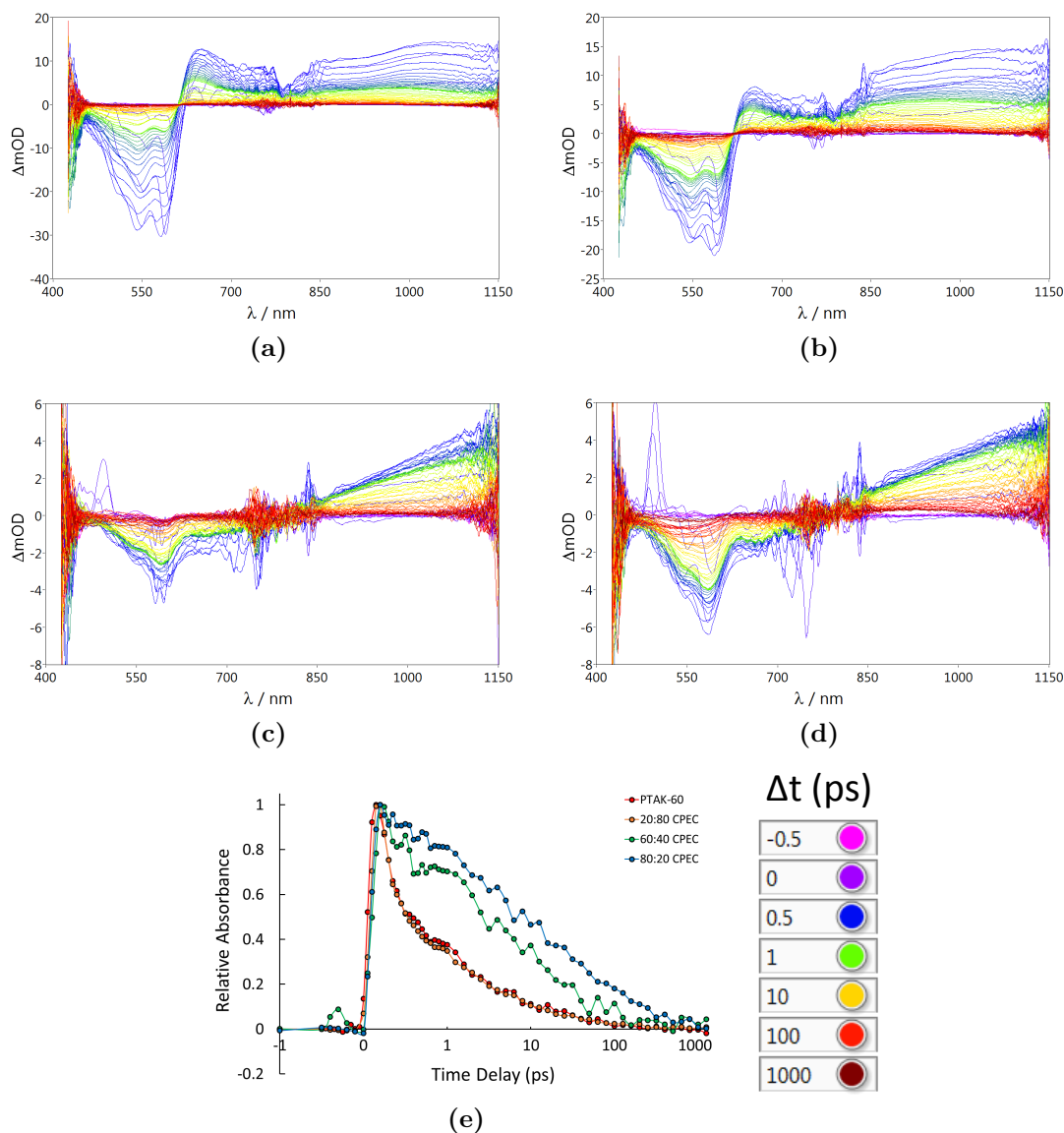


Figure 6.2: 600 nm Transient Absorption of CPECs and Integrated Traces: (a) PTAK-60, (b) CPEC 20:80, (c) CPEC 60:40, (d) CPEC 80:20, and (e) decay traces of PTAK and CPEC NIR integrated over 850-1100 nm

(6.3a) and various PTAK-heavy CPEC compositions (6.3b, 6.3c, and 6.3d), following low fluence excitation at 360 nm. The pure PTAK sample (6.3a) exhibits features similar to those seen for 600 nm excitation but with delayed and prolonged kinetics, namely a several hundred fs induction to the coupled transient signals with decay lifetimes that are approximately 50% longer. Comparisons of pure PTAK to 20:80 CPEC

(6.3b) show few noteworthy differences, with the GSB (blue) shifting to slightly lower wavelengths and the visible TA band decreasing in intensity. As the absolute PTAK absorption dominates the PFPI absorption at 360 nm in the 20:80 composition, these differences should arise principally from disruption of the PTAK H-aggregate domains rather than photophysics induced by direct interaction with or energy transfer from photoexcited PFPI. While the influence of the latter cannot be entirely ruled out, the observed changes in PTAK photophysics are comparable to direct PTAK excitation (600 nm) of PTAK-60 and 20:80 CPEC (Figures 6.2a and 6.2b), indicating that the initial disruption of H-aggregation is mostly responsible rather than EET for the observed differences or PFPI based signals. A weak, broad, and long-lived feature appearing around 900 nm also persists onto relatively long timescales, eventually becoming a very prominent feature within the transient spectra of 40:60 (6.3c). Comparatively, the absolute spectrum of the 40:60 mixture is characterized by relatively intense infrared (IR) signatures and a smaller, unstructured PTAK GSB, though the former is likely due to discrepancies in collection conditions and scaling the visible to near-IR (NIR) regions. 60:40 CPEC (6.3d) shows spectral shapes largely similar to 40:60 but with the same relative intensities between the NIR absorption and GSB as were seen in 20:80, suggesting the disagreement by 40:60 CPEC to be an acquisition anomaly.

Similarly, Figure 6.4 presents TA spectra corresponding to low fluence, 360 nm excitation of PFPI-40 and CPEC 80:20 (6.4a and 6.4b). The TA progression shown in Figure 6.4a reflects the dynamics of pure PFPI, namely a GSB below 500 nm, S_1 sharp TA absorptive feature and shoulder at 725 and 550 nm, and significantly weaker

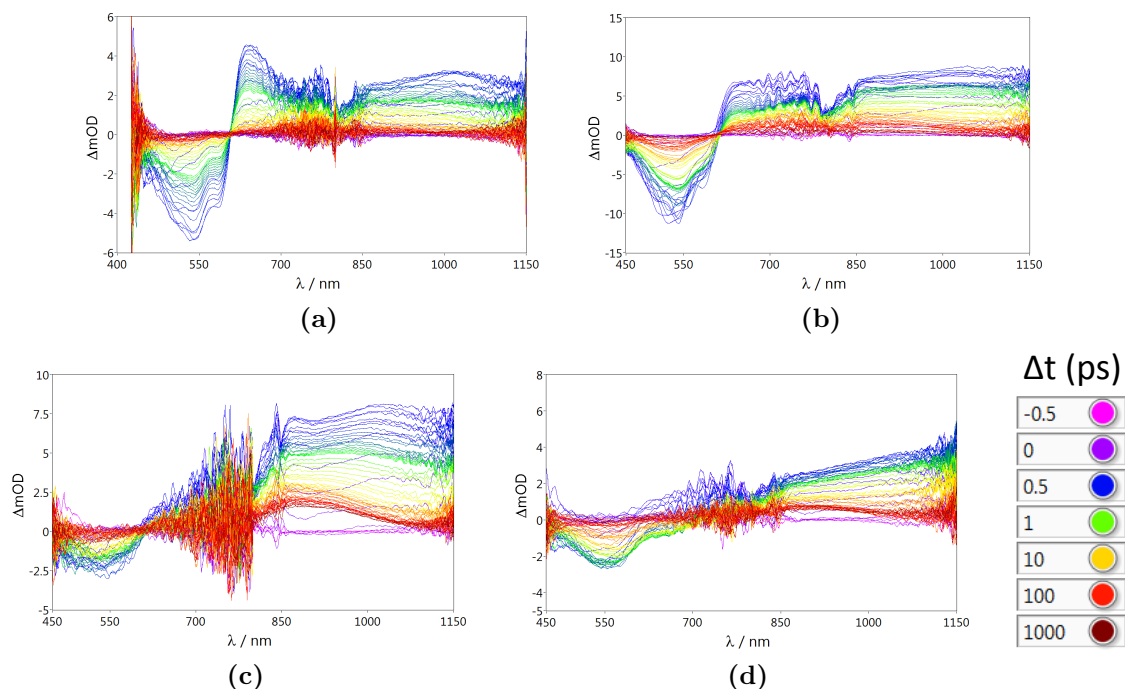


Figure 6.3: 360 nm Transient Absorption of PTAK and PTAK-dominant CPECs: (a) PTAK-60, (b) CPEC 20:80, (c) CPEC 40:60, and (d) CPEC 60:40

and relatively unstructured broadband absorption across the NIR. With PFPI having a nine-fold higher relative cross section than PTAK in the 60:40 complex (6.3d), this is the first sample in which these PFPI excited state transients are barely discernible, if only as a narrow, slight absorption at early times around 750 nm and positive shoulder at intermediate times near 650 nm. Interestingly, despite strong favorability for excitation of PFPI over PTAK in 60:40 CPEC, PFPI singlet signatures do not dominate the overall transient spectrum indicating that PFPI transients are quenched very rapidly, probably as a result of PFPI to PTAK EET or rapid internal conversion and non-radiative relaxation of PFPI transients adjacent to PTAK CPEs. Upon increasing the PFPI:PTAK ratio of the CPEC to 80:20, the PFPI transient features dominate the resulting TA spectra as seen in Figure 6.4b. The PTAK GSB (500-600 nm) and S_1 NIR absorption (>850 nm) remains prevalent and persists

for approximately the same timescale as observed in the PTAK dominated samples. Other less intense regions of the PTAK absorptive features are likely present as well but are obscured by stronger PFPI absorptions. The NIR absorption of PTAK singlet at the high wavelength (red) edge of the spectrum dominates until later times (100s of ps), at which point the signal decays and now resembles PFPI with the long lived feature seen in the other CPECs (40:60 and 60:40) slightly above 900 nm. This long-lived signal in the NIR also seems more intense here than it was for 60:40 and relaxes more rapidly at the end of the one nanosecond time window explored here.

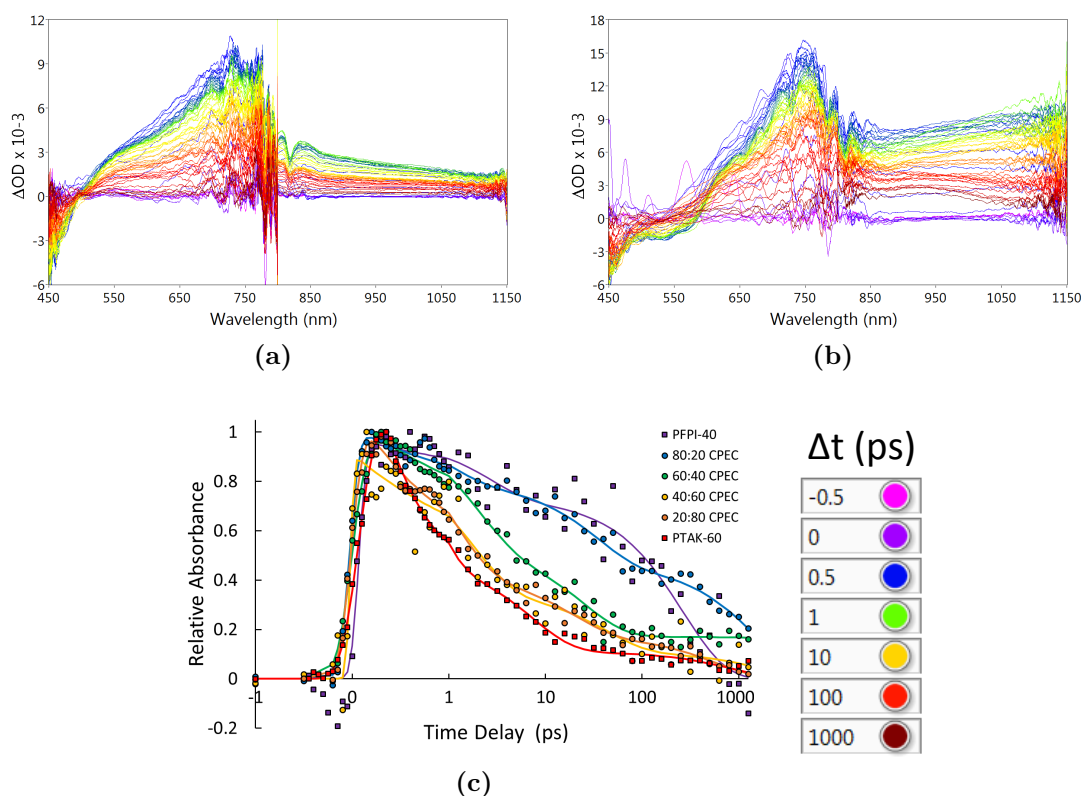


Figure 6.4: 360 nm Transient Absorption of PFPI and CPEC 80:20 and Integrated Traces (a) PFPI-40, (b) CPEC 80:20, and (c) decay traces of PTAK, CPEC, and PFPI NIR integrated over 850-1100 nm

Direct comparison of these spectra reveals several features that evidence EET. Firstly, if no EET occurred between PFPI and PTAK, one might expect the PTAK

bleach signal to decrease according to what a number density argument would suggest, i.e. as the higher absorption cross section PFPI absorbs 38, 77, 90, and 96% of excitation fluence for 20:80 through 80:20 respectively, the intensity of the PTAK GSB signature should decrease markedly as fewer thiophene domains are directly excited. However, this pronounced drop-off in bleach signal is not seen, indicating that thiophene transients are prepared by means other than direct excitation, namely EET from excited PFPI. The timescale for the recovery of the PTAK bleach also lengthens, although this may not be strictly attributed to EET and could rather be linked to the disruption of H-aggregate thiophene domains (seen in the shifting of the bleach spectrum) as a result of coupling between CPEs. Additionally, the long lived species absorbing at 900 nm is most prevalent in 40:60 through 80:20 (slightly in 20:80) is likely a sign of T_1 absorption following triplet formation on the PTAK as the feature is located where a conjugated thiophene triplet has been observed in poly-3-hexylthiophene (P3HT) films.⁹ As this feature is only seen for aggregated films of regiorandom (RRa-) rather than regioregular (RR-)P3HT (in which intermolecular order facilitates H-aggregate formation) the absence of this supposed triplet from spectra of H-aggregated thiophene domains in predominantly PTAK based CPECs (and pure PTAK) is likely the result of such ordering and a plausible explanation.¹⁰

We can further validate EET from PFPI to PTAK and extract some details on EET kinetics through quantitative comparisons of a weighted contribution of PFPI-only (360 nm) and PTAK-only (600 nm) transients to mixed CPEC data collected at 360 nm. A weighted combination of the first two spectral progressions reflect what can be expected if no EET occurs, (barring energy dependence of PTAK excitation seen

to be minimal by the similarities exhibited by Figures 6.2a and 6.3a) where spectral transients should only reflect the fraction of each component excited at 360 nm. The PTAK-only data was collected via photoexcitation of the 80:20 CPEC at very low fluence 600 nm excitation to be resonant only with PTAK and elicit kinetic evidence of the production of PTAK transients following photoexcitation in a CPEC environment. Although we are unable to show that 360 and 600 nm excitation of the PTAK phase in this CPEC have strictly identical transient spectral behaviors, they are similar given that Figures (6.2a and 6.3a show markedly similar photoresponses to excitation of pure PTAK at either wavelength.

Figure 6.5 shows spectral waterfall plots (6.5a and 6.5b) and kinetic traces (6.5c) resulting from this analysis. Comparison of pure PFPI (Figure 6.4a) to a system in which PFPI is the predominant species, 80:20 CPEC (Figure 6.4b), reveals a prominent difference in the NIR portion of the TA spectra. Specifically, much more of the 80:20 CPEC NIR signal is seen along the red edge of the spectrum (>1100 nm), eventually decaying to reveal the long-lived PTAK triplet underneath. If it is assumed that the isolated PFPI signatures do not shift in response to the presence of PTAK (i.e. the presence of PTAK does not disrupt PFPI transient structures leading to an energetic shifting of this broad absorptive feature), then a weighted subtraction can be performed to remove the pure PFPI component from the 80:20 CPEC TA spectra. The pure PFPI was weighted such that the peak intensity of its primary absorptive feature at 725 nm was identical in intensity to the equivalent band from 80:20 CPEC, to account for differences in pump fluence, sample composition, relative absorptivity, and other experimental conditions between measurements. This relative subtraction

yielded the set of spectra shown in Figure 6.5a and can be compared directly to PTAK transients collected from 600 nm excitation of 80:20 CPEC in Figure 6.5a (similar to Figure 6.2d but collected at a slightly lower fluence).

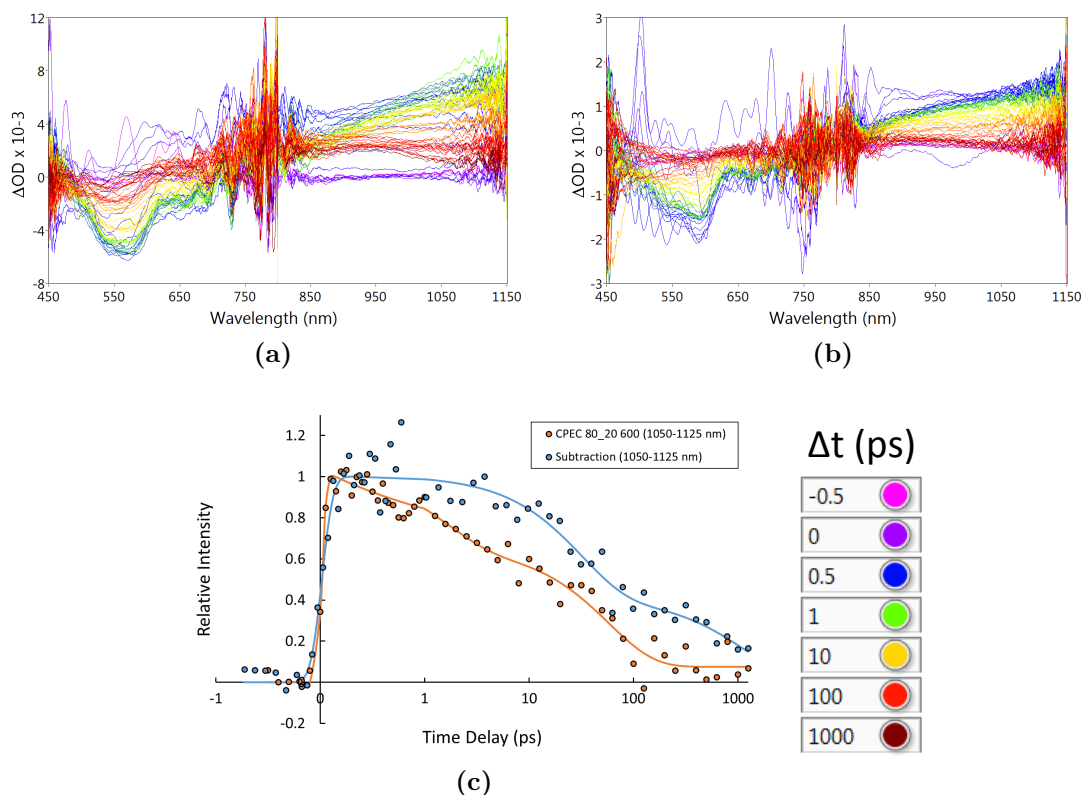


Figure 6.5: PFPI Subtraction and Energy Transfer Isolation from TA: (a) CPEC 80:20 – PFPI-40 (weighted), (b) CPEC 80:20 TA (600 nm excitation), and (c) integrated Kinetic Traces (1050-1125 nm)

Both spectra contain an absorption band further into the NIR at >1150 nm (the PTAK S_1) accompanied by PTAK GSB and SE at 560 and 650 nm, respectively. The PTAK T_1 absorption subsequently grows in over the course of 100s of picoseconds in Figure 6.5a, though not appreciably in Figure 6.5b. If EET did not occur, this subtraction should reveal the same spectral profile and kinetics obtained by directly exciting the 80:20 CPEC with an excitation wavelength solely resonant with the PTAK component. The weighted subtraction spectrum does contain highly similar

features but also evidences a slower decay along the red-edge of the NIR (>1100 nm) seen via direct excitation. Decay traces obtained by integrating each transient spectrum from 1050 to 1125 nm are shown in Figure 6.5c and the data elicited from the subtraction analysis clearly exhibits a pronounced increase in singlet decay lifetimes. While the long-lived triplet species centered around 900 nm does overlap the integrated region of interest, the state has not yet been populated at early delays and cannot account for the entire difference between the traces at longer delays. To obtain a quantitative handle on the differences seen between the kinetics of each of these, the transient cuts were fit with a non-linear regression function comprised of a bi-exponential and constant offset convoluted with a Gaussian instrument response to obtain the fitting parameters listed in Table 6.1.

Parameter	Subtraction	CPEC 80:20 600
A_1	0.594	0.371
τ_1 (ps)	31.4	1.56
A_2	0.387	0.557
τ_2 (ps)	1126	58.2
A_3	0.019	0.072

Table 6.1: CPEC Subtraction Decay Trace Fitting Parameters

The net increase in both decay lifetimes by over an order of magnitude when the sample is primarily excited at a higher excitation frequency indicates that EET plays a definitive role in generating PTAK singlet excited state transients. Comparable TA analysis of non-polyelectrolyte polythiophene (e.g. RR-P3HT) excited at different pump frequencies shows moderate alterations to charge transfer yields with changes in excitation frequency;¹¹ however, they do not show such drastic differences in exciton decay timescales, suggesting that energy dependence of direct

PTAK excitation cannot explain the different timescales observed when exciting each CPEC.¹⁰ Inspection of NIR region in Figures 6.2a and 6.3a reveals significant evidence to validate this assertion. The immediate decrease of the direct excitation trace relative to the subtracted trace ($\approx 15\%$ by 1 ps) indicates that EET can occur on a sub-picosecond timescale following population of the PFPI excited state to maintain and repopulate these initially relaxed PTAK transients states over comparable lifetimes. These timescales also persist longer than those obtained by a similar analysis of pure PFPI excitation from Figure 6.4a (and shown in Figure 6.4c), which decays bi-exponentially with lifetimes of 2.6 and 270 ps. As the PFPI excited state lifetime is substantially longer than that of the directly excited PTAK singlet exciton (50-80 ps), the similarity in lifetimes provides direct evidence of continuous, gradual population of the PTAK by PFPI throughout the latter's singlet decay lifetime. Slight overlap of the T_1 absorbance is a primary factor in elevating the longest lifetime seen for 360 nm excitation of the CPEC, though this contribution is assumed to be minimal. Succinctly, this analysis stands as strong evidence for the instantaneous and prolonged population of PTAK excited state as a result of PFPI lifetime limited EET.

6.5 Conclusions

Ultrafast TA spectroscopy yielded several insights into the structural and photophysical characteristics of polyelectrolyte complexes and their components. The disruption of H-aggregation domains in PTAK upon addition of PFPI was validated in observing the formation of singlet excitons and triplets rather than charged po-

larons and polaron pairs as well as the resulting prolonged kinetics associated with these transients. It was shown that PFPI serves as a donor for ultrafast energy transfer to PTAK at several different mixed ratios. Specifically, a rigorous analysis to remove the contributions of PFPI from the transient spectra of 80:20 CPEC and compare the resulting spectra to direct excitation of the PTAK within the CPEC highlighted differences in PTAK signature behavior between direct excitation and when it is populated through EET. Comparison of subtracted spectra decay traces and relaxation timescales relative to direct PTAK excitation indicates energy transfer from PFPI to PTAK throughout the PFPI excited state lifetime. Additional analysis illustrates how the dynamics of the transient signatures are affected by shifting the excitation frequency and PFPI:PTAK ratio. Ongoing work will look into preparations at different intermediate weight percentages to determine what the ideal conditions for EET within this system.

6.6 Acknowledgments

Professor Alex Ayzner and his research group at the University of California, Santa Cruz (UCSC), particularly his student William Hollingsworth, designed, synthesized, and prepared the supramolecular assemblies of interest. They handled the steady state analysis and preliminary examination of photoluminescence patterns of these samples. The ultrafast work was accomplished by our group in collaboration with our postdoctoral researcher, Jamie Young.

References

1. Croce, R. and van Amerongen, H. *Nat Chem Biol* **10**(7), 492–501 (2014).
2. McConnell, I., Li, G., and Brudvig, G. W. *Chemistry & Biology* **17**(5), 434–447 (2010).
3. Costa, T., Garner, L. E., Knaapila, M., Thomas, A. W., Rogers, S. E., Bazan, G. C., and Burrows, H. D. *Langmuir* **29**(32), 10047–10058 (2013).
4. Knaapila, M., Evans, R. C., Garamus, V. M., Almásy, L., Székely, N. K., Gutacker, A., Scherf, U., and Burrows, H. D. *Langmuir* **26**(19), 15634–15643 (2010).
5. Evans, R. C., Knaapila, M., Willis-Fox, N., Kraft, M., Terry, A., Burrows, H. D., and Scherf, U. *Langmuir* **28**(33), 12348–12356 (2012).
6. Ardoña, H. A. M. and Tovar, J. D. *Chem. Sci.* **6**(2), 1474–1484 (2015).
7. Hollingsworth, W. R., Segura, C., Balderrama, J., Lopez, N., Schleissner, P., and Ayzner, A. L. *J. Phys. Chem. B* **120**(31), 7767–7774 (2016).
8. Spano, F. C. and Silva, C. *Annu. Rev. Phys. Chem.* **65**(1), 477–500 (2014).
9. Guo, J., Ohkita, H., Bente, H., and Ito, S. *J. Am. Chem. Soc.* **132**(17), 6154–6164 (2010).
10. Guo, J., Ohkita, H., Bente, H., and Ito, S. *J. Am. Chem. Soc.* **131**(46), 16869–16880 (2009).
11. Herrmann, D., Niesar, S., Scharsich, C., Köhler, A., Stutzmann, M., and Riedle, E. *J. Am. Chem. Soc.* **133**(45), 18220–18233 (2011).

Chapter 7

Electronic Relaxation Dynamics of 9,10-bis(phenylethynyl)anthracene Studied with Ultrafast Broadband Polarization Anisotropy

7.1 Abstract

Data acquisition methodology was developed for measuring broadband polarization anisotropy (BPA) via transient absorption (TA) spectroscopy through alternating sampling of broadband probe spectra collected at different polarization orientations relative to a fixed excitation source. The dynamics of 9,10-bis-phenylethynylanthracene (BPEA) was interrogated to establish the viability of the experimental set-up. Findings for solution-phase and nanoaggregated BPEA elaborate on previously established understandings of BPEA's excited transient states, transition dipole orientation, and excitation-dependent relaxation dynamics prevalent within the system. Consideration of solution phase BPEA provided insight into the rotational lifetime (≈ 170 ps) while aggregates yielded information about the extent of and timescales associated with crystalline phase energy migration. Observed anisotropic values were considered

relative to previous reports.

7.2 Introduction

Ultrafast spectroscopies have become valuable probes of photochemical and photophysical processes, as evidenced by the ever expanding repertoire of techniques that have been developed to interrogate chemical and material systems. Advances in optical equipment, understanding of the involved materials, and the theory behind transient state behavior permits the extension of procedures often applied to steady state or slower transients into the ultrafast domain.

A natural augmentation of broadband transient absorption (TA) measurements is the simultaneous measurement of electronic transition polarization; we refer to the combination of these measurements collected on an ultrafast time domain as transient polarization anisotropy (TPA). TPA occurs when the photoresponses of spectral transitions induced by directional, polarized excitation of a molecular system vary when probed along cardinal polarization axes. An anisotropic transition polarization created via photoexcitation generally relaxes towards isotropy when constituent molecules are free to rotate, e.g. gas phase or individual molecules dissolved in solution, or when the excitations transfer to other sites or moieties in condensed-phase materials. The memory of the initially induced polarization anisotropy typically diminishes with time from these factors over a picosecond-to-microsecond timescale. Thus, by tracking the change in TPA with time, additional details about the photodynamics and kinetics behind molecular rotation, exciton localization, or transient

migration can be obtained for the material. Ultrafast dynamics between electronic states may also lead to dramatic changes in transition anisotropy quickly after excitation.

TPA measurements have been used extensively to characterize rotational lifetimes of molecular excited states by fluorescence and single-wavelength transient absorption detection methods.^{1,2} The relatively novel approach taken here is one in which samples can be interrogated over a span of wavelengths simultaneously to facilitate comparisons between transients. Traditionally, polarization anisotropy is eliminated from a sample consisting of randomly oriented molecules or molecular units in a 3D interaction volume by fixing the polarization of the probe at an angle 54.7° away from the vector of the incident photo-excitation pulse polarization (as described in Section 1.2.3). The unique methodology utilized here (Section 2.4) avoids errors imposed by batch collection of each polarization by alternating which probe polarization is sampled over consecutive shots throughout a polarization resolved TA measurement. Broadband polarization anisotropy (BPA) measurements have been conducted previously, though not over a sizable range corresponding to wavelengths that probe electronic transitions.^{3,4}

9,10-bis-phenylethynylantracene (BPEA) serves as an ideal test molecule for this experiment as the lowest lying electronic excitations have perpendicular transition dipole moments that can be selectively photoexcited using different excitation frequencies. Figure 7.1a shows the molecular structure of the compound with arrows overlaid to indicate the dipole vectors of the ethynyl bridge (blue) and anthracene (purple) -like chromophores. The structure and spectra shown in Figure 7.1b depict

the directionality of the transition dipoles to each higher lying singlet state and how these excitations relate to the dipole vectors shown for Figure 7.1a. The strongest transition dipoles are aligned along the ethynyl bridge chromophore for the lowest lying transition, S_1 , and the orthogonal anthracene moiety, for the next transition to S_5 in Figure 7.1a (later identified by density functional theory (DFT) calculations to be S_4). The net UV-Vis spectrum of solution phase BPEA with highlighted regions of Franck-Condon overlap to these chromophores is shown as Figure 7.1c. Based on this, the S_1 and S_4 transitions are primarily photoexcited when using 400 (blue) and 266 nm (purple) excitation wavelengths, respectively.

Following Kasha’s Rule, excitation of the molecule to this higher lying state leads to a rapid relaxation (within a ps) back to the S_1 which will persist for a comparatively long time. However, since the direct and indirect population of S_1 occur from different directionalities relative to the resulting S_1 polarization (parallel and perpendicular respectively), the resulting polarization anisotropies are encoded with opposite signs. As illustrated in previous studies⁵ fluorescence measured from S_1 following photoexcitation yields anisotropies of approximately -0.2 and 0.35 for 266 and 400 nm excitation respectively.

In addition to isolated molecules, various types of BPEA crystal aggregates can be manufactured⁶ with potential applications as oligomeric molecular switches.⁷ Absorption spectra of BPEA compared to these crystal aggregates are included as Figure 7.2a. Specifically, the absorption shown by the green trace corresponds to nanocrystals (NCs) reprecipitated from acetone into water⁸, by a procedure similar to that seen in for poly-3-hexylthiophene (P3HT) nanoparticles considered in Chap-

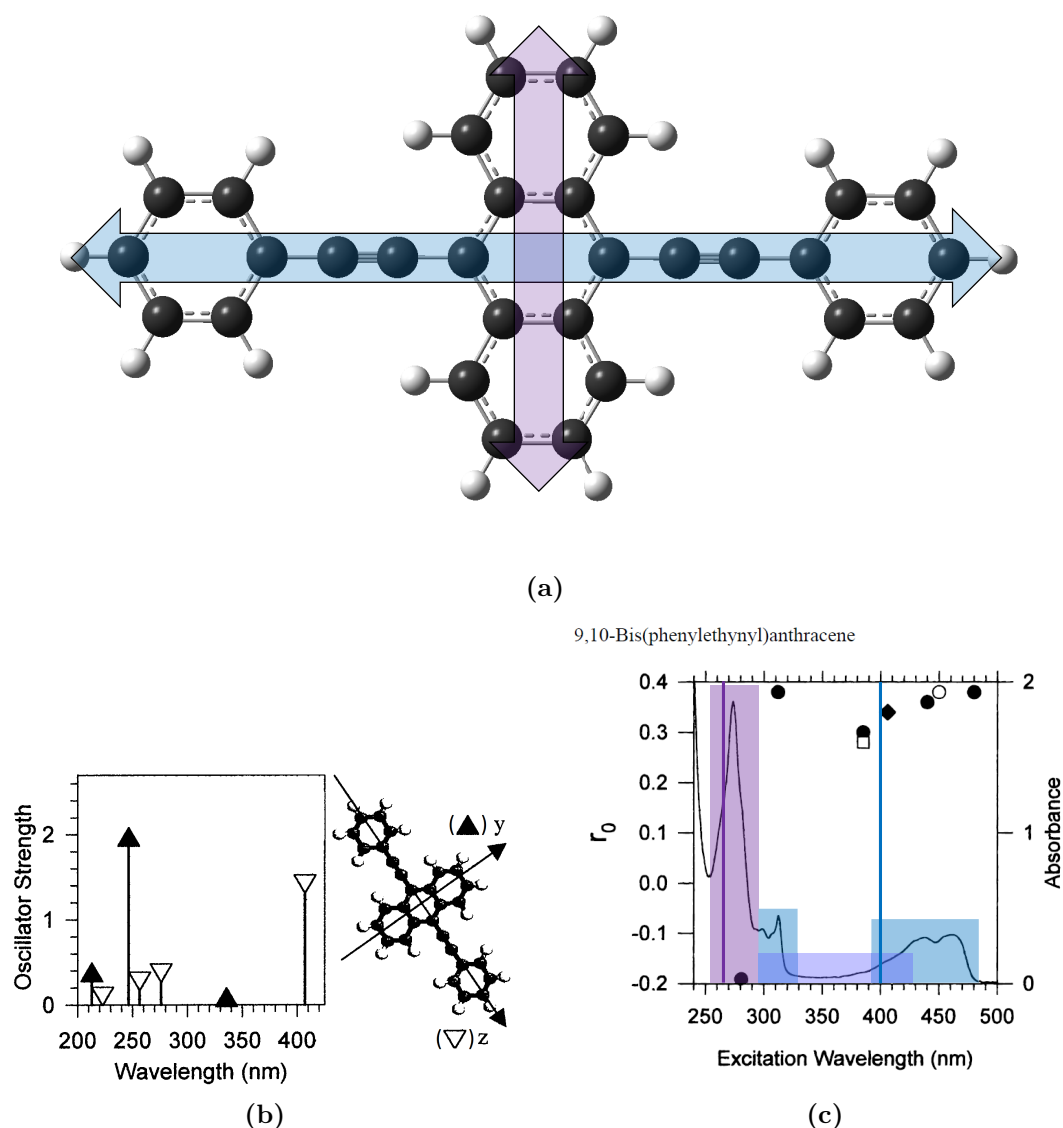


Figure 7.1: BPEA Molecule, Transition Dipoles and UV-Vis Spectra: (a) 9,10-bis-phenylethynylanthracene (BPEA) with vectors corresponding to ethynyl bridge (blue) and anthracene (purple) -like chromophores, (b) open downward and closed upward triangles indicate transition dipoles aligned along the z- and y-axis respectively⁵, and (c) experimental UV-Vis spectrum with colorations to describe regions of excitation along each chromophore and vertical lines to show 266 (purple) and 400 nm (blue) excitation⁵

ter 3.⁹ A transmission electron microscope (TEM) reference image of NCs prepared by this methodology is shown as Figure 7.2b. BPEA NCs have been previously shown to engage in energy transfer from peripheral to internal states on a nanosecond timescale,

resulting in the change of relative populations of different fluorophore populations.⁶ These energy transfer interactions should be reflected in measurements of electronic TPA as the transient state dipoles will rotate towards an isotropic distribution following prolonged energy migration. Though it would likely be difficult to tease out energy transfer kinetics from the degree of rotation entailed with each energy transfer event, BPEA NCs can serve to clarify the energy transfer of these specific aggregates and highlight the ability of this experimental methodology to interrogate aggregated or assembled molecular materials.

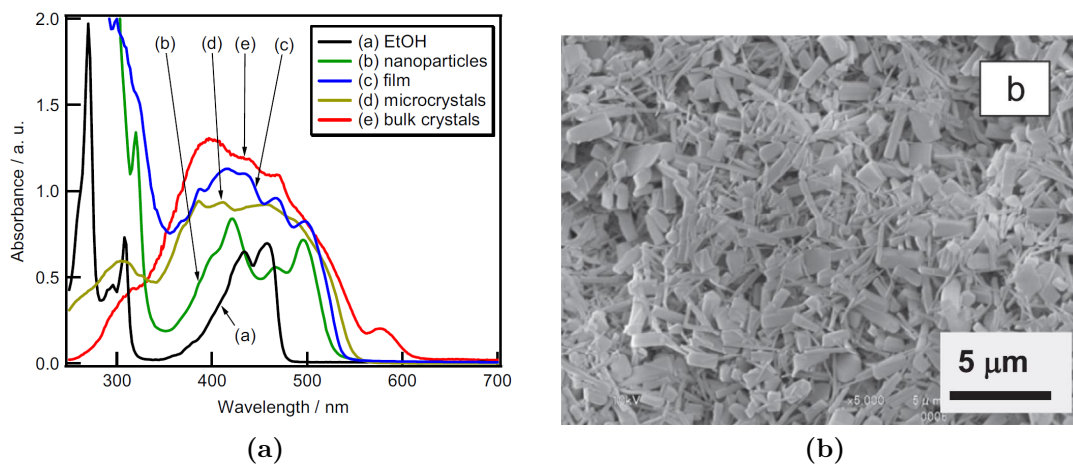


Figure 7.2: Molecular Orbitals for Electronic Excitations of BPEA Ground State: (a) electronic absorption of BPEA in solution (black) and various aggregates, especially nanoparticles (green)⁶ and (b) TEM image of BPEA reprecipitated nanoparticles^{6,8}

7.3 Experimental Methods

A 0.05 mg/mL solution of BPEA in cyclohexane (CH) was prepared for ultra-fast experiments; BPEA was obtained from Sigma Aldrich and used as is. BPEA NCs were formed by reprecipitation as detailed in Section 2.1, by rapidly injecting

0.500 mL of 0.5 mg/mL BPEA solution in acetone into 5 mL of H₂O and using compressed air to remove residual acetone from the sample.

Broadband polarization anisotropy (BPA) measurements were executed using the methodology laid out in Section 2.4. 400 nm and 266 nm pulses obtained through second harmonic generation (SHG) and subsequent sum frequency generation (SFG) were used as excitation wavelengths for BPEA in solution. BPEA nanocrystals were evaluated using excitation wavelengths of 400 and 500 nm, though these were not selected for with rigorous reasoning. These measurements were conducted by collecting pairs of parallel (\parallel) and perpendicular (\perp) spectra though subsequent collection of magic angle (MA) and \perp spectra provided similar results. Further discussion of the experimentation is omitted from here, but polarizers were included immediately following the neutral density filter used to split the white light probe to not impact the relative intensities of each polarization.¹⁰

7.4 Results and Discussion

Density functional theory (DFT) calculations were run using Gaussian 09 in order to clarify which molecular orbitals of BPEA are associated with transitions excited experimentally. Orbitals associated with two sets of occupied BPEA ground state and unoccupied excited states that correspond to 400 and 266 nm excitation are shown in Figure 7.3. Figure 7.3a depicts that the transition dipole of the lowest lying singlet transition, S₁, and the directionality of the dipole formed by the overlap of the two, which lies along the length of the longest conjugated segment (i.e.

spanning both phenyl, both ethynyl, and the short axis of the anthracene moieties). Figure 7.3b illustrates that the next significant transition (S₄, to the LUMO+3 orbital). This transition involves a linear combination of several sets of molecular orbital excitations: two minor components lie along the same axis as the S₀-S₁ transition, while the two major components involve changes in dipole moment along the long axis of the anthracene moiety (i.e. perpendicular to the lower energy excitation). This comparison is consistent with a previous report that showed that excitation and subsequent relaxation of this excited state to the S₁ state should result in an inverted anisotropic response relative to direct excitation of the S₁ state.⁵

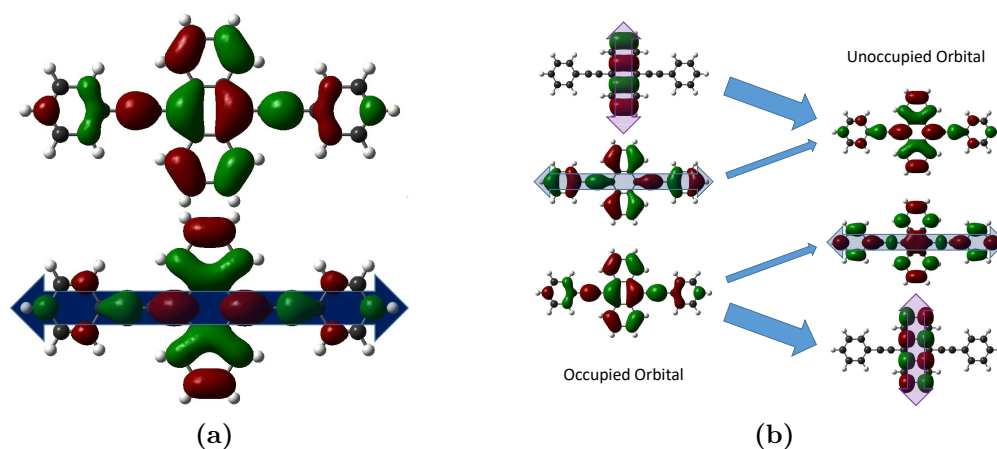


Figure 7.3: Molecular Orbitals for Electronic Excitations of BPEA Ground State: (a) S₁ and (b) S₄ excitation of BPEA

7.4.1 BPA on Solution Phase BPEA

TA spectra collected at each of these excitation wavelengths to be selectively excite the S₁ and S₄ electronic states were monitored at parallel and perpendicular probe polarizations relative to excitation and are presented as plots (a-d) in Figure 7.4. Figures 7.4a and 7.4b show the TA collected by exciting BPEA using 400 nm

excitation in parallel and perpendicular geometries of probe polarization, respectively. As these spectra were collected simultaneously and handled using the exact same data handling procedures, i.e. identical smoothing conditions and application of the parallel chirp correction to both, no further scaling or alteration of the spectra should be necessary for direct comparison. During the first 100 ps following excitation the parallel spectrum is noticeably more intense than the corresponding perpendicular spectrum, while at later delays the spectra are almost identical. This stems from the ability of the ensemble of excited molecules to rotationally diffuse in solution ultimately generating a less anisotropic or completely isotropic distribution of excited state transition dipoles. Figure 7.4e shows the corresponding BPA or $r(t, \lambda)$ spectrum determined by comparison of these intensities at each time and wavelength using equations derived from Equation 1.2c. At wavelengths along the blue edge of the visible band and the red edge of the NIR absorption, the initial anisotropy plateaus at 0.4 before relaxing on a timescale of about 170 ps. This exemplifies the ability of the experimental set-up to accurately and quantitatively determine polarizations across a broadband range of probe wavelengths simultaneously.

Figures 7.4c and 7.4d show the same analysis conducted for excitation of the same sample at 266 nm. For delays > 200 fs the transient spectra are incredibly similar to those collected with 400 nm excitation. This provides substantial evidence of a rapid, ultrafast relaxation of the higher lying singlet state(s) to S_1 . At this excitation wavelength the relative magnitude of the parallel and perpendicular spectra is reversed with the perpendicular spectrum being more intense for most of the first few hundred ps (Figure 7.4e). This rapid change in transition dipole moment can be

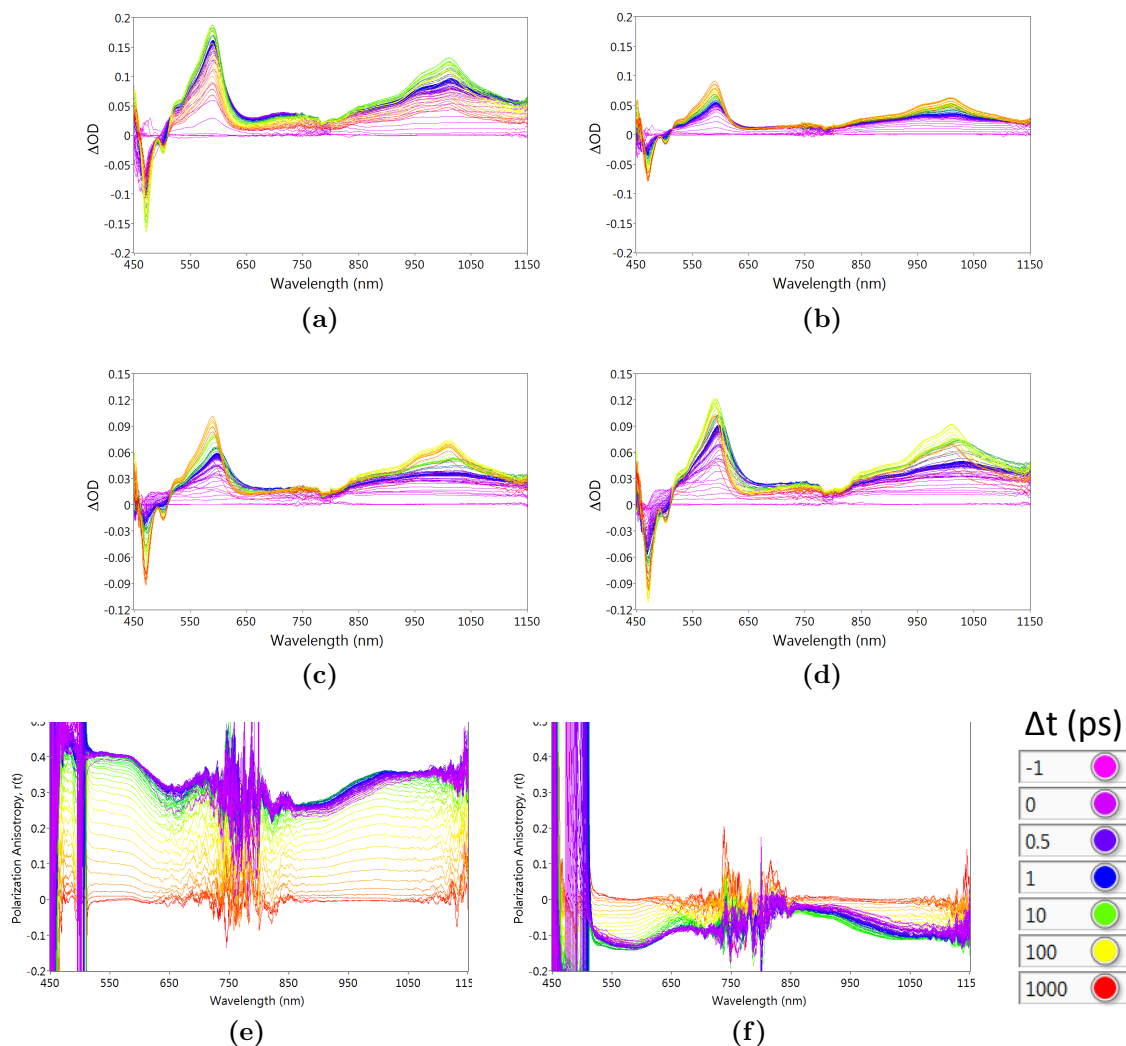


Figure 7.4: BPEA Parallel and Perpendicular TA and BPA Spectra: Parallel, perpendicular, and magic angle spectra for 400 nm (a, b, and e) and 266 nm (c, d, and f) excitation

attributed to population of the S_1 state by ultrafast relaxation from the higher-lying excited state rather than direct population by photoexcitation at 400 nm.

Different portions of the electronic excitation spectrum exhibit discrepancies in polarization anisotropies despite similarities in kinetic traces across the entire probe spectrum. Figure 7.5 plots traces from four integrated regions of the BPA spectra that each roughly correspond to an overlap of ground state bleach (GSB) and stim-

ulated emission (SE) (475 nm), discrete TA bands from S_1 (590 and 1100 nm) and a broadband absorption covering much of the visible-NIR region (~ 600 -1000 nm). The solid and dashed lines indicate the anisotropy traces of these regions from 400 and 266 nm excitation, respectively. Table 7.1 lists parameters obtained by fitting these traces using a single (S_1) or bi-exponential (one rise and one decay, S_4) function to model the change in anisotropy as a function of time. Direct excitation of the S_1 yields consistent rotational lifetimes between 170-184 ps regardless of the wavelength regime selected, which is sensible for this molecule and solvent given previous studies of the rotational lifetimes of similar sized molecules.² The rotational lifetimes determined for S_4 excitation with subsequent relaxation to S_1 are more varied and slightly lower overall, with the anticipated most accurate value of 92 ps, but are still reasonably close to those predicted from 400 nm excitation. This slight decrease in lifetime may be attributable to additional vibrational energy deposited into the solvent within the immediate vicinity of the photoexcitation in response to absorption of a 266 nm photon and subsequent relaxation to S_1 compared to direct excitation to the S_1 manifold with a photon containing only $\frac{2}{3}$ the energy. This would thereby provide slightly more flexibility for the molecule to rotate more quickly if more vibrational energy had been transferred into adjacent solvent molecules.

Some differences in the average anisotropies associated with different spectral regions are apparent (Figures 7.4e, 7.4f, and 7.5 and Table 7.1), which are due to a few factors. An initial, important consideration is that the overlap of features characterized by (even slightly) different anisotropies will skew net anisotropies based on Equation 1.2d, particularly when the signal intensities are opposite in sign.¹¹

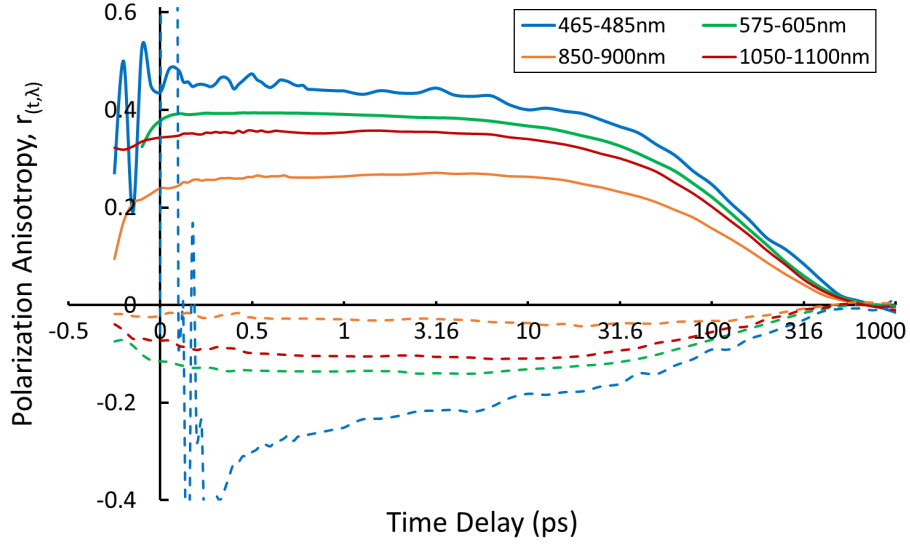


Figure 7.5: Kinetic Traces of BPA Measurements on BPEA: traces of integrated cuts, over regions indicated in key, from BPA measured. These bands represent different BPA signatures with solid and dashed lines corresponding to 400 and 266 nm excitation respectively.

400 nm	465-485 nm	575-605 nm	850-900 nm	1050-1100 nm
$r_{(t,\lambda),0}$	0.446	0.392	0.269	0.358
τ_{rot} (ps)	170	171	184	173
266 nm	465-485 nm	575-605 nm	850-900 nm	1050-1100 nm
$r_{(t,\lambda),S_4 \rightarrow S_1}$	0.028	0.276	0.026	0.035
τ_{rel} (ps)	0.24	0.13	11.0	0.71
$r_{(t,\lambda),0}$	-0.140	-0.248	-0.050	-0.114
τ_{rot} (ps)	151	92	188	145

Table 7.1: BPEA Anisotropy Range Fit Parameters

Anisotropies of overlapping features are often skewed to more extreme values as the net TA intensity approaches zero, as can be seen in the GSB/SE region of Figure 7.4e at wavelengths below 480 nm. This illustrates a limitation of polarized measurements in general, in that features of interest must either be isolated spectrally or capable of being modeled in a selected wavelength regime for the technique to be viable. This is evident by comparing the GSB and visible TA features with maximum anisotropies

of 0.45 and 0.39 respectively, compared to only 0.36 for the peak in the NIR. The first two features overlap one another, canceling out signal intensity while encoding slightly different anisotropies that elevates their net values above the NIR's measured anisotropy which is the closest to the anticipated value for 400 nm photoexcitation.⁵

Interestingly, a noticeably lower initial anisotropy is observed between 600 and 1000 nm in both BPA spectra (Figures 7.4e and 7.4f). This region is sufficiently isolated from either of the other peaks and exhibits a maximum anisotropy of only 0.27 from 400 nm excitation, significantly lower than either peak. This result suggests that BPA measurements are also susceptible to the dipole moment between the probed transient state and a higher lying resonant electronic state indicated by the involved TA signal. If BPA was only sensitive to the dipole moment between the polarized excitation of a subpopulation of the isotropic ground states and the resulting transients with configurations that relax to exhibit heterogeneous dipole moments, one would expect the broadband anisotropy isolated for each band to be independent of wavelength; modulations to the anisotropy, now simplified as $r(t)$, would only arise from the overlapping of disparate transient states and features as mentioned above and concerns surrounding white light continua as part of BPA measurements described in Section 1.2.3. Here, in light of discrepancies in adjacent probe wavelengths, the most plausible explanation is that BPA measurements have the capability to be even more descriptive of a transient state, but are complicated by the incorporation of higher lying transition dipoles into the net anisotropic result.

7.4.2 BPEA Nanoaggregates and Evidence of Intermolecular Energy Migration

Figure 7.6 shows the TA and BPA spectra collected for BPEA NCs excited at 400 and 500 nm. Figures 7.6a (400 nm) and 7.6b (500 nm) show very little difference in spectroscopic signatures or decay lifetimes as a function of pump wavelength, despite having been excited on either end of their highly structured steady-state absorbance band. The spectra contain two broad overlapping absorbances above 550 nm (centered at approximately 660 and 925 nm) as well as several sharp absorptive and negative peaks below 550 nm. Interestingly, the broad absorptive features decay on a 21 ps timescale, leaving a sharp progression of bands that correspond to residual bleach and transient absorption but only persisting in the high energy region of the spectrum which overlaps the region of the GSB.

The BPA spectra included as Figures 7.6c and 7.6d show more pronounced differences due to changing excitation energy than the TA spectra themselves. While the $r(t, \lambda)$ values show similar patterns between the two pump wavelengths, an interesting observation is that they are actually *lower* across the entire spectrum (especially the NIR) for 500 compared to 400 nm excitation. Both sets of $r(t, \lambda)$ values integrated over 650-750 nm decay toward zero as the signal intensity decays with bi-exponential decay lifetimes of approximately 1 and 26 ps to a constant anisotropy offset. Within the NIR region, the 400 nm spectra shows a larger proportion of rapid anisotropy decay than when using 500 nm excitation (which is far lower at early times). The sharp discontinuities of the anisotropy spectra below 525 nm are reflective of regions

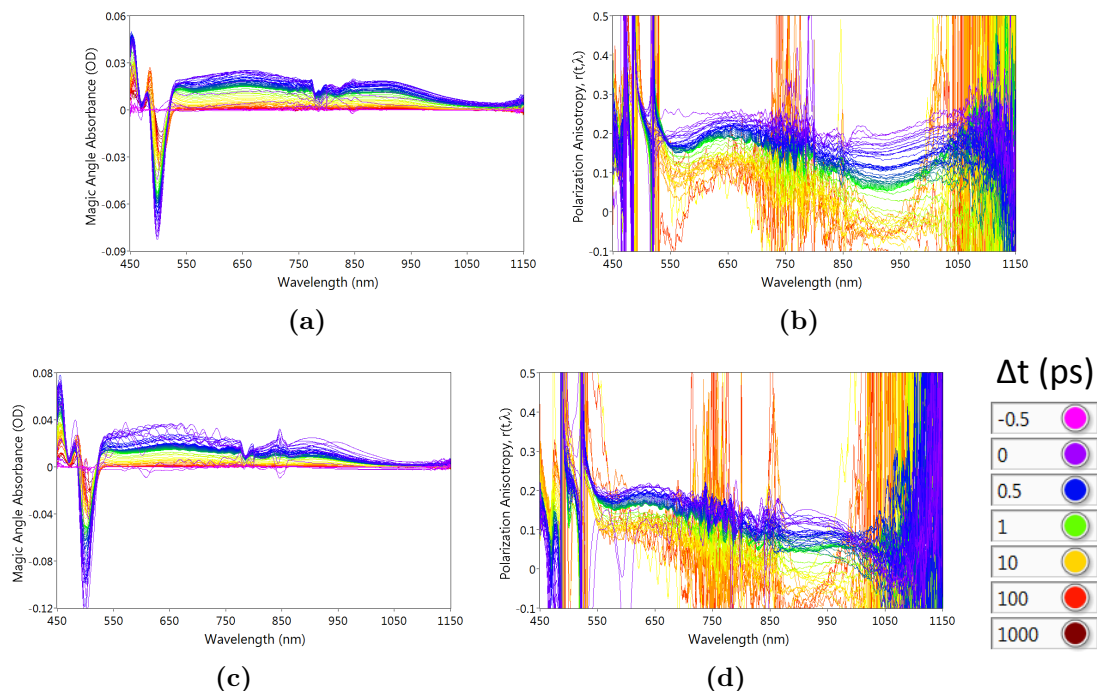


Figure 7.6: BPEA NC Transient Absorption and BPA Spectra: magic angle TA and BPA spectra corresponding to 400 nm (a and c) and 500 nm (b and d) excitation

where the TA spectra cross zero, and though that has little significance as is, it may be possible to model and decouple them in order to determine which sharp peaks correspond to each overlapping state, though this analysis is beyond the scope of this dissertation. Overall, the data from Figure 7.6 shows that similar measurements to those from Figure 7.4 can be conducted on aggregated materials, and that $r(t, \lambda)$ can reflect energy transfer timescales and the orientation of excited state localization, as well as serving as a probe of molecular rotation.

7.5 Conclusions

The experimental set-up detailed in Section 2.4 was employed to measure broadband electronic polarization anisotropies of various samples throughout this

dissertation and has been validated by the systematic interrogation of BPEA. Excitation wavelength dependent traces of anisotropies and their decays qualitatively agree upon the same rotational diffusion timescale and highlight the technique’s sensitivity to monitoring the relationship between dipole moments of various excited states, both through excited state relaxation and through comparisons of transient absorption signals within different regions. These results were found to be consistent to those previously shown for BPEA and shed new insight into interactions between different electronic excited states.

References

1. Cross, A. J. and Fleming, G. R. *Biophysical Journal* **46**(1), 45–56 (1984).
2. Horng, M.-L., Gardecki, J. A., and Maroncelli, M. *J. Phys. Chem. A* **101**(6), 1030–1047 (1997).
3. Takaya, T., Hamaguchi, H.-o., and Iwata, K. *The Journal of Chemical Physics* **130**(1), 014501 (2009).
4. Tice, D. B., Weinberg, D. J., Mathew, N., Chang, R. P. H., and Weiss, E. A. *J. Phys. Chem. C* **117**(25), 13289–13296 (2013).
5. Levitus, M. and Garcia-Garibay, M. A. *J. Phys. Chem. A* **104**(38), 8632–8637 (2000).
6. Yagita, Y. and Matsui, K. *Journal of Luminescence* **161**, 437–441 (2015).
7. Moore, A. M., Dameron, A. A., Mantooth, B. A., Smith, R. K., Fuchs, D. J., Ciszek, J. W., Maya, F., Yao, Y., Tour, J. M., and Weiss, P. S. *J. Am. Chem. Soc.* **128**(6), 1959–1967 (2006).
8. Yagita, Y., Hashimoto, A., Shimada, K., and Matsui, K. *J. Jpn. Soc. Colour Mater.* **85**(8), 321–326 (2012).
9. Shimizu, H., Yamada, M., Wada, R., and Okabe, M. *Polym. J* **40**(1), 33–36 (online November 13, 2007).
10. Tan, H.-S., Piletic, I. R., and Fayer, M. D. *J. Opt. Soc. Am. B* **22**(9), 2009 (2005).
11. Schott, S., Steinbacher, A., Buback, J., Nuernberger, P., and Brixner, T. *J. Phys. B: At. Mol. Opt. Phys.* **47**(12), 124014 (2014).

Chapter 8

Appendices

8.1 Appendix II: Experimental

8.1.1 Alternative Aggregate Preparation Techniques

Attempting the same reprecipitation procedure from Section 2.1 with triptycene in place of PCBM (a molecule added to fill space sterically without participating in P3HT electronic photophysics) revealed that not all materials will readily aggregate evenly as it tended to precipitate out more readily at higher concentrations.

Several sample preparation methods were used in preparing other aggregated samples for which no data is presented in the body of the thesis. Mixed solvent aggregates were used sparingly and involved the combination of two miscible solvents in which a solute was and was not soluble ('good' or 'favorable' and 'poor' solvents respectively). Poor solvent was slowly added to a dissolved solution of solute in good solvent to induce aggregation of a portion of the solute. Various solvent combinations were studied using RR-P3HT, and it is clear that the sample stability, lifetime, and degree of aggregation depend heavily on the choice and ratio of solvents. Chloroform (CHCl_3) was the only favorable solvent to produce the desired behav-

ior as chlorobenzene (ArCl) and THF would not sufficiently solvate the solute after introducing various poor solvents. Poor solvents including water, ethanol (EtOH), isopropyl alcohol (IPA), acetone, methanol (MeOH), and ethyl acetate (EtAc) were used with the last two producing usable samples and the last being the most successful overall. CHCl_3 :MeOH and CHCl_3 :EtAc mixtures yielded aggregates as reported previously with sample lifetimes of approximately two to three days and a few weeks, respectively, before precipitating. CHCl_3 :EtAc in a ratio of 25:75 %v/v was determined to be the optimal mixture in terms of level of aggregation and stability. While these samples remain in solution for approximately a month before irreversibly forming macroscopic material, a slow gradual change in their UV-Vis spectra becomes apparent over time as the aggregates are able to re-organize and self-assemble to form larger aggregates, or ones with different types of intermolecular ordering. These samples are slightly laser sensitive, and while it degraded much more quickly than those prepared by the reprecipitation method, it provided much more ordered aggregates and may be considered useful as an aspect of future studies. Attempts to prepare similar types of suspensions using regio-random (RRa)-P3HT, tri-phenyl benzene (TPB), and sexithiophene (6T) were unsuccessful. RRa-P3HT may be stable in other solvent mixtures not considered, but the poorer solubility of its reprecipitated NPs suggests that it is less amenable to aggregation overall. 6T and TPB seem incompatible with the technique, likely because of their smaller molecular size and the limited favorable and poor solvents that will work for them (e.g. H_2O is not a good solvent for this technique but is really the only candidate for a poor solvent for TPB).

6T aggregates were prepared by adding 1 mL of concentrated 6T in CHCl_3

solution into 10 mL of H₂O analogous with the procedure in the first technique. However, since the two solvents are not miscible, two distinct layers are formed with the oligomer preferring to remain in the organic phase of the mixture. Since CHCl₃ has a high vapor pressure and low boiling point, the sample is then shaken and sonicated extensively until all of the CHCl₃ has evaporated from the mixture. Much of the material precipitates out macroscopically (as the technique has not been optimized) but a small amount of analyte forms aggregates and remains suspended in the H₂O similar to the first technique. This method has been used in conjunction with a surfactant to generate NPs (Eref), but this has remained untested thus far in our lab. While this method provides the means to form aggregate suspensions for certain molecules which the previous methods are not applicable to, it is inferior to other methods as it is far less consistent, cannot be done if another organic solvent (e.g. acetonitrile) is present, and produces suspensions of much lower overall concentration.

Several methods have been attempted to form nanoparticles with “core-shell” morphologies, whereby an initially prepared RR-P3HT reprecipitated NPs are coated with PCBM during a second addition step to form layered NP’s. If successful, this method could be attempted with other molecules or to form 3-layered aggregates. Several methods involving benzene, dimethyl-sulfoxide (DMSO), and CHCl₃ have been attempted with varying results. Briefly, the DMSO method produces high quality core-shell particles but at low concentrations (Eref), and a method akin to that attempted for 6T with benzene or chloroform tends to produce macroscopic webbings of NPs interconnected by PCBM. All of these samples, however, exhibit fluorescence quenching relative to control RR-P3HT NPs, indicating some degree of energy/charge

transfer present via intermolecular interactions between P3HT and PCBM interfaces.

Finally, well ordered J-aggregate nanofibers of RR-P3HT were formed through temperature based aggregation and re-precipitation. A saturated solution of RR-P3HT in toluene with extra solute present was heated to 75°C and slowly cooled back to room temperature to induce aggregation from the now supersaturated solution. This technique produces dark, fibular crystals that exhibit self-organize into columns in solution and exhibit dramatically red-shifted steady state absorbance compared to other reprecipitated aggregates. These aggregates only remain stable for a couple days, and are plagued by a significant amount of As most of these supplementary last few methods inevitably contain significant amounts of macroscopic material, DLS is not recommended for characterizing their size distributions.

8.1.2 Pump Re-pump Probe Spectroscopy

Schematically, pump-re-pump-probe (PRP) measurements are very similar to FSRS measurements in that two pumps (in this case both femtosecond electronic excitations) and a minimum of four acquisition phases are necessary for calculating the appropriate ratios experimentally. These measurements are particularly useful in enabling a particular transient to be re-excited or depleted using a second femtosecond pump, thus providing very useful information towards decoupling spectroscopic features observed in TA and resolving differences amongst heterogeneous components of a signal transient signature. Manipulating these four phases, labeled PuRPr, PuPr, RPr, and Pr to reflect the pulses present (among the (pu)mp, (r)e-pump and (pr)obe),

allows one to extract a signal due only to the interaction of both pumps with the sample. To do so, one calculates the spectra listed below:

PRP/P = Synchronous signal PP/P = Pump probe (TA) RP/P = Re-pump probe (TA using re-pump pulse, sometimes negligible) PRPSig = PRP/P - PP/P - c*RP/P for $0 < c < 1$

To extract the pure three pulse signal, the signals due to both ordinary transient absorption of the sample and transient absorption imposed by interaction of the sample's ground state with the re-pump pulse must be accounted for and subtracted. Since the re-pump, by definition, arrives at the sample after initial interaction with the pump, the population of ground state seen by the re-pump is often modulated by the presence of the pump pulse (i.e. discrepancies arise between PRP and RP phases). In the case of the former, a portion of the ground state has been depopulated to generate the transient species of interest and others, leaving a smaller ground state population than seen ordinarily. Thus, the re-pump signal must be empirically scaled by a factor that is less than (but often close to) one to account for fewer ground state molecules being present to produce a re-pump only signal in the case of the PRP phase. The same concern is irrelevant for the pump's transient absorption as it is formally always the first pulse to arrive, thus the presence/absence of the re-pump has no bearing on its signal. Removing both of these contributions yields a net signal due only to excited state interaction of the re-pump pulse with an excited state population produced by excitation with the pump pulse. PRP/P, PP/P, and RP/P are PRP equivalents of FSRS phases re-cast to simultaneous TA of both pumps, then the actinic and re-pump's individually relative to a probe pulse.

8.2 Appendix IV: PTMT

400nm Excitation: λ Shift (nm) Relative to NT-PTMT				
	GSB	SE	S_1	I_1
Ti-PTMT	-0.15	-11.86	-54.78	32.00
TO-PTMT	-11.94	3.81	-183.02	-100.60
TTMTT	-4.25	-5.51	-43.89	-43.46
PTMTT	15.85	13.55	18.35	-20.66

400nm Excitation: ν Shift (cm^{-1}) Relative to NT-PTMT				
	GSB	SE	S_1	I_1
Ti-PTMT	8	363	532	-699
TO-PTMT	611	-113	2041	2716
TTMTT	214	167	421	1065
PTMTT	-762	-397	-166	488

480nm Excitation: λ Shift (nm) Relative to NT-PTMT				
	GSB	SE	S_1	I_1
Ti-PTMT	-3.38	-20.33	-44.64	8.83
TO-PTMT	-16.00	-6.32	-136.85	-85.95
TTMTT	-21.00	-14.39	-73.49	-69.96
PTMTT	20.89	2.96	-0.83	18.05

480nm Excitation: ν Shift (cm^{-1}) Relative to NT-PTMT				
	GSB	SE	S_1	I_1
Ti-PTMT	155	602	405	-180
TO-PTMT	753	183	1363	2025
TTMTT	999	422	685	1606
PTMTT	-909	-84	7	-363

400nm Excitation: NP λ Shift (nm) Relative to Solution				
	GSB	SE	S_1	I_1
Ti-PTMT	3.14	1.27	-5.87	5.05
TO-PTMT	-12.21	-16.59	60.25	26.69
TTMTT	-20.07	16.73	25.06	43.47

400nm Excitation: NP ν Shift (cm^{-1}) Relative to Solution				
	GSB	SE	S_1	I_1
Ti-PTMT	-155.16	-39.60	60.45	-104.35
TO-PTMT	660.17	504.72	-761.60	-811.20
TTMTT	1066.49	-496.43	-244.97	-1064.83

480nm Excitation: NP λ Shift (nm) Relative to Solution				
	GSB	SE	S_1	I_1
Ti-PTMT	-4.69	6.35	-35.13	-11.77
TO-PTMT	N/A	-14.00	0.45	75.00*
TTMTT	18.00	23.07	15.06	26.16

480nm Excitation: NP ν Shift (cm^{-1}) Relative to Solution				
	GSB	SE	S_1	I_1
Ti-PTMT	218.38	-192.74	344.08	241.05
TO-PTMT		419.12	-5.15	-1794.90
TTMTT	-862.20	-666.55	-148.56	-640.90

(a)

λ Shift (nm) 400 Relative to 480nm Excitation				
	GSB	SE	S_1	I_1
NT-PTMT	-20.85	-13.55	-30.02	-34.95
Ti-PTMT	-17.63	-5.09	-40.16	-11.77
TO-PTMT	-16.79	-3.41	-76.19	-49.60
TTMTT	-4.10	-4.66	-0.42	-8.45
PTMTT	-25.89	-2.96	-10.83	-73.66

ν Shift (cm^{-1}) 400 Relative to 480nm Excitation				
	GSB	SE	S_1	I_1
NT-PTMT	991.95	396.52	268.31	759.66
Ti-PTMT	844.92	157.37	395.29	241.05
TO-PTMT	849.68	100.37	946.76	1450.95
TTMTT	206.17	141.15	4.19	218.56
PTMTT	1139.15	84.32	95.24	1611.03

NP λ Shift (nm) 400 Relative to 480nm Excitation				
	GSB	SE	S_1	I_1
Ti-PTMT	-9.80	-10.17	-10.89	5.05
TO-PTMT		-6.00	-16.40	-97.91*
TTMTT	-42.17	-11.00	9.58	8.85

NP ν Shift (cm^{-1}) 400 Relative to 480nm Excitation				
	GSB	SE	S_1	I_1
Ti-PTMT	471.37	310.51	111.66	-104.35
TO-PTMT		185.98	190.30	2434.65*
TTMTT	2134.86	311.26	-92.22	-205.37

(b)

Figure 8.1: Wavelength/Frequency Shifts of PTMT Absorbances: (a) shifts of each PTMT feature relative to NT (left column) and each aggregate relative to its solution phase for 400 and 480 nm excitation and (b) shifts of each PTMT feature for 400 nm relative to 480 nm excitation

400 GSB	IRF	A_1	τ_1	A_2	τ_2	A_3	τ_3
NT-PTMT	0.033	4.94	0.053	0.603	60.7	0.288	753
TO-PTMT	0.055	1.64	0.154	0.712	140	0.147	
TI-PTMT	0.046	0.144	8.19	0.467	253	0.337	
PTMTT	0.146			0.788	128	0.210	2880
TTMTT	0.031			0.374	124	0.575	1710
TO-PTMT NP	0.059			0.492	11.2	0.375	1010
TI-PTMT NP	0.043	13.0	0.059	0.505	5.78	0.189	513
TTMTT NP	0.074	0.516	1.52	0.134	62.5	0.441	1680

480 GSB	IRF	A_1	τ_1	A_2	τ_2	A_3	τ_3
NT-PTMT	0.075			0.772	52.3	0.164	902
TO-PTMT	0.031	0.524	0.316	0.340	61.9	0.256	732
TI-PTMT	0.070	4.016	0.085	0.236	11.0	0.531	862
PTMTT	0.030			0.217	11.5	0.481	153
TTMTT	0.092	0.354	0.565	0.339	23.9	0.485	
TI-PTMT NP	0.030	0.744	0.161	0.434	9.15	0.141	499
TTMTT NP	0.030	1.043	0.419	0.178	11.1	0.145	

(a)

400 S_1	IRF	A_1	τ_1	A_2	τ_2	A_3	τ_3	A_{Rise}	τ_{Rise}
NT-PTMT	0.141			0.543	34.5	0.459	284		
TO-PTMT	0.150			0.448	18.0	0.552	292	79.3	0.560
TI-PTMT	0.150			0.291	20.7	0.709	348	312	0.649
PTMTT	0.150			0.582	71.6	0.418	493	122	0.489
TTMTT	0.150			0.204	98.7	0.709	631	115	0.518
TO-PTMT NP	0.088	0.202	3.26	0.758	79.7				
TI-PTMT NP	0.077	0.477	1.50	0.467	14.1	0.174	184		
TTMTT NP	0.085	0.684	1.60	0.394	16.1	0.074	750		

480 S_1	IRF	A_1	τ_1	A_2	τ_2	A_3	τ_3
NT-PTMT	0.069	0.262	0.713	0.568	29.8	0.289	230
TO-PTMT	0.117	2.824	0.163	0.579	118	0.276	382
TI-PTMT	0.147			0.200	24.3	0.782	407
PTMTT	0.128			0.262	16.5	0.707	168
TTMTT	0.132			0.207	7.57	0.785	763
TO-PTMT NP	0.030	>100	0.022	0.387	4.03	0.132	181
TI-PTMT NP	0.030			0.560	2.98	0.361	84.8
TTMTT NP	0.033	0.768	0.369	0.401	3.83	0.078	122

(b)

Figure 8.2: Regression Model Parameters for PTMT GSB and S_1 Decays: exponential decay fitting parameters for each PTMT material (a) GSB and (b) S_1 NIR absorbance

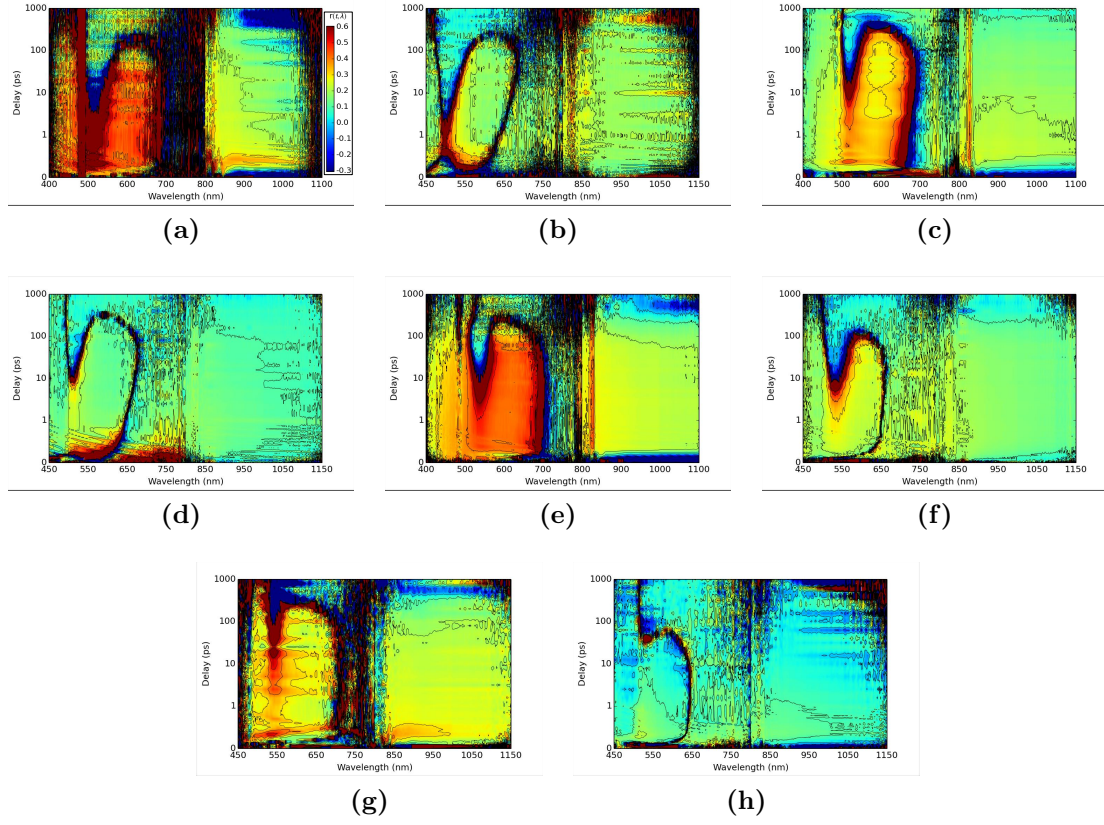


Figure 8.3: BPA Contour Plots for PTMT Samples: (a, b) TO, (c, d) TI, (e, f) NT, (g, -) PTMTT, and (h, -) TI NP excited at 480 and 400, respectively

8.3 Appendix V: Dyad

Figures 8.4, 8.5, and 8.6 show the excitation wavelength and sample composition data collected from the dyad chapter, comparable transient absorption spectra of DA-6 and DA-3, and kinetic traces fit to different absorptive features of DA-2, 3, and 6 highlighting their kinetic similarities, respectively.?

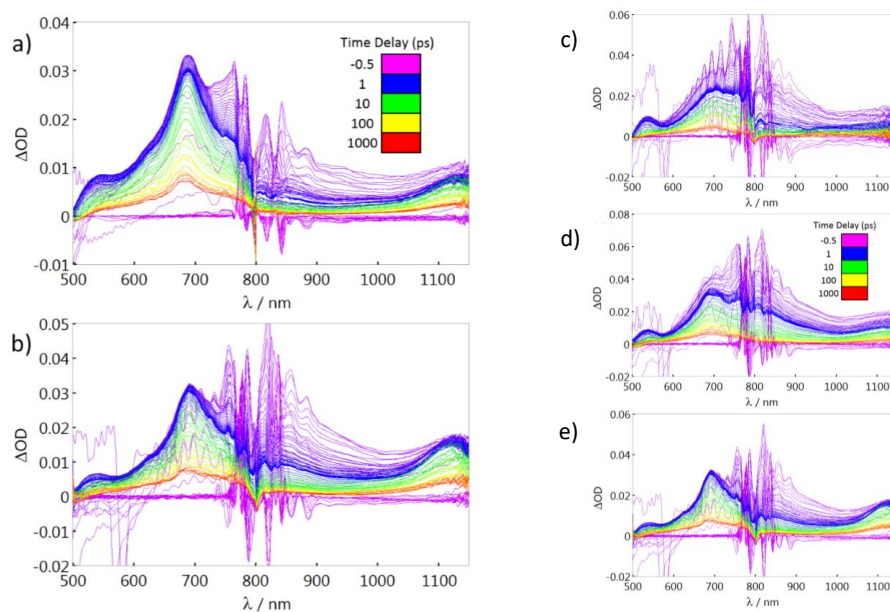


Figure 8.4: 480 nm Excitation and Control, Mixture, and Dyad TA Spectra: comparison of 400 nm (a) and 480 nm (b) excitation spectra in DA-2 and pure control (c), mixture (d), and dyad (e) spectra used for the analysis covered by Figure 5.6

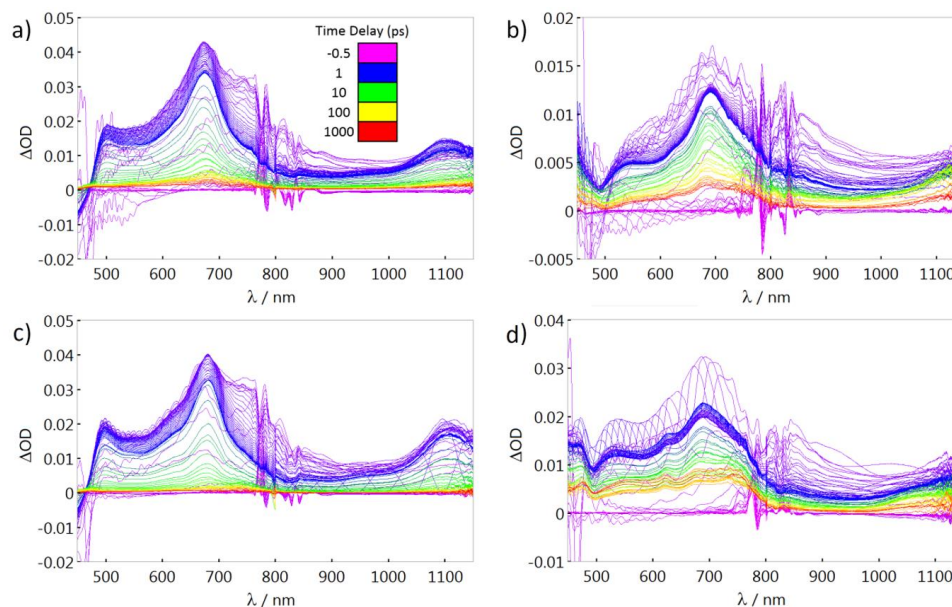


Figure 8.5: DA-6 and DA-3 TA Spectra: comparison of unassembled and assembled traces of DA-6 (a and b) and DA-3 (c and d) which show very similar spectral patterns and decay timescales as DA-2 in Figure 5.3

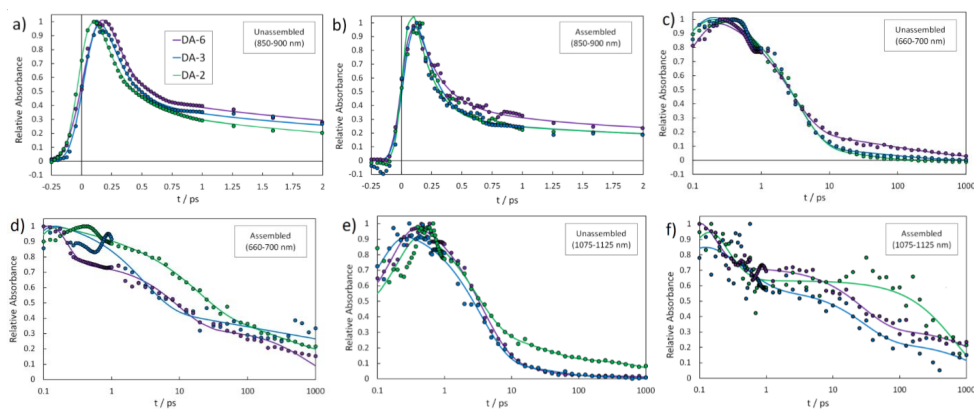


Figure 8.6: DA-2, 3, and 6 Integrated Decay Traces: kinetic decay traces corresponding to integrated features of the unassembled and assembled data shown in Figures 5.3 and 8.5

8.4 Appendix VI: CPEC

Figure 8.7 shows the fluence dependence associated with 600 nm excitation of PTAK. Higher excitation fluences lead to a more rapid decay progression, indicating a larger relative occurrence of multi-excitonic or exciton-exciton annihilation events that serve as relaxation pathways.

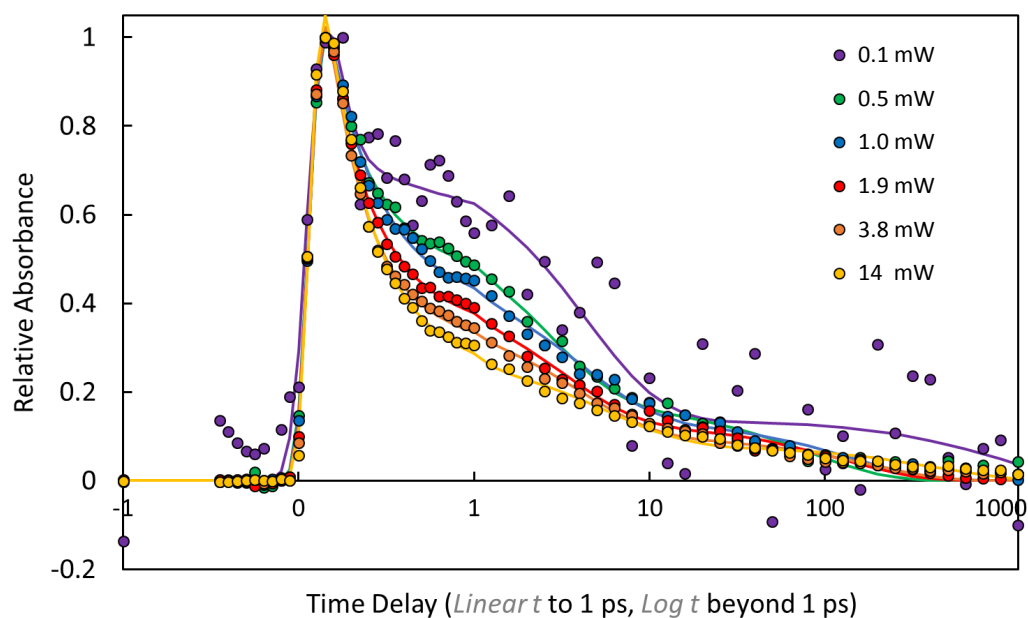


Figure 8.7: PTAK Fluence Dependence NIR Decay Traces: kinetic decay traces corresponding to the fluences marked in the legend of pure PTAK excited at 600 nm with comparative pump powers ranging from 0.1 to 14 mW

8.5 Curriculum Vitae

TIMOTHY J. MAGNANELLI

Department of Chemistry
Johns Hopkins University
Baltimore, MD 21218-2680

Home Address
432 Windy Knoll Dr.
Mount Airy, MD 21771

Office #: (410)-516-4851
E-mail: tmagnan2@jhu.edu

Cell #: (301)-514-3332

Current Position

Johns Hopkins University (JHU, Baltimore, MD)

Physical Chemistry Research Assistant (Ph.D. expected 10/2017)

Research Advisor: Dr. Arthur E. Bragg

Research Topic: Spectroscopic probes of charge separation, energy transfer, and their dependence on local structure in assembled organic materials.

Education

Johns Hopkins University (JHU), Baltimore, MD (09/11-Present) **M.A.** Physical Chemistry, May 2013, GPA 3.77

University of Maryland Baltimore County (UMBC), Baltimore, MD (01/07-12/09) **B.S.**

Chemistry, **B.S.** Mathematics, December 2009, Cum Laude, GPA: 3.64 GRE: 1310, Chemistry Subject GRE: 770

Research Experience

Johns Hopkins University

Bragg Lab – Chemistry Department

(01/12 – Present)

- Apply and develop ultrafast transient spectroscopies, e.g. femtosecond stimulated Raman, transient absorption, and electronic polarization anisotropy to explore research topics highlighted below
- Interrogate aggregates of conjugated polymers and oligomers relevant to organic photovoltaic (OPV) devices to understand the effects of material morphology on the properties of charge-separated states
- Investigate charge and energy transfer/migration within biologically compatible oligomer and polyelectrolyte supramolecular assemblies, respectively
- Examine prototypical OFET device materials for spectroscopic signatures of bias stress and dielectric polarization upon corona charging with steady state spectroscopic methodology
- Complement spectroscopic measurements with *ab initio* computations and spectral decomposition techniques such as SVD and PCA

University of Maryland Baltimore County

Arnold Lab – Chemistry Department

(08/09 – 09/10)

- Conducted extensive research using laser induced fluorescence and emission spectroscopies
- Operated Nd-YAG lasers, manipulated optical set-ups, and prepared/synthesized test samples
- Investigated fluorescence signatures of nitrotoluenes to test the long range detection of explosive materials and of naphthalene derivatives to ascertain their transient state lifetimes

Publications

Magnanelli, T. J.; Bragg, A. E. Time-Resolved Raman Spectroscopy of Polaron Pair Formation in Poly(3Hexylthiophene) Aggregates. *J. Phys. Chem. Lett.* **2015**, 6 (3), 438–445.

- Extracted pure Raman spectra corresponding to charge transfer states in conjugated polymer aggregates and used time-dependent measurements to reinforce/clarify the dynamics and mechanism by which coupled polaron pair states are formed

Sanders, A. M.; Magnanelli, T. J.; Bragg, A. E.; Tovar, J. D. Photoinduced Electron Transfer within Supramolecular Donor–Acceptor Peptide Nanostructures under Aqueous Conditions. *J. Am. Chem. Soc.* **2016**, 138 (10), 3362–3370.

- Conducted, analyzed, and wrote-up ultrafast photophysical characterization of charge separation dynamics critical for proving increased charge separation in dyad assemblies and clarifying charge migration patterns amongst stacked chromophores

Bragg, A. E.; Yu, W.; Zhou, J.; Magnanelli, T. Ultrafast Raman Spectroscopy as a Probe of Local Structure and Dynamics in Photoexcited Conjugated Materials. *J. Phys. Chem. Lett.* **2016**, 7 (19), 3990–4000.

- Contributed research information and discussion to topics concerning aggregated materials and extensions of FSRS and related spectroscopic techniques

Yu, W.; Magnanelli, T. J.; Zhou, J.; Bragg, A.E. Structural Heterogeneity in the Localized Excited States of Poly(3-hexylthiophene). *J. Phys. Chem. B*, **2016** 120(22), 5093-5102.

- Developed 3-pulse, 8-phase acquisition methodologies to improve upon data quality and correct for scatter in the measurements described in this work; utilized these methodologies to collect complementary information on regio-regular (RR-)P3HT to support conclusions made regarding the heterogeneity of transients along polymer strands

Teaching Experience

Johns Hopkins University

Physical Chemistry Lab Teaching Assistant:

(09/11-05/15)

- Instructed students in the operation of the NO Oxidation Kinetics, Lattice Energy of Argon, I₂ Absorption, Na Absorption/Emission, and NMR-related experiments; assessed student performance on formal lab report submissions
- Improved manifold and trap handling protocols for safe execution of the NO Oxidation Kinetics experiment; designed LabVIEW-based automated data acquisition software to modernize Lattice Energy of Argon, BET Isotherm, and Effusion of Gases experiments; implemented modifications to existing procedures to improve the data quality and accuracy of the Na and I₂ spectroscopic experiments

University of Maryland Baltimore County

Introductory Lab and Physical Chemistry Teaching Assistant (01/10-12/10)

- Taught the principles and procedures behind introductory experiments; graded lab reports and problem sets; organized and managed physical chemistry help sessions

Part Time Instructor (01/11-05/11)

- Instructed in 4 sections of introductory lab; taught and oversaw experiments for 96 students; graded and evaluated the majority of their assignments

Private Tutoring in Chemistry, Mathematics, and Statistics (01/07-Present)

Middle School Catholic Religious Education Instructor (09/08-06/09)

Awards and Fellowships

Langmuir-Cresap Fellowship in recognition of an outstanding physical chemistry graduate student (2016)

Ernest E. Marks Award in recognition of teaching excellence (2011)

Conference Participation

Gordon Research Seminars/Conferences (GRS/GRC), Stonehill College (Easton, MA), Poster Presenter

Photochemistry (GRS and GRC) (07/18/15 – 07/24/15)

“Ultrafast Characterization of Charge Transfer Processes within Nanoparticles and Peptide-based Aggregates of Conjugated Polymers and Oligomers”

Atomic and Molecular Interactions (GRC) (07/13/14 – 07/18/14)

“Ultrafast Characterization of Excited State Structure and Dynamics within Nanoparticulate Aggregates of Conjugated Polymers”

NIDays DC, Washington D.C., Attendee (11/18/14)

NIH Career Symposium, Washington D.C., Attendee (05/16/14)

Skills and Proficiencies

- Extensive LabVIEW program design and implementation experience
- Proficiencies with Mathematica, Matlab, Gaussian, HTML/CSS, and Microsoft Office
- Knowledge of various technical lab instruments – Ti:Sapphire and Nd-YAG laser systems, OPA's, TEM Microscopes, NMR, FTIR, UV-Vis-NIR spectrometers, and various CCD, array, and fiber coupled detectors.
- Experience fabricating custom metal/optical components within the department machine shop
- Spanish and Latin (beginner level)